Characterization of molecule clustering and liquid transport at nearly ideal solid surfaces

Rosenholm, Jarl B.

Published in:
Advances in Colloid and Interface Science

DOI:
10.1016/j.cis.2022.102733

Published: 01/09/2022

Document Version
Final published version

Document License
CC BY

Advances in Colloid and Interface Science 307 (2022) 102733

Contents lists available at ScienceDirect

Advances in Colloid and Interface Science

journal homepage: www.elsevier.com/locate/cis

Historical Perspective

Characterization of molecule clustering and liquid transport at nearly ideal solid surfaces

Jarl B. Rosenholm

Physical Chemistry, Laboratory of Molecular Science and Engineering, Aurum, Henriksgatan 2, 20500 Åbo (Turku), Finland

ARTICLE INFO

Keywords:
Vapor adsorption and clustering
Molecular kinetic (MK) models
Thin film metastability and transport
Hydrodynamc (HD) models
Molecular hydrodynamic (MH) models
Forced fluxes (wetting)

ABSTRACT

Vapor adsorption, mobility, two-dimensional (monolayer formation) and three-dimensional (multilayer formation) clustering is evaluated. Two-dimensional vapor diffusion is compared to results obtained from molecular kinetic (*MK*) model fits. Three-dimensional clustering results in condensation of multimolecular vapor layers to thin films. Thin films are characte-rized by line tension and liquid spreading by hydrodynamic (*HD*) models. Although it is experimentally shown that steady-state wetting ranges are intersected by a chaotic slip-stick range, *MK* and *HD* models are combined to molecular hydrodynamic (*MH*) models with the aim to cover this slip-stick range. The results of *MK*, *HD* and *MH* model fits are, however rather poor (unphysical results). Thin film (α-phase) models are compared to thick film (β-phase) models. In order to improve model designs, established phenomenological relation-ships known from irreversible thermodynamics are presented. Forced wetting, expressed as generalized fluxes can be made dependent on multiple generalized conjugate forces which enables identification of dominant interactions to be introduced in future improved transport models.

1. Introduction

When vapor molecules collide with solid surfaces, they lose one degree of freedom, which results in reduced two-dimensional mobility. This is experimentally observed as reduced surface diffusivity. At surface sites physicochemical interaction immobilizes molecules. Such interactions are dispersive (*D*) and Lifshitz-van der Waals (*LW*), Lewis's type acid (*A*)–base (*B*) and Brϕnsted type hydrogen bond/release interactions [1]. Alternative interaction scales are provided by Gutmann AN-DN, Drago *E*-C and Parson-Parr HSAB parameters, Pauling-Mulliken-Allred-Roschow electronegativity and by Brϕnsted A-B and Hildebrand-Hansen-Barton solubility parameters [2,3]. The overall surface pressure created by two-dimensionally distributed vapor molecules can conveniently be determined by adsorption isotherms. The two-dimensional mobility is restricted further when they meet obstacles, such as sessile drops or liquid films. The additional loss of freedom results in molecular clustering (wedge formation) at three-phase contact-line (*tpcl*). Molecular clustering as multimolecular layers occur when partial vapor pressure exceeds saturation (monolayer capacity). The three-dimensional molecular clustering is characterized by disjoining pressure. At supersaturation multimolecular vapor layers condense to liquid films which may decompose to thin films (α-phase) and thick films (β-phase) or sessile drops.

Molecular clustering at *tpcl* is characterized by molecular kinetic (*MK*) models which relate wetting rate to the change of (cos) contact angle from its equilibrium (Young) value (time-dependent surface pressure). Fits of *MK* model to experimental data provides kinetic quasi-equilibrium constants (frequencies) and distances between surface sites. Forced wetting has been employed to extend advancing (wetting) and receding (dewetting) ranges. Advancing and receding liquids are characterized by hydrodynamic (*HD*) models. The difference between cube of time-dependent contact angle from cube of equilibrium (Young) contact angle is related to wetting rate expressed as capillary number (*Ca*) multiplied by natural logarithm of ratio between characteristic macroscopic and nanoscopic (molecular) lengths. This approach resembles characterization of buildup of fractal objects. In order to cover a wide wetting range, the *HD* model is modified by characteristic length ratios. Straight-forward log(radius)–log(time) and log(contact angle)–log(time) plots reveal, however that the steady-state wetting rate ranges are intersected by chaotic slip-stick ranges. Contrary to this reality, *MK* and *MD* models were combined to molecular hydrodynamic (*MH*) models to enforce this chaotic slip-stick behavior to comply with steady-state *MH* models. As results model fits produced poor (unphysical) data.

The observed drawbacks seem to depend on: 1) Although nanometric surface structure heterogeneities may influence wetting, no corrections for surface roughness were made before model fits. 2) The well-known contact angle–surface structure relationships identifying different; full

E-mail address: jarl.rosenholm@abo.fi.

https://doi.org/10.1016/j.cis.2022.102733
Received in revised form 6 July 2022;
Available online 14 July 2022

Nomenclature

Symbol

A	Surface area
C	Cohesion, adsorption constant
D	Diffusion, permeability
E	Energy
F	Helmholtz energy, Faraday const., Force
G	Gibbs energy
H	Enthalpy, Hamaker constant
I	Electric charge flow, current
J	Flux
K	Rigidity constant
L	Macroscopic length
N	Number
P	Pressure
R	Radius, ratio, gas constant
S	Entropy, work of spreading
T	Temperature
U	Internal energy
V	Volume
W	Work, adhesion
X, Y	State functions
Γ	Surface excess
Δ	Process, difference
Θ	Contact angle
Π	Disjoining pressure
Σ	Sum of
BET	Adsorption isotherm
Bo	Bond number
Ca	Capillary number
FFG	Adsorption isotherm
HdB	Adsorption isotherm
IR	Infrared
L_{cap}	Capillary length
MW	Microwave
S_{dr}	Per cent projected area increase
UV	Ultraviolet
We	Weber number
a	molecular area
d	diameter
f	function, slope
h	height, Planck const.
k	Boltzmann const.
l	Nanoscopic length
n	amount (nr. moles)
p	partial pressure
q	heat, charge
r	radius
s	slope
t	time
v	molecular volume
x	partial pressure ratio
z	valence (charge nr.)
γ	liquid surface tension
ε	permittivity (diel.const.)
ζ	effective surface pot.
η	dynamic viscosity
θ	surface coverage
κ	rate const., frequency
λ	site distance
μ	chemical pot., kinematic visc.
ν	frequency
π	Surface pressure
ρ	density
σ	solid surface energy
τ	relax.time, line tens., stress tensor
υ	wetting rate
ϕ	relaxation potential
ψ	electric potential
ω	Angular frequency
Re	Reynolds number
S_q	Root mean square roughness
vOCG	Lewis acid-base model

Upper indices

A	Acid, arithmetic, advancing
AB	Acid-Base, hydrogen bond
B	Base
D	London dispersive
G	Geometric
HD	Hydrodynamic
LW	Lifshitz-van der Waals
MK	Molecular kinetic
MH	Molecular hydrodynamic
P	Polar
R	Receding
Y	Young (equilibrium)
0	Limiting, quasi-equilibrium
cap	capillary
$grav$	gravitation
el	electrical
n	adjustable exponent
s	surface
str	structural
t	time dependent
τ	at tension
vdW	van der Waals
#	activation
~	electrochemical

Lower indices

$e(xt)$	external
hd	hydrodynamic
int	internal, component
j	molecular jump, component
$local$	local
k	component
m	molar, molecular, microscopic
mon	monolayer
r	radius
sat	saturated
$tpcl$	three-phase contact-line
vis	viscous
γ	friction
λ	adsorption site (distance)
B	Blake
C	cutoff
E	electrostatic, charges
F	Film
HVT	Hoffman-Voinov-Tanner
L	Liquid, Langmuir
M	Macroscopic
O	Oil, hydrocarbon
S	Solid, spreading, slip
T	temperature
V	Vapor, Volmer, Voinov
W	Work, wedge, Wenzel
X	$V, L, F,$ state variable
Y	State function

Z	Zhou (Sheng)	*i*	component
0	Vapor free (vacuum)	*infl*	inflection
Θ	Contact angle	*k*	component
ads	adsorption	*j*	molecular jump, component
ave	average	*local*	Local
base	base	*men*	meniscus
bu	buoyancy	*p*	Pore
c	coordination, cylinder, conc.	*s*	sphere
cap	capillary	*ss*	slip-stick
cond	condensation	*vdW*	van der Waals
d	drop (profile)	*ϕ*	cross-section
diff	diffusion	*φ*	interfacial base
f	fractal, friction	*υ*	wetting rate

(imbition), partial (Wenzel), partial rejection and full rejection (Lotus) wetting mechanisms were ignored. 3) No detailed physicochemical properties (van der Waals, Lewis, Brϕnsted) of probe liquids and model solids were recognized when probe liquids and model solids were selected and when fits were evaluated. 4) The aim to enforce experimentally observed unstable (chaotic) slip-stick wetting to obey steady-state *MK*, *HD* and molecular hydrodynamic (*MH*) models seems unjustified. The poor success is evident from obtained results. 5) The *MK*, *HD* and *MH* models have been developed in isolation, without correlation to corresponding key properties of (diffusion, line tension, thin film spreading) processes. As a result, some modifications have no physicochemical foundation.

Forced wetting is a transport process relating to irreversible thermodynamics. Due to poor results, the presented transport models are suggested to be expanded by established pheno-menological relations from irreversible thermodynamics. It is shown that forced liquid flow at solid surfaces can be expanded as generalized fluxes, which can be made dependent on several conjugate generalized forces. This approach provides an opportunity to design experiments to support future improved transport models.

2. Two-dimensional macroscopic equilibrium wetting

Traditionally partial wetting has been described by work of adhesion between sessile drops and solid substrate. The interaction between sessile drop and solid surface (adhesion) may be characterized in terms of dispersive, polar, and Lewis-type acid-base contributions. The potential spreading of sessile drop on the surface is described by work of spreading which equals work of adhesion reduced by work of cohesion of spreading liquid. At experimental conditions, the surrounding is more or less saturated by liquid vapor. The focus of this section is on the relationships between these properties.

2.1. Thermodynamic considerations

The most typical set of parameters for a system containing two homogeneous phases separated by one flat interface is based on changes of internal energy (*U*):

$$dU = TdS + SdT - PdV - VdP + \gamma dA + Ad\gamma + \Sigma_i \mu_i dn_i + \Sigma_i n_i d\mu_i \quad (1)$$

where γ = surface tension, μ = chemical potential and n = amount of substance. In classical thermodynamics changes are allowed only for extensive properties, while the intensive variable are kept constant. The differentials of intensive state variables are omitted as stated specifically by Gibbs-Duhem relationship [1,4]:

$$SdT - VdP + Ad\gamma + \Sigma_i n_i d\mu_i \equiv 0 \quad (2)$$

Reduced from total differential, we find the corrected differential of internal energy [1,4] as:

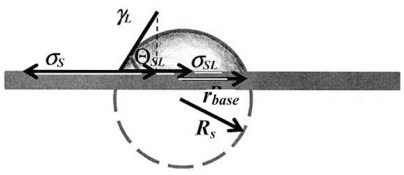

Fig. 1. Contact angle of a hemispherical sessile drop on an ideally smooth and homogeneous surface is characterized by the horizontal vectorial stress laid upon the three-phase (Solid-Liquid-Vapor) contact-line (*tpcl*). Radius of curvature (symmetry) of the sphere (R_s) and of drop base radius (r_{base}) are usually not equal.

$$dU = TdS - PdV + \gamma dA + \Sigma_i \mu_i dn_i \quad (3)$$

Helmholtz energy (*F*), enthalpy (*H*) and Gibbs free energy (*G*) are all related to the internal energy [1,4] as:

$$dF = d(U - TS) = -SdT - PdV + \gamma dA + \Sigma_i \mu_i dn_i \quad (4)$$

$$dH = d(U + PV) = TdS + VdP + \gamma dA + \Sigma_i \mu_i dn_i \quad (5)$$

$$dG = d(U - TS + PV) = -SdT + VdP + \gamma dA + \Sigma_i \mu_i dn_i \quad (6)$$

Each of them considers different dependencies on the working state variables, *T, P, V* and *S*. An extended evaluation of these relationships is presented elsewhere [5]. Gibbs-Duhem relationship (2) provides the important Gibbs adsorption equation at constant temperature and pressure as:

$$Ad\gamma + \Sigma_i n_i d\mu_i \equiv 0 \quad \Leftrightarrow \quad d\gamma = \Sigma_i \Gamma_i d\mu_i \quad (7)$$

where Γ represents surface excess.

2.2. Equilibrium wetting of ideal solid surfaces

The equilibrium properties of sessile drops on structurally and chemically ideal solid surfaces is evaluated in terms of classical (mechanic) thermodynamic parameters (entropy changes disregarded). The dynamic *macroscopic wetting* relates to a macroscopic (μm-mm) length scale. The surface energy of strained solids is denoted σ_S to distinguish it from equilibrium surface tensions of relaxed liquids denoted γ_L. In both cases tension is expressed as mN/m and surface energy as mJ/m^2. If a pure liquid (*L*) is placed in contact with a smooth and homogeneous solid surface (*S*) maintaining temperature and pressure and composition constant we may, in the absence of other work functions, derive the Young equation in the following way (Fig. 1) [1]:

$$dG_{SL} = \sigma_{SV} dA - \gamma_{LV}(dA cos\Theta_{SL}) - \sigma_{SL} dA \quad (8a)$$

Note that polar solids are at normal experimental conditions covered by vapor (*V*). At equilibrium there is no change of Gibbs surface energy:

Table 1
Dispersive surface energy (Eq.(13a)) of four model solids determined geometrically (Eq.(13a)) with octane (*O*), hexadecane (*H*), α-bromonaphtalene (*B*) and diiodomethane (*D*) indicated by upper indices. Model solids were hydrophobized by dichlorodimethylsilane in xylene [1]. Typical differences from arithmetically determined (Eq. (13b)) dispersive component is 0.0 (hydrocarbons), 0.2 (*B*) and 0.6 (*D*).

	γ_{LV}	γ_{LV}^{D}	σ_{SV}^{O}	σ_{SV}^{H}	σ_{SV}^{B}	σ_{SV}^{D}
	mN/m	mN/m	mJ/m^2	mJ/m^2	mJ/m^2	mJ/m^2
Octane	22.2	22.2				
Hexadecane	28.4	28.4				
α-BrNaphtalene	44.4	44.4				
Diiodomethane	50.8	50.8				
SiO_2-hydrophobic			22.2	23.3	24.6	21.7
SiO_2-hydrophilic			22.2	28.1	39.6	40.7
TiO_2-hydrophobic			22.2	28.4	38.0	40.2
TiO_2-hydrophilic			22.2	28.4	44.3	45.3

$$dG_{SL}^{s} = \frac{dG_{SL}}{dA} = 0 \quad \Leftrightarrow \quad \sigma_{SV} = \gamma_{LV} cos\Theta_{SL} + \sigma_{SL} \tag{8b}$$

The influence of surface energies and surface tension are expressed as a balance of horizontal vectors along the solid surface/interface. This balance is illustrated for a hemispherical sessile drop in Fig. 1.

The change in free surface energy may also be expressed by the Dupré equation for work of adhesion [1] as:

$$\Delta_W G_{SL}^{s} = -W_{SL} = \sigma_{SL} - \gamma_{LV} - \sigma_{SV} \tag{9}$$

As shown, work functions are defined for separation of the interconnected phases (work done by the system), while Gibbs´surface energy for adhesion is defined as uniting the surfaces. Thus, for a spontaneous process they have opposite signs. Adhesion characterizes the interaction between two (condensed) phases. The contact angle can be determined graphically or geometrically. Assuming that the drop is represented by a hemisphere it is characterized by Laplace pressure. The key work functions in surface chemistry are [1]:

$$\text{Cohesion}: C_{SS} = 2\sigma_{SV} \quad \Leftrightarrow \quad C_{LL} = 2\gamma_{LV} \tag{10a}$$

$$\text{Adhesion}: -\Delta_W G_{SL}^{s} = W_{SL} = \sigma_{SV} + \gamma_{LV} - \sigma_{SL} = \gamma_{LV}(cos\Theta_{SL} + 1) \tag{10b}$$

$$\text{Spreading}: -\Delta_S G_{SL}^{s} = S_{SL} = \sigma_{SV} - \gamma_{LV} - \sigma_{SL} = W_{SL} - C_{LL} = \gamma_{LV}(cos\Theta_{SL} - 1) \tag{10c}$$

As shown, the potential energy for spreading liquids on solids equals the difference between work of solid-liquid adhesion and liquid-liquid cohesion.

2.3. Non-specific solid-liquid interactions

Traditionally medium to long chain-length hydrocarbons have been used as standard for hydrophobic (London, dispersive, *D*) solid-liquid interactions. Fowkes and Zettlemoyer subtracted the surface tension of hydrocarbon oils ($\gamma_{LV}^{D} \approx \gamma_{OV}$) from the surface tension of polar liquids (γ_{LV}) to obtain the residual polar (*P*) surface tension [1]:

$$\gamma_{LV} = \gamma_{LV}^{D} + \gamma_{LV}^{P} \quad \Leftrightarrow \quad \gamma_{LV}^{P} = \gamma_{LV} - \gamma_{LV}^{D} \tag{11}$$

Octane has been used as reference for dispersive interaction of water ($\gamma_{WV}^{D} = \gamma_{OV}$). The polar interaction should be understood as the contribution of arrested polar molecules. Two straight-forward alternatives for averaging the dispersive work of solid-liquid adhesion are [1]:

$$\text{Geometric average}: W_{SL}^{G} = 2\sqrt{\sigma_{SV}^{D}\gamma_{LV}^{D}} \tag{12a}$$

$$\text{Arithmetic average}: W_{SL}^{A} = \sigma_{SV}^{D} + \gamma_{LV}^{D} \tag{12b}$$

When combined with the previous expression for work of adhesion (10b) we can extract an corresponding expressions for interfacial energies [1] as:

$$\text{Geometric average}: \sigma_{SL}^{G} = \sigma_{SV}^{D} + \gamma_{LV}^{D} - 2\sqrt{\sigma_{SV}^{D}\gamma_{LV}^{D}} = \left(\sqrt{\sigma_{SV}^{D}} - \sqrt{\gamma_{LV}^{D}}\right)^2 \tag{13a}$$

$$\text{Arithmetic average}: \sigma_{SL}^{A} = \sigma_{SV}^{D} + \gamma_{LV}^{D} - \left(\sigma_{SV}^{D} + \gamma_{LV}^{D}\right) = 0 \tag{13b}$$

The geometric average shows that dispersive interaction is always positive (attraction) whatever the solid and liquid contributions are. Eq. (13b) shows that the definition of arithmetic adhesion average is obviously incomplete. Combining geometric work of adhesion (10b) with eq. (12a) we obtain a mean to determine the dispersive energy of solids by measuring contact angles of oils on model solids as:

$$2\sqrt{\sigma_{SV}^{D}\gamma_{LV}^{D}} = \gamma_{LV}^{D}\left(cos\Theta_{SL}^{D} + 1\right) \quad \Leftrightarrow \quad \sigma_{SV}^{D} = 0.25\gamma_{LV}^{D}\left(cos\Theta_{SL}^{D} + 1\right)^2 \tag{14}$$

where $\gamma_{LV}^{D} = \gamma_{OV}$ and $cos\Theta_{SL}^{D} = \cos\Theta_{SO}$. Table 1 shows that not all apparently dispersive probe liquids behave according to this model.

Note that (dispersive) surface tension and thereby liquid cohesion of α-bromonaphtalene and diiodomethane are about double as large as those of octane and hexadecane. Consequently, the use of halocarbons results in considerable larger surface energies of the model solids. An intrinsic test for applicability of Eq. (14) is provided by [1]:

$$cos\Theta_{SL}^{D} = -1 + 2\sqrt{\frac{\sigma_{SV}^{D}}{\gamma_{LV}^{D}}} \tag{15}$$

A straight line should be obtained when $cos\Theta_{SL}^{D}$ is plotted against $1/\sqrt{\gamma_{LV}^{D}}$ for several probe oils. The requirement that the line should pass −1 at $1/\sqrt{\gamma_{LV}^{D}} = 0$ is not fulfilled by the liquids in Table 1. One reason may be the neglected slightly acidic contribution of halocarbons.

2.4. Specific solid-liquid interactions

The simple division of surface energies into dispersive and polar parts was deemed insufficient. Van Oss, Chadhury and Good developed a method to expand this concept [6,7]. The weak acidic interactions described above were accounted for by formally redefining (London) dispersive interactions to include all Lifshitz-van der Waals interactions ($\sigma_{SV}^{LW} \approx \sigma_{SV}^{D}$). The weak acidity of halocarbons (α-BN, DIM) are then a natural part of this enlarged Lifshitz-van der Waals non-polarity. All polar molecules were then assigned both Lewis acidic and basic sites (bidentacy), which interact mutually upon contacts (very small distances). The acid-base interfacial tension of liquid sites and interfacial energy of solid sites are then, according to vOCG model defined as geometric average of intrinsic Lewis acid (electron acceptor) and base (electron donor) contributions [1,6–8] as:

$$\gamma_{LV}^{AB} = \gamma_{LV} - \gamma_{LV}^{LW} = 2\sqrt{\gamma_{LV}^{A}\gamma_{LV}^{B}} \quad \Leftrightarrow \quad C_{LL}^{AB} = 2\gamma_{LV}^{AB} \tag{16a}$$

$$\sigma_{SV}^{AB} = \sigma_{SV} - \sigma_{SV}^{LW} = 2\sqrt{\sigma_{SV}^{A}\sigma_{SV}^{B}} \quad \Leftrightarrow \quad C_{SS}^{AB} = 2\sigma_{SV}^{AB} \tag{16b}$$

These Lewis acid-base interfacial components are commonly used to define Brϕnsted hydrogen bond capacity. The acid-base cohesion is, as usual twice these values. Since the dispersive = Lifshitz-van der Waals component of α-bromonaphtalene and diiodomethane are twice as large as those of octane and hexadecane, the corresponding acid-base component of polar liquids are half of those of octane and hexadecane. The work of adhesion is defined as the sum of bidentate acid-base interactions [1,6–8]:

$$W_{SL}^{AB} = W_{SL} - W_{SL}^{LW} = 2\left(\sqrt{\sigma_{SV}^{A}\gamma_{LV}^{B}} + \sqrt{\sigma_{SV}^{B}\gamma_{LV}^{A}}\right) \tag{17a}$$

$$W_{SL}^{AB} = \sigma_{SV}^{AB} + \gamma_{LV}^{AB} - \sigma_{SL}^{AB} \tag{17b}$$

Table 2
Total, Lifshitz-van der Waals (*LW*, Table 1), acid-base (*AB*), acid (*A*), and base (*B*) compo-nents determined for water (W), formamide (FoAm), ethylene glycol (EG'ol) and with (O = octane, H = hexadecane, B = α-bromonaphtalene and D = diiodomethane, Table 1) probe oils on silica and titania solids (pi = hydrophilic, po = hydrophobized by dichlorodimethylsilane in xylene) [8].

		γ_{LV} mN/m	γ^{LW} mN/m	γ^{AB} mN/m	γ^{A} mN/m	γ^{B} mN/m						
Water	W	72.8	21.8	51.0	25.5	25.5						
FoAm	F	58.0	39.0	19.0	2.28	39.6						
EG'ol	E	48.0	29.0	19.0	1.92	47.0						
		σ_{SV} mJ/m^2	σ^{LW} mJ/m^2	σ^{AB} mJ/m^2	σ^{A} mJ/m^2	σ^{B} mJ/m^2		σ_{SV} mJ/m^2	σ^{LW} mJ/m^2	σ^{AB} mJ/m^2	σ^{A} mJ/m^2	σ^{B} mJ/m^2
SiO_2-po	OWF	NA	22.2	NA	NA	NA	OWE	23.2	22.2	1.01	0.03	8.94
SiO_2-pi	OWF	55.3	22.2	33.2	8.39	32.7	OWE	45.2	22.2	23.0	2.73	48.5
TiO_2-po	OWF	29.2	22.2	7.04	0.50	24.8	OWE	26.8	22.2	4.59	0.19	27.6
TiO_2-pi	OWF	53.6	22.2	31.4	7.16	34.5	OWE	43.4	22.2	21.2	2.27	49.6
SiO_2-po	HWF	NA	23.3	NA	NA	NA	HWE	23.8	23.3	0.48	0.01	8.82
SiO_2-pi	HWF	54.6	28.1	26.5	5.27	33.4	HWE	44.7	28.1	16.6	1.45	47.1
TiO_2-po	HWF	29.2	28.4	0.81	0.01	25.4	HWE	28.7	28.4	0.27	0.00	26.4
TiO_2-pi	HWF	52.7	28.4	24.3	4.21	35.1	HWE	42.9	28.4	14.5	1.09	48.1
SiO_2- po	BWF	NA	24.6	NA	NA	NA	BWE	24.7	24.6	0.09	0.00	8.69
SiO_2- pi	BWF	54.7	39.6	15.2	1.68	34.4	BWE	45.8	39.6	6.25	0.22	44.8
TiO_2-po	BWF	NA	38.0	NA	NA	NA	BWE	NA	38.0	NA	NA	NA
TiO_2-pi	BWF	52.8	44.3	8.50	0.50	36.5	BWE	44.9	44.3	0.62	0.00	44.9
SiO_2-po	DWF	NA	21.7	NA	NA	NA	DWE	23.0	21.7	1.25	0.04	9.00
SiO_2-pi	DWF	54.8	40.7	14.1	1.45	34.5	DWE	46.0	40.7	5.33	0.16	44.6
TiO_2-po	DWF	NA	40.2	NA	NA	NA	DWE	NA	40.2	NA	NA	NA
TiO_2-pi	DWF	52.9	45.3	7.61	0.40	36.6	DWE	45.4	45.3	0.12	0.00	44.8

If one of the acid-base pairs is monodentate the corresponding term is set equal to zero. The interfacial energy is, according to vOCG model obtained from rearranged work of adhesion [1,6–8] as:

$$\sigma_{SL}^{AB} = \sigma_{SV}^{AB} + \gamma_{LV}^{AB} - 2\left(\sqrt{\sigma_{SV}^{A}\gamma_{LV}^{B}} + \sqrt{\sigma_{SV}^{B}\gamma_{LV}^{A}}\right) \tag{18a}$$

$$\sigma_{SL}^{AB} = 2\left(\sqrt{\sigma_{SV}^{A}\sigma_{SV}^{B}} + \sqrt{\gamma_{LV}^{A}\gamma_{LV}^{B}}\right) - 2\left(\sqrt{\sigma_{SV}^{A}\gamma_{LV}^{B}} + \sqrt{\sigma_{SV}^{B}\gamma_{LV}^{A}}\right) \tag{18b}$$

$$\sigma_{SL}^{AB} = 2\left[\left(\sqrt{\sigma_{SV}^{A}} - \sqrt{\gamma_{LV}^{A}}\right)\left(\sqrt{\sigma_{SV}^{B}} - \sqrt{\gamma_{LV}^{B}}\right)\right] \tag{18c}$$

Eq. (18c) implies that the acid-base interaction is repulsive if $\gamma_{LV}^{A} > \sigma_{SV}^{A}$ and if $\gamma_{LV}^{B} < \sigma_{SV}^{B}$. The reverse conditions also apply. When the dispersive interaction has been determined by contact angle measurements with oils (Eq.(14)), the acid-base interaction of two polar probe liquids *W* (water) and *L* with the solid can be determined [1,6–8] as:

$$W_{SW}^{AB} = W_{SW} - 2\sqrt{\sigma_{SV}^{LW}\gamma_{WV}^{LW}} = C\sqrt{\sigma_{SV}^{A}(W)} + D\sqrt{\sigma_{SV}^{B}(W)} \tag{19a}$$

$$W_{SL}^{AB} = W_{SL} - 2\sqrt{\sigma_{SV}^{LW}\gamma_{LV}^{LW}} = E\sqrt{\sigma_{SV}^{A}(L)} + F\sqrt{\sigma_{SV}^{B}(L)} \tag{19b}$$

where $W_{SW} = \gamma_{WV}(\cos\Theta_{SW} + 1)$, $W_{SL} = \gamma_{LV}(\cos\Theta_{SL} + 1)$, $C = 2\sqrt{\gamma_{WV}^{B}}$, $D = 2\sqrt{\gamma_{WV}^{A}}$, $E = 2\sqrt{\gamma_{LV}^{B}}$ and $F = 2\sqrt{\gamma_{LV}^{A}}$. Since $\sigma_{SV}^{A}(W) = \sigma_{SV}^{A}(L)$ and $\sigma_{SV}^{B}(W) = \sigma_{SV}^{B}(L)$, the acid and base component of solid sites may be derived [1,6–8] as:

$$\sqrt{\sigma_{SV}^{A}} = \frac{W_{SW}^{AB}F - W_{SL}^{AB}D}{CF - DE} \tag{20a}$$

$$\sqrt{\sigma_{SV}^{B}} = \frac{W_{SL}^{AB}C - W_{SW}^{AB}E}{CF - DE} \tag{20b}$$

The surface energy components for pure and hydrophobized SiO_2 and TiO_2 calculated using this procedure with a range of liquids are presented in Table 2.

As shown, surface energy components are rather dependent on the probe liquids chosen for vOCG model analysis. The problem with this method is that it may produce negative square root surface energy components which are squared artificially to provide positive values. For an intrinsic consistency test the acid-base adhesion can be back-calculated [8] as:

$$W_{SW}^{AB} = (cos\Theta_{SW} + 1) - 2\sqrt{\sigma_{SV}^{LW}\gamma_{WV}^{LW}} \tag{21a}$$

$$W_{SL}^{AB} = (cos\Theta_{SL} + 1) - 2\sqrt{\sigma_{SV}^{LW}\gamma_{LV}^{LW}} \tag{21b}$$

for comparison. If acid-base adhesion calculated from Eqs. (19a) and (19b) do not agree with those calculated from Eqs. (21a) and (21b) the results should be abandoned. A comprehensive evaluation of the vOCG procedure has been published elsewhere [8].

2.5. Equilibrium work of spreading

Work of adhesion characterizes interaction between liquids (sessile drop) and solid surface (vertical interaction). Equilibrium work of spreading characterizes the potential surface energy for spreading liquids (sessile drops) along surfaces (horizontal interaction). The work of spreading was defined by eq. (10c) as work of adhesion reduced by work of cohesion of probe liquids. If vapor molecules adsorb on the surface, it creates a surface pressure which reduces work of spreading [1] as:

$$S_{S(V)L} = \sigma_{SV} - \gamma_{LV} - \sigma_{SL} = \sigma_{S(0)} - \gamma_{L(0)} - \sigma_{SL} - \pi_{S(V)} = S_{S(0)L} - \pi_{S(V)} \tag{22a}$$

where $\sigma_{S(0)}$ is the surface energy of the bare (vapor free) solid surface and $S_{S(0)L} = S_{SL}$. Surface pressure may be expressed in terms of chemical potential of vapor [1] as:

$$\pi_{S(V)} = \sigma_{S(0)} - \sigma_{S(V)} = \int_{0}^{sat} \Gamma_V d\mu_V \tag{22b}$$

Adsorption isotherms have been designed to characterize the state of adsorbent (vapor). *Langmuir adsorption equation* represents localized adsorption without lateral interaction and can be expressed in terms of surface pressure [4,9,10] as:

$$\pi a_m = -kT\ln(1-\theta) \approx kT\theta \quad \Leftrightarrow \quad \pi_L = -\frac{kT}{a_m}ln(1-\theta) \approx \frac{kT\theta}{a_m} \tag{23}$$

where $\theta = (N_{ads}/N^{S})$ = surface coverage and a_m = molecular cross-section or site area [m^2]. Eq. (23) applies for very low surface coverage.

Frumkin-Fowler-Guggenheim (FFG) equation adsorption isotherm expands Langmuir equations to include local adsorption with lateral interaction. Expressed in terms of surface pressure it takes the form [4,9,10]:

$$\pi_{FFG}\, a_m = -kTln(1-\theta) + \frac{N_c \omega_{ii}}{2}\theta^2 \quad \Leftrightarrow \quad \pi_{FFG} = \pi_L + \frac{N_c \omega_{ii}}{2a_m}\theta^2 \tag{24}$$

where ω_{ii} = pair interaction energy and N_c = coordination number. It includes the approxi-mation that lateral interaction has no consequences for the configurational entropy of the lattice.

Volmer equation adsorption isotherm characterizes surface layers with mobile molecules without lateral interactions [4,9,10] as:

$$\pi_V\, a_m = kT\left(\frac{\theta}{1-\theta}\right) \approx kT\,\theta \quad \Leftrightarrow \quad \pi_V = \frac{kT}{a_m}\left(\frac{\theta}{1-\theta}\right) \approx \frac{kT\theta}{a_m} \tag{25}$$

For low coverages Volmer ($\theta/(1-\theta) \approx \theta$) and Langmuir ($-\ln(1-\theta) \approx \theta$) are nearly equal, but at higher surface coverages (θ) the difference increases.

Hill-de Boer equation adsorption isotherm [4,9,10] expands Volmer equation to include lateral interaction. It may be expressed in terms of surface pressure as:

$$\pi_{HdB}\, a_m = kT\left(\frac{\theta}{1-\theta}\right) - \frac{a^s_{vdW}}{a_m}\theta^2 \quad \Leftrightarrow \quad \pi_{HdB} = \pi_V - \frac{a^s_{vdW}}{a_m^2}\theta^2 \tag{26}$$

where van der Waals constant of two-dimensional gases is denoted a^s_{vdW}. According to this theory monolayer completion occurs slowly, but eventually a phase transition takes place.

Brunauer-Emmett-Teller (BET) adsorption isotherm is, alike Langmuir isotherm based on localized monolayer adsorption. However BET isotherms allow for additional adsorption to mobile vapor multilayers. Expressed in terms of surface pressure we find [4,9,10] that:

$$\theta = \frac{Cx}{[1+(C-1)x](1-x)} \quad \Leftrightarrow \quad \pi_{BET} = \frac{kT}{a_m}\left[\frac{1+(C-1)x}{1-x}\right] \tag{27}$$

where $x = p_V/p_{sat}$ and $\ln C \approx (\Delta_{ads}U - \Delta_{cond}U)/RT$. Plotted as V_{ads}/V_{mon} as a function of x the curves bend increasingly upwards for $C < 1.0$, but an initial opposite bend (hump) is observed before the upward bend is restored for increasing $C > 1.0$ (revisited later).

Work of spreading (Eq.(10c)) may be generalized to allow for vapor adsorption [1] as:

$$S_{S(V)L} = \gamma_{LV}\left(cos\Theta_{S(V)L} - 1\right) = \gamma_{LV}(cos\Theta_{SL} - 1) - \pi_{S(V)} \tag{28a}$$

Surface pressure of vapor films may be determined by measuring contact angles in the absence (Θ_{SL}) and presence ($\Theta_{S(V)L}$) of vapor films [1]:

$$\pi_{S(V)} = S_{SL} - S_{S(V)L} = \gamma_{LV}\left(cos\Theta_{SL} - cos\Theta_{S(V)L}\right) \tag{28b}$$

2.6. Summary

Classical thermodynamics provides a straightforward mean to characterize partial wetting (sessile liquid drop on ideal solid surfaces) in terms of work of cohesion, work of adhesion and work of spreading.

The overall surface tension of liquids may be divided into dispersive, polar, and Lewis-type acid and base contributions including Brϕnsted type hydrogen bonding. This enables determination of corresponding components of solid surface energy.

The surface and interfacial components are experimentally accessible by measurements of contact angles of probe liquids. The choice of probe liquids has a significant influence on determined surface energies.

Adsorption of vapor on solids reduces surface energy of bare solids. The nature of vapor-solid and vapor-vapor interactions can be evaluated using adsorption isotherms expressed in terms of surface pressure.

3. Vapor film adsorption and spreading

Previous section was focused on macroscopic equilibrium wetting properties. Surface pressure indicated the presence of molecular dynamics. In this section attention is on such processes.

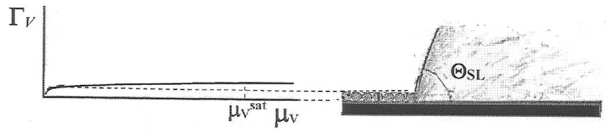

Fig. 2. Schematic illustration of the relationship between surface excess and vapor diffusion from three-phase contact-line (*tpcl*) of a sessile drop.

3.1. Diffusive molecular spreading

The best-known molecular transport is by diffusion. For two-dimensional vapor (V) diffusion, we write the normalized molecular surface (s) transport as:

$$\frac{dn^s_V/dt}{L_\varphi} = \frac{d(A_S\Gamma_V)/dt}{L_\varphi} = \frac{A_S}{L_\varphi}\left(\frac{d\Gamma_V}{dt}\right) + \Gamma_V\frac{d(A_S/L_\varphi)}{dt} \tag{29}$$

where L_φ is length of diffusion front (radial perimeter length), n^s amount of adsorbed substance (vapor) and $\Gamma_V = n^s_V/A_S$ surface excess. The two-dimensional vapor (V) diffusion from a sessile drop is illustrated in Fig. 2.

Assuming radial diffusion, the surface transport consists of a diffusive component defined [4,11] as:

$$\frac{A_S}{L_\varphi}\left(\frac{d\Gamma_V}{dt}\right) = \frac{\pi R^2_{base}}{2\pi R_{base}}\left(\frac{d\Gamma_V}{dt}\right) = \frac{R_{base}}{2}\left(\frac{d\Gamma_V}{dt}\right) \tag{30}$$

and a convective component defined as:

$$\Gamma_V\frac{d(A_S/L_\varphi)}{dt} = \frac{\Gamma_V\pi R_{base}}{2\pi R_{base}}\left(\frac{dR}{dt}\right) = \frac{\Gamma_V}{2}v_V \tag{31}$$

The total radius may be expressed by the sum of base radius (r_{base}) and the extension of diffused vapor r_{diff}, $R_{base} = r_{base} + r_{diff}$. The contribution of diffusion can be related to Fick's first law [4,11] as:

$$\frac{R_{base}}{2}\left(\frac{d\Gamma_V}{dt}\right) = D^s_\Gamma\left(\frac{d\Gamma_V}{dR_{base}}\right) \approx D^s_\Gamma\left(\frac{\Delta\Gamma_V}{R_{base}}\right) \tag{32}$$

where D^s_Γ denotes two-dimensional diffusion coefficient. It is customary to maintain the unit (m^2/s) of the three-dimensional diffusion coefficient in the two-dimensional case [4]. Eq. (32) may be reorganized and integrated to yield Einstein relationship as:

$$\int R_{base}dR = 2D^s_\Gamma\int t \quad \Leftrightarrow \quad R^2_{base} = 4D^s_\Gamma t \quad \Leftrightarrow \quad \frac{dR^2_{base}}{dt} = 4D^t_\Gamma \tag{33}$$

In condensed media surface diffusion is intimately connected with bulk diffusion in a mixed transport. The characteristic radius of three-dimensional and one-dimensional diffusions are:

$$R_\Gamma = \sqrt{6D^s_\Gamma t} \tag{34a}$$

$$R_\Gamma = \sqrt{2D^s_\Gamma t} \tag{34b}$$

The following diffusion constants have been reported for water on a silica sample (Spherisorb S20W) with a specific surface area $A_S = 232$ m^2/g and site density $N^s_\lambda = 4.60$ OH-groups/nm^2 ($4.60{*}10^{18}$ m^{-2}) [12]:

$${}^*D^s_\Gamma(localized) = 1{\cdot}10^{-10}\ m^2/s$$

$${}^*D^s_\Gamma(2D-mobile) = 6{\cdot}10^{-10}\ m^2/s$$

The following two-dimensional translation time, $t_{translation} = 6{*}10^{-11}$ s ($t_o = 1/\kappa_o$) and translational jump distance 0.3 nm were found. Moreover, it is estimated that $4D^s_\Gamma \approx D_c$ which compares quite well with published surface diffusion constant for water [11]:

$${}^*D^s_{aq} = 2.3{\cdot}10^{-9}\ m^2/s$$

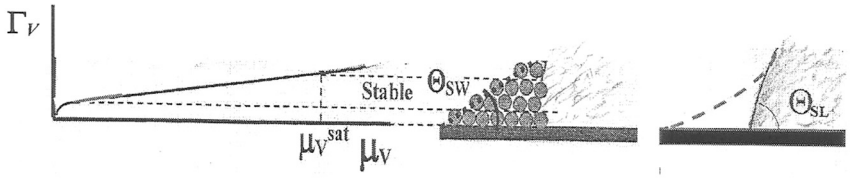

Fig. 3. Schematic illustration of the relationship between chemical potential dependent vapor surface excess (adsorption) and formation of an asymptotic vapor wedge at three-phase contact-line (*tpcl*).

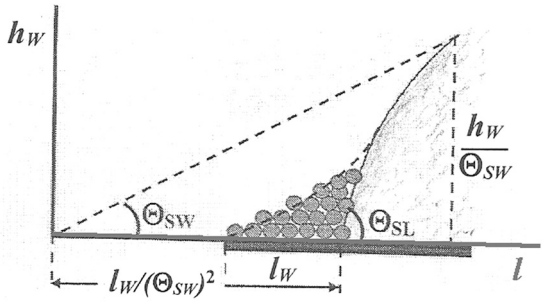

Fig. 4. Characteristic features of the asymptotic vapor wedge profile in the vicinity of three-phase contact-line (*tplc*) [5,13].

Inserted in eq. (33) water diffuses $0.63 < R/\text{nm} < 1.55$ in 1 ns on surfaces as compared to 3.71 nm in 1 ns in bulk.

3.2. Vapor clustering – thin films

Due to vapor condensation the three-phase-contact-line (*tpcl*) around the drop fluctuates as a function of thermal gradients and convection (see diffusive vapor transport). When contact angle is small (solid-vapor interaction is large) the vapor clustering at *tpcl* gives rise to a vapor wedge. Fig. 3 illustrates the equilibrium between vapor and condensed liquid states. The vapor pressure was expressed in terms of molecular state by Langmuir (Eq.(23)), Frumkin-Fowler-Guggenheim (Eq.(24)), Volmer (Eq.(25)) and Hill-de Boer (Eq.(26)) adsorption isotherms.

Despite normally negligible extension, the wedge height may be observed on solid surfaces when contact angles are very small. Fig. 4 illustrates the relationships between wedge height, length, and contact angle.

De Gennes established a relationship which describes the asymptotic wedge at three-phase contact-line (*tplc*) [5,13] as:

$$h_W^2 = \Theta_{SW}^2 l^2 - \frac{l_W^2}{\Theta_{SW}^2} \tag{35}$$

where the limiting molecular cut-off value (hydrophobic liquid wedge extension) is defined as, $l_W = \sqrt{H_{SL}/6\pi\gamma_L} \approx 0.1$ nm (H_{SL} = Hamaker constant [2,3]). One reviewer pointed out that accurate considerations of the microscopic and macroscopic contact angles has been published by Ruckenstein E. and Berim GO. in Advances in Colloid and Interface Science, 157 (2010) 1–33.

3.3. Molecular-kinetic (MK) model

Micro/nanoscopic wetting occurs when surface sites are separated λ /nm apart and thermal fluctuations may result in jumps over one or several surface sites. The molecular kinetic theory by Blake and Haynes [14] describes the three-phase contact-line (*tpcl*) movement of molecular assemblies as a dynamic stress-modified molecular rate process. Fluctuations at *tpcl* are described as statistical events of molecular displacements around mean. It involves adsorption of molecules from the advancing liquid front or sessile drop and concurrent desorption of molecules of the receding liquid. When the contact angle is sufficiently small (solid-vapor interaction sufficiently large) a liquid wedge develops, and the adjoining sessile drop can be considered a thin film. The molecular-kinetic model was originally developed by Glasstone and coworkers [15]. The adsorption of evaporated molecules occur at evenly distributed adsorption sites at distance λ from each other. The number of adsorption sites per unit area is given by, $N_\lambda^s = N^s/\lambda^2$. The adsorption is characterized by kinetic equilibrium constants (hopping frequencies) for both the advancing (κ_A [1/s]) and the receding (κ_R [1/s]) liquids. The rate of liquid movement at *tpcl* is thus: $v_{tpcl} = \kappa\lambda$. Three-phase contact-line (*tpcl*) movement is driven by half of time-dependent vapor surface pressure ($\pi_{S(V)}^t/2$), both in the forward (wetting) and backward (dewetting) directions. The work performed per adsorption site at the advancing front is identified as ($W_{cap}^s/2N_\lambda^s = \pi_{S(V)}^t/2N_\lambda^s$, expressed in Joules). The total pseudo-equilibrium (steady state) constant can then be defined [14,16] as:

$$\kappa_{tpcl} = \kappa_{tpcl}^A + \kappa_{tpcl}^R = \kappa_{tpcl}^0 \left[exp\left(\frac{W_{cap}^s}{2N_\lambda^s kT}\right) - exp\left(\frac{-W_{cap}^s}{2N_\lambda^s kT}\right) \right] \tag{36}$$

where k is the Boltzmann constant. The rate (velocity) of wetting is obviously [16]:

$$v_{tplc} = \kappa_{tpcl}\lambda = 2\kappa_{tpcl}^0 \lambda sinh\left(\frac{W_{cap}^s}{2N_\lambda^s kT}\right) = 2\kappa_{tpcl}^0 \lambda sinh\left(\frac{\pi_{S(X)}^t}{2N_\lambda^s kT}\right) \tag{37}$$

where $v_{tpcl}^0 = \kappa_{tpcl}^0\lambda = \lambda/t_0 (t_0 = \text{relaxation time})$. For irregular menisci (as in line tension) the rate may deviate considerably from the ideal case. For liquid wetting the surface (capillary) work is replaced by dynamic surface pressure:

$$\pi_{S(X)}^t = \gamma_{LV}\left(cos\Theta_{S(X)L}^0 - cos\Theta_{S(X)L}^t\right) \tag{38}$$

where lower index $X = V$ (vapor) for advancing and $X = F$ (film) for receding processes. The corresponding equilibrium surface pressure was introduced previously (Eqs.(28)–(26)). Note that extrapolated $\Theta_{S(X)L}^0$ does not necessarily correspond to the equilibrium (Young, $\Theta_{S(X)L}^Y$) contact angle. The dependence of surface pressure on wetting rate is then given (sinh$x \approx x$) by:

$$\frac{d\pi_{S(X)}^t}{dv_{tpcl}} = \frac{N_\lambda^s kT}{\kappa_{tpcl}^0 \lambda} \tag{39}$$

where only κ^0 and N_λ^s are unknown. It is known that advancing contact angles (dry surface wetting, $\Theta_{SL}^t \rightarrow \Theta_{S(V)L}^A$) increase and receding angles (wetted surface, $\Theta_{SL}^t \rightarrow \Theta_{S(F)L}^R$) decrease with an increased rate of *tpcl* displacement. Contact angles of ethylene glycol and water may be determined with an ultra-rapid camera as a function of time on paper as drop profile height (h_d) and base diameter ($d_d = 2r_{base}$) [11,17] as:

$$\Theta_{S(X)L}^t = 2arctan\left(\frac{h_d^t}{r_{base}^t}\right) = 2arctan\left(\frac{2h_d^t}{d_d^t}\right) \tag{40a}$$

The intrinsic consistency of contact angles was checked by determining drop volume from same parameters as:

$$V_d = \frac{\pi h_d}{6}\left(3r_{base}^2 + h_d^2\right) \tag{40b}$$

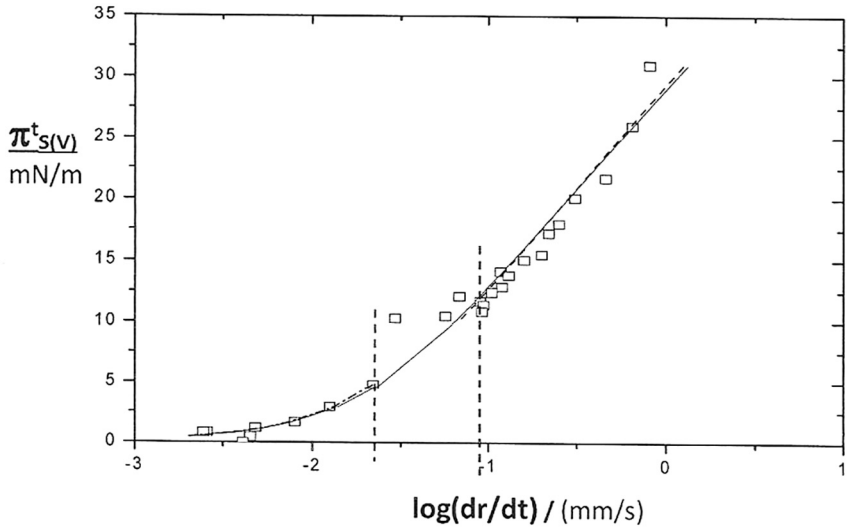

Fig. 5. Double exponential molecular kinetic model (Eq. (36), rate potted on log scale) applied to ethylene glycol spreading (advancing) on model OS1 paper (Table 1). A fit to the low spreading rate section (left, dash-dotted line) gives: $\kappa^0 = 1.0{*}10^7$ s^{-1}, $\lambda = 1.2$ nm and $N^s_\lambda = 0.7$ nm^{-2}. The high spreading rate section (right, dashed line) gives: $\kappa^0 = 1.6{*}10^8$ s^{-1}, $\lambda = 0.6$ nm and $N^s_\lambda = 2.6$ nm^{-2}. A slip-stick region appears between these limits as indicated with vertical broken lines. A fit to all experimental points gives: $\kappa^0 = 3.6{*}10^7$ s^{-1}, $\lambda = 1.0$ nm and $N^s_\lambda = 1.1$ nm^{-2} [17].

Only when the monitored time dependent drop volume remained roughly constant contact angles are acceptable. A model paper was characterized by $S_q = 116$ nm, $S_{dr} = 47.3\%$ and $r = 1.196$ [17]. The fit of eq. (36) to experimental data within low-, high- and overall v_L-ranges is illustrated in Fig. 5.

The λ and N^s_λparameters are quite reasonable as compared to ideal model systems for which $\kappa = 10^6$ s^{-1} of molecular relaxation and $\lambda \approx d_L$. Unfortunately the extracted κ^0 are found to be too high by orders of magnitude. Typical values for water on poly(ethylene terephtalate) (PET) determined with Wilhelmy plate [18] and optical data [14,16] methods using eq. (48) are: $0.95 < N^s_\lambda/(1/\text{nm}^2) < 1.00$, $0.99 < \lambda/\text{nm} < 1.00$, $2.0{*}10^5 < \kappa^0/(1/\text{s}) < 1.3{*}10^6$ and $97.5 < E^\#_m/(\text{kJ/mol}) < 41.9$. Most values are very similar to those in Fig. 5. However, the rate constants obtained from Wilhelmy plate forced wetting measurements (discussed later) are considerably greater in magnitude as compared to those obtained from optical measurements. As a result, the molar activation energy of wetting is different. In all cases the values indicate that at *tpcl* molecular displacements occur at a lower frequency than in bulk which influences molar activation energy.

At small displacement rates the liquid front gets pinned (within the slip-stick range) due to chemical, topographical or adsorptive heterogeneities. This disturbance can fully cover differ-rences found for molecular-kinetic parameters. According to Fig. 5 one can distinguish between two wetting mechanisms separated by the slip-stick region ($-1.7 < \log v_{tpcl}/(\text{mm/s}) < -1.1$, $v_{tpcl} = dr/dt$) [11,14,16,17]:

1. At low v_{tpcl} ($-3 < \log v_{tpcl}/(\text{mm/s}) < -1.7$) N^s_λ is expected to be small and the activation energy for wetting large. The small number of sites thus relates to a strong adsorbate-site interaction.
2. At high v_{tpcl} ($-1 < \log v_{tpcl}/(\text{mm/s}) < 0$) N^s_λ is expected to be large and the activation energy for wetting small. A large number of sites corresponds to a weak adsorbate-site interaction.

The site distance and equilibrium constant are then expected to be comparable to those of water diffusion on silica ($\lambda \approx 0.3$ nm and $\kappa_{trans} = 1/t_{trans} \approx 1.7{*}10^{10}$ s^{-1}) [12]. Two further limiting states can be introduced [11,14,16,17]:

1. If $\gamma_{LV}(\cos\Theta^a_{S(X)L} - \cos\Theta^t_{S(X)L}) \langle\langle 2N^s_\lambda kT$, i.e. when $\Theta^t_{SL} \to \Theta^a_{SL}$ eq.

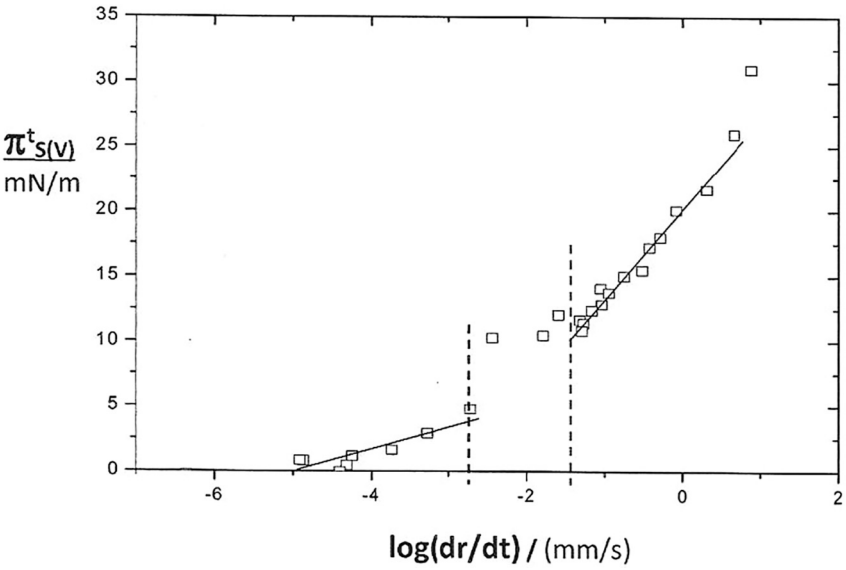

Fig. 6. Single exponential molecular kinetic model (rate plotted on ln-scale) applied on ethylene glycol spreading on OS2 paper. A fit to the low spreading rate section (Eq.41), left) resulted in the following fit parameters: $\kappa^0 = 4.69{*}10^8$ s^{-1}, $\lambda = 2.12$ nm and $N^s_\lambda = 0.22$ nm^{-2}. The high rate spreading section (Eq.(42), right) resulted in the following parameters: $\kappa^0 = 9.19{*}10^8$ s^{-1}, $\lambda = 1.08$ nm and $N^s_\lambda = 0.85$ nm^{-2}. The slip-stick region is indicated with vertical broken lines [11].

Table 3
Extracted molecular parameters from a non-linear fit of eq. (37) to rate spreading of 1.0 μl ethylene glycol on off-set papers OS1-OS4 [19]. Left four upper columns = low-rate fits, middle four columns = high-rate fits and right four columns all-rate fits. Linear (Eq.(42)) fit (lower left four columns) and non-linear fit (Eq.(37), lower middle columns) to the rate of spreading of 0.5 μl ethylene glycol on ink-jet papers IJ5-IJ8 [20].

	N_λ^s	λ^{MK}	κ_{tpcl}^o	$E_m^\#$	N_λ^s	λ^{MK}	κ_{tpcl}^o	$E_m^\#$	N_λ^s	λ^{MK}	κ_{tpcl}^o	$E_m^\#$
Paper	1/nm^2	nm	1/s	kJ/mol	1/nm^2	nm	1/s	kJ/mol	1/nm^2	nm	1/s	kJ/mol
OS1	0.7	1.2	$1.0*10^7$	33	2.6	0.6	$1.6*10^8$	26	1.1	1.0	$3.6*10^7$	30
OS2	0.4	1.7	$4.7*10^6$	35	2.2	0.7	$1.3*10^8$	27	2.0	0.7	$9.2*10^7$	28
OS3	0.4	1.6	$7.6*10^6$	34	0.6	1.2	$1.1*10^8$	27				
OS4	0.7	1.2	$2.8*10^7$	31	0.5	1.4	$5.2*10^7$	29				
IJ5	0.39	1.6	$2.0*10^4$	47.5	0.25	2.0	$4.1*10^3$	51.5				
IJ6	0.18	2.9	$6.2*10^2$	56.1	0.08	3.5	$2.9*10^2$	57.9				
IJ7	0.30	1.8	$4.1*10^2$	57.1	0.40	1.6	$2.3*10^3$	52.9				
IJ8	0.20	2.3	$1.9*10^4$	47.8	0.16	2.5	$1.1*10^4$	49.0				

Table 4
Extracted molecular parameters from linear fits of eq. (42) to 0.5 μl water on ink-jet papers IJ5-IJ8 [20] (left four columns). Non-linear fits of eq. (37) to all rate spreading of 1.0 μl water on off-set papers OS1-OS4 [19]) and 0.5 μl water on ink-jet papers IJ5-IJ8 [20] (right four columns).

	N_λ^s	λ^{MK}	κ_{tpcl}^o	$E_m^\#$	N_λ^s	λ^{MK}	κ_{tpcl}^o	$E_m^\#$
Paper	1/m^2	nm	1/s	kJ/mol	1/m^2	Nm	1/s	kJ/mol
OS1					1.6	0.8	$1.0*10^8$	27.0
OS2					1.8	0.7	$2.1*10^8$	26.0
OS3					1.7	0.8	$1.6*10^7$	32.0
OS4					1.0	1.0	$1.5*10^7$	32.0
IJ5	0.42	1.54	$7.7*10^3$	50.0	0.71	1.19	$1.0*10^5$	43.7
IJ6	1.00	1.00	$3.3*10^3$	52.0	0.74	1.16	$1.6*10^3$	53.8
IJ7	6.36	0.40	$2.5*10^6$	35.9	0.74	1.16	$1.3*10^6$	37.5
IJ8	0.05	4.55	$2.3*10^1$	64.1	2.44	0.64	$2.8*10^3$	52.4

(36) can be simplified by expansion in series (sinh x = x + …) as:

$$\upsilon_{tpcl} = \kappa_{tpcl}^o \lambda^{MK} \left(\frac{\gamma_{LV}\left(cos\Theta_{S(X)L}^o - cos\Theta_{S(X)L}^t\right)}{N_\lambda^s kT} \right) \approx \frac{\kappa_{tpcl}^0 \lambda^{MK} \pi_{S(X)}^t}{N_\lambda^s kT} \tag{41}$$

This equation applies only at small wetting rates and should produce a linear $\cos\Theta_{S(X)L}^t$ - υ_{tpcl} dependence.

2. If $\gamma_{LV}(\cos\Theta_{S(X)L}^o - \cos\Theta_{S(X)L}^t) \rangle\rangle 2N_\lambda^s kT$, i.e. when $\upsilon_{tpcl} > 0$ the reverse reaction κ_R can be neglected and eq. (48) can be simplified ($e^x = 1 + x + \cdots$) as:

$$\upsilon_{tpcl} = \kappa_{tpcl}^o \lambda^{MK} exp\left(\frac{\gamma_{LV}\left(cos\Theta_{S(X)L}^o - cos\Theta_{S(X)L}^t\right)}{2N_\lambda^s kT} \right) \approx \approx \kappa_{tpcl}^0 \lambda^{MK} + \frac{\kappa_{tpcl}^0 \lambda^{MK} \pi_{S(X)}^t}{2N_\lambda^s kT} \tag{42}$$

In this case $\cos\Theta_{S(X)L}^t$ is expected to depend on ln υ_{tpcl}. If $\pi_{S(X)}^t = \gamma_{LV}(\cos\Theta_{S(X)L}^o - \cos\Theta_{S(X)L}^t)$ is plotted against ln υ_{tpcl} the slope is $2N_\lambda^s kT$ and the intercept is $\ln(\kappa_{tpcl}^0 \lambda)$ is obtained at $\pi_{S(X)}^t = 0$. The fit of eq. (41) for low velocities and eq. (42) for high velocities to experimental data is illustrated in Fig. 6.

The extracted parameters are as expected of the same magnitude but significantly different from those reported in Fig. 5. The quasi-equilibrium (steady state) rate constant κ^0 is related to the activation energy [16] as:

$$E^\# = -N_\lambda^s kT ln\left(\frac{\kappa_{tpcl}^0 h}{kT}\right) \tag{43}$$

where h is Planck's constant. Exchanging N_λ^s for Avogadros number provides a molar acti-vation energy ($E_m^\# = E^\# \cdot (N_A/N_\pi^s)$). The parameters N_λ^s, λ, κ_{tpcl}^o, $E^\#$ and $E_m^\#$ for ethylene glycol on OS1-OS4 papers, extracted with eq. (37) are listed in Table 3 and those extracted with eqs. (37) and (42) within high-υ_{tpcl} range in Table 4 for 1.0 μl and 0.5 μl sessile drops. Samples represent off-set [19] and samples IJ5-IJ8 ink-jet [20] papers.

The calculated parameters are somewhat dependent on both drop size and on spreading rate range investigated, as well as on the model applied.

Despite their very different use as off-set and ink-jet papers the parameters N_λ^s and λ are relatively similar. The expected similarity of distances between sites with the size of liquid molecules ($d_L < \lambda/\text{nm} < 1.0$) is roughly fulfilled [21]. The quasi-equilibrium (steady state) frequency, $\kappa_{tpcl}^0$and activation energies separate papers from each other. The rate constant is expected to lie between molecular relaxation ($\kappa = 10^6$ s^{-1}) and viscous dissipation ($\kappa = 10^{11}$ s^{-1}) [22]. Previously, the distance between hydroxyl sites on silica was found to be $\lambda = 0.3$ nm and two-dimensional (surface) translation frequency of water $\kappa = 1.7{\cdot}10^{10}$ s^{-1} [12]. Considering dielectric spectra, the IR resonance frequencies for bulk pentane-to-pentadecane is $8.50{\cdot}10^{13}$ s^{-1}, the UV resonance frequencies $2.94{\cdot}10^{13} < \nu/\text{s}^{-1} < 2.03{\cdot}10^{15}$ and for bulk water $\nu = 3.02{\cdot}10^{13}$ s^{-1} [23,24]. The electronic reference frequency for bulk pentane, water and alcohol is $\nu = 3.0{\cdot}10^{15}$ s^{-1}. The relaxation times may be considered as inverse resonance frequencies. The NMR relaxation frequency for surfactants is $10^2 < \nu/\text{s}^{-1} < 10^8$ increases with reduced hydrocarbon chain length [25].

3.4. Summary

On molecular level vapor spreading on surfaces may conveniently be characterized by diffusion. This provides references for values extracted from theoretical models.

Vapor clustering at *tpcl* gives rise to wedge formation which horizontal and vertical extension is characterized by an asymptotic function.

The dynamic properties of molecular displacement at *tpcl* is provided by molecular-kinetic (*MK*) model in terms of distance between sites, sites per unit surface, displacement (hopping) frequency and energy of activation. Unfortunately, it was found difficult to experimentally obtain physically acceptable values.

The observed unstable slip-stick wetting rate range cannot be explained by steady-state molecular-kinetic vapor displacement model.

4. Thin film formation and spreading

An increased partial vapor pressure beyond saturation results in formation of thin condensed surface films. Due to loss of one dimension of motion freedom vapor molecules arrange themselves in layers. The layering is enforced by van der Waals interaction which extends typically $1 < h_W/\text{nm} < 2$ [10,23,24]. Three layers of water has experimentally been observed on silica surface with a total thickness of $0.51 < h_W/\text{nm} < 0.54$. The upper limit of film thickness may, however, extend to up to seven or more vapor layers which is the maximum of long-range van der Waals interactions. These stratified layers are most common with fluids made of globular molecules. Surface pressure indicated the presence of dynamic molecules (Eqs.(25), (26)). In this section attention

is on thin film formation and spreading.

4.1. Thermodynamic considerations

Classical two-dimensional Gibbs' surface energy and work of spreading was introduced by eq. (10c) and it was extended to include monolayer vapor films by Eqs. (23)–(26). Adsorption of vapor on solid surfaces cannot occur beyond saturation. Instead, excess vapor condenses to films which are in equilibrium with sessile drops. It seems warranted to revisit dependencies of work of spreading and film pressures. The basic surface pressure is characterized by integrated vapor accumulation from $\Gamma = 0$ to $\Gamma = \infty$ [1]:

$$-\Delta_S G^s_{SL} = S_{SL} = S_{S(0)L} = \sigma_{S(0)} - \gamma_{L(0)} - \sigma_{SL} = \int_0^\infty \Gamma_V d\mu_V \tag{44a}$$

where lower index (0) refers to bare (vapor free) solid surfaces. Introducing Young eq. (8b) we find a way to determine work of spreading by measuring contact angles [1] as:

$$S_{SL} = S_{S(0)L} = \gamma_{L(X)}(cos\Theta_{SL} - 1) \tag{44b}$$

The surface tension and contact angle of liquids can, however not be determined in vacuum. Introducing a vapor pressure we find that:

$$\pi_{S(V)} = \sigma_{S(0)} - \sigma_{SV} = \int_0^{sat} \Gamma_V d\mu_V \tag{45a}$$

The relationship between work of spreading in the presence and absence of vapor monolayer may be expressed as:

$$-\Delta_S G^s_{S(V)L} = S_{S(V)L} = \sigma_{SV} - \gamma_{L(X)} - \sigma_{SL} = S_{S(0)L} - \pi_{S(V)} = \int_0^{sat} \Gamma_V d\mu_V \tag{45b}$$

Introducing Young equation (Eq.(28b)) we find a way to determine the work of spreading in presence of vapor by measuring contact angles:

$$S_{S(V)L} = \gamma_{L(X)}\left(cos\Theta_{S(V)L} - 1\right) \tag{45c}$$

Introducing film (F) pressure beyond vapor monolayer as:

$$\pi_{S(F)} = \sigma_{SV} - \sigma_{SF} = \sigma_{S(0)} - \sigma_{SF} - \pi_{S(V)} = \int_{sat}^\infty \Gamma_V d\mu_V \tag{46a}$$

The work of spreading in presence of thin films becomes:

$$-\Delta_S G^s_{S(F)L} = S_{S(F)L} = \sigma_{SF} - \gamma_{L(X)} - \sigma_{SL} = S_{S(V)L} - \pi_{S(F)} \tag{46b}$$

Introducing Young equation (Eq.(8b)) we find a way to determine the work of spreading by measuring contact angles:

$$S_{S(F)L} = \gamma_{L(X)}\left(cos\Theta_{S(F)L} - 1\right) \tag{46c}$$

Introducing eq. (45b) to eq. (46b) we find the work of spreading in presence and absence of thin films:

$$S_{S(F)L} = \sigma_{SF} - \gamma_{L(X)} - \sigma_{SL} = S_{S(0)L} - \pi_{S(V)} - \pi_{S(F)} \tag{46d}$$

Note that interfacial tension ($\gamma_{L(X)}$, $X = 0$, V, F) is considered to be little affected by the surrounding medium as compared to surface energy of solid. In summary, the work of spreading in the presence of thin films equals the work of spreading without these films reduced by (monolayer) vapor pressure and film pressure. Another view is that film pressure is measured from bare solid surface to macroscopic wetting (∞-limit). Thin films separating at $\mu > \mu_{sat}$ on solid surfaces do not initially possess liquid properties but are influenced by their contact with the solid. The influence of vertical interactions through adsorbed thin films is defined [4,5,9,26] as:

$$-\Delta_S G^s_{S(F)L} = S_{S(F)L} = \sigma_{SF} - \gamma_{L(X)} - \sigma_{SL} = -\int_{sat}^\infty \Pi_{S(F)} dh = \int_{sat}^\infty \Gamma_i d\mu_i \tag{47a}$$

where $i = V$, L and $\Pi_{S(F)}$ is expressed as N/m^2 and $\Delta_S G^s_{S(F)L}$as J/m^2. Combined with Young eq. (8b) we find a way to experimentally access the disjoining pressure as a modified work of spreading by measuring contact angles:

$$-\Delta_S G^s_{S(F)L} = S_{S(F)L} = \gamma_{L(X)}\left(cos\Theta_{S(F)L} - 1\right) = -\int_{sat}^\infty \Pi_{S(F)} dh = \int_{sat}^\infty \Gamma_i d\mu_i \tag{47b}$$

Derjaguin's disjoining pressure ($\Pi_{S(F)}$) is a linear combination of numerous contributions, such as liquid structure ($\Pi^{str}_{S(F)}$), van der Waals attraction($\Pi^{vdW}_{S(F)}$), electrostatic repulsion($\Pi^{el}_{S(F)}$), capillary suction ($\Pi^{cap}_{S(F)}$), and gravity($\Pi^{grav}_{S(F)}$) [5,26,27]:

$$\Pi_{S(F)} = \Pi^{str}_{S(F)} + \Pi^{vdW}_{S(F)} + \Pi^{el}_{S(F)} + \Pi^{cap}_{S(F)} + \Pi^{grav}_{S(F)} \tag{48}$$

Work of spreading was defined (Eq.(10c)) as the difference between vertical solid-liquid work of adhesion and horizontal work of liquid cohesion. Previously work of adhesion was divided into contributions of Lifshitz-van der Waals (London type dispersion, Eq.(12a)) and of Lewis type acid-base (polar, Eqs.(17a),(17b)) interactions. Since focus is on vertical solid-liquid film interactions, eq. (47) suggests that disjoining pressure is in fact related to work of adhesion as:

$$-\Delta_W G^s_{S(F)L} = W_{S(F)L} = -\int_{sat}^\infty \Pi_{S(F)} dh \tag{49}$$

The work performed at surface sites were previously expressed as dynamic surface pressure (Eq.(38)). Expressing work of adhesion (Eq. (10b)) and work of spreading (Eq.(10c)) as time-dependent functions and subtract them from their equilibrium states, we find (Eq.(38)) that:

$$\pi^t_{S(F)} = W^0_{S(F)L} - W^t_{S(F)L} = S^0_{S(F)L} - S^t_{S(F)L} = \pi^t_{S(F)} = \gamma_{LV}\left(cos\Theta^0_{S(F)L} - cos\Theta^t_{S(F)L}\right) \tag{50}$$

Eqs. (49) and (50) show that disjoining pressure ($\Pi_{S(F)}$) represents film pressure ($\pi_{S(F)}$) integrated over time-dependent film height

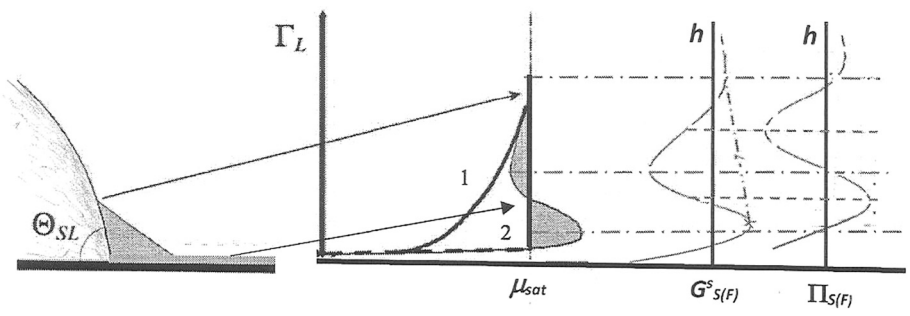

Fig. 7. Schematic illustration of surface excess dependence on chemical potential upon formation of thin films (middle diagram). Interaction through thin films (right diagram) on solid surfaces [5,10]. Curve 1 represents a continuously increasing surface excess equaling BET isotherms (Eq.(27)). Curve 2 characterizes a van der Waals loop. When $\mu > \mu_{sat}$, excess vapor is condensed to sessile drops. When $\mu < \mu_{sat}$ sub-monolayers form between sessile drops. The only observed transition at μ_{sat} is from saturated vapor thin α-films to condensed sessile drops of thick β-films.

(thickness) which may be included in the molecular-kinetic wetting model (Eq.(37)). The van der Waals contribution in Eq. (48) can therefore also be divided into contributions of van der Waals components such as;

$$\Pi^{vdW}_{S(F)} = \Pi^{D}_{S(F)} + \Pi^{P}_{S(F)} \quad \Leftrightarrow \quad \Pi^{vdW}_{S(F)} = \Pi^{LW}_{S(F)} + \Pi^{AB}_{S(F)} \tag{51}$$

The total vertical interaction expressed by Derjaguin's disjoining pressure (Eq.(47a)) can also be used to redefine the interfacial solid-film interfacial energy as:

$$\sigma_{SF} = \gamma_{L(X)} + \sigma_{SL} - \int_{sat}^{\infty} \Pi_{S(F)} dh = \gamma_{LV} + \sigma_{SL} - \Delta_S G^s_{S(F)L} \tag{52}$$

Previous extraction of geometrically averaged dispersive (Eqs.(13)) and acid-base (Eqs.(18)) components of interfacial energy contradicts, however an additive division of solid-film interfacial energy into partial (*D, P, A, B*) contributions.

When vapor saturation point is exceeded, transient van der Waals instability states appears which is illustrated by van der Waals loops. Such van der Waals loops were allowed for by Frumkin-Fowler-Guggenheim (FFG, Eq.(24)) and by Hill-de Boer (HdB, Eq. (26)) adsorption isotherms. These adsorption isotherms include mutual interaction between adsorbed vapor molecules. Fig. 7 quantifies vapor and thin film interactions in terms of vertical Gibbs interfacial (surface) interaction energy ($\Delta_S G^s_{S(F)L}$) and of Derjaguin's disjoining pressure ($\Pi_{S(F)}$).

Curve 1 may be represented by a BET isotherm (Eq.(27)) resulting in complete wetting. Curve 2 represents partial wetting which implies that initial adsorption of vapor occurs until it is saturated. This is followed by a fictive van der Waals loop at μ_{sat}characterized by metastability and spinodal decomposition. Stable states of the adsorbed film correspond to those segments of the isotherm for which, $d\mu_L/d\Gamma_L > 0$ (Fig. 7). In a closed system the adsorbed film at supersaturation pressure can be in equilibrium with a sessile drop. After passing meta- and unstable (spinodal decomposition) regions vapor condenses on the solid surface as a thick β-film at $\Gamma_L = \infty$ [5,10]. Unstable states correspond to those segments of the isotherm for which, $d\mu_L/d\Gamma_L < 0$. The transitory meta- and unstable film states are impossible (or extremely difficult) to determine experimentally. Derjaguin disjoining pressure is defined in terms of transversal Gibbs´ interaction energy [4,5,9,10,26] as:

$$\Pi_{S(F)} = -\left(\frac{\partial \Delta_S G^s_{S(F)L}}{\partial h}\right)_{P,T} \tag{53a}$$

where $\Pi_{S(F)}$ is expressed as N/m^2. Integration results in:

$$\Delta_S G^s_{S(F)L} = \int_{sat}^{\infty} \Pi_{S(F)} dh = -\int_{\infty}^{sat} \Pi_{S(F)} dh \tag{53b}$$

where $\Delta_S G^s_{S(F)L}$ is expressed as J/m^2. The latter equality considers that the liquid in the film is in equilibrium with vapor. Viewed from *h*-axis in Fig. 7 there are two minima (positive $\Delta_S G^s_{\min} \leftrightarrow \Delta_S G^s_{prim}$ at small *h* and $\Delta_S G^s_{\sec}$ at large *h*) and one maximum (negative $\Delta_S G^s_{\max}$). The extremes are a result of contributions from interaction forces. At exceedingly small $0 < h/\text{nm} < max$, structural and van der Waals forces dominate. At $\Delta_S G^s_{\max}$(electrostatic) repulsion dominates, and at very large *h* gravitation contributes significantly. Viewed from *h*-axis the extrema are identified [5,10] as:

$$\Pi_{S(F)} = 0 \quad \Leftrightarrow \quad \left(\frac{\partial \Delta_S G^s_{S(F)L}}{\partial h}\right)_{P,T} = 0 \tag{54}$$

There are inflection points [5,10] at:

$$\left(\frac{\partial \Pi_{S(F)}}{\partial h}\right)_{P,T} = 0 = -\left(\frac{\partial^2 \Delta_S G^s_{S(F)L}}{\partial h^2}\right) \tag{55}$$

Stability as a function of *h* for positive $\Delta_S G^s_{prim}$ and $\Delta_S G^s_{\sec}$ requires [5,10] that:

$$\Pi_{S(F)} = 0 \quad \Leftrightarrow \quad \left(\frac{\partial \Pi_{S(F)}}{\partial h}\right)_{P,T} < 0 \quad \Leftrightarrow \quad \left(\frac{\partial^2 G^h_{S(F)}}{\partial h^2}\right) > 0 \tag{56a}$$

Meta- and instability as a function of *h* at negative $\Delta_S G^s_{\max}$is identified [5,10] by:

$$\Pi_{S(F)} = 0 \quad \Leftrightarrow \quad \left(\frac{\partial \Pi_{S(F)}}{\partial h}\right)_{P,T} > 0 \quad \Leftrightarrow \quad \left(\frac{\partial^2 \Delta_S G^s_{S(F)L}}{\partial h^2}\right) < 0 \tag{56b}$$

A thin α-film (nm) separates at $\Delta_S G^s_{prim}$ which is in equilibrium with a thick β-film at $\Delta_S G^s_{\sec}$ (< 100 nm). The $\Delta_S G^s_{\max}$ excitation barrier must be overcome before $\alpha \leftrightarrow \beta$ phase transition can occur. The curve between inflection points corresponds to positive curvature with reference to *h*-axis and represent unstable films where spinodal decomposition of films to sessile drops occur. The curves between inflection points and α-phase limit ($\Delta_S G^s_{prim}$) in equilibrium with β- phase limit ($\Delta_S G^s_{\sec}$) are metastable films, which upon thermal agitation may decompose to α- and β-films. Self-evidently disjoining pressure influences contact angles [5,10,13,26,27].

4.2. Phenomenological parameters (numbers)

In this section we focus on properties of thin liquid films protruding from sessile drops. Here the vapor clustering has resulted in formation of thin films. As shown in Fig. 4 a sessile drop with sufficiently small contact angle may be in equilibrium with a multimolecular thin vapor wedge. For small droplets, which shape may be deformed by gravity the limiting acceptable size is given by capillary length:

$$L_{cap} = \sqrt{\frac{\gamma_{LV}}{\rho_L g}} \tag{57a}$$

where $\rho_{LV} \approx \rho_L$is the formal difference between liquid and vapor. The influence of gravity is compared to surface tension/energy by dimensionless Eötvö's or Bond number:

$$Bo = \frac{\rho_{LV} g\, l^2}{\gamma_{LV}} = \left(\frac{l}{L_{cap}}\right)^2 \tag{57b}$$

where *l* is a characteristic nanoscopic (molecular) length which is dependent on the scale of the system. The relative influence of viscous drag as compared to surface tension/energy is expressed by dimensionless capillary number:

$$Ca = \left(\frac{\eta_L}{\gamma_{LV}}\right) v_L = \frac{v_L}{v_{hd}} \tag{58}$$

The wetting rate is normalized (divided by) the characteristic hydrodynamic velocity v_{hd} ($=\gamma_{LV}/\eta_L$). For small $Ca < 10^{-5}$ capillary forces dominate, while viscous forces dominate for large Ca. For sessile drops characteristic lengths are sessile drop base radius (r_{base}), wedge length (l_W) and for capillary wetting capillary length (L_{cap}). The total wetted area is characte-rized by ($R_{base} = r_{base} + l_W$) which can be related to Weber and Bond numbers. The contribution from gravity (large drops) is small when small when $Bo < 0.5$.

4.3. Line tension

In *mesoscopic wetting* surface heterogeneities μm–nm apart may result in experimentally observable deformation of three-phase contact-line (*tpcl*). For small contact angles the deformation of *tplc* equals the appearance of line tension due to *tpcl* elasticity and pinning. Elasticity aims at keeping *tpcl* undisturbed while pinning induces local radii of curvature (r_{local}). Since surface forces become significant at *tpcl*, the projected drop profile cannot maintain its spherical shape. However, it is

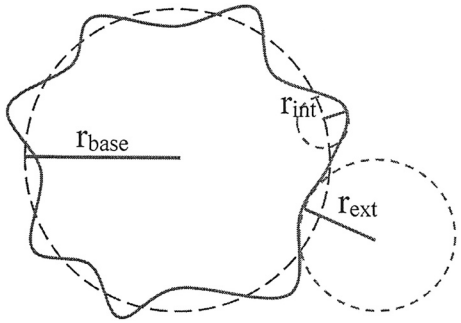

Fig. 8. Relationship between average base radius (r_{base}) and local internal (r_{int}) and external (r_{ext}) radii of the corrugated *tplc*.

still possible to formally maintain the apparent spherical shape of base radius (r_{base}) if the changes at *tpcl* is accounted for by introducing a line tension (τ_{SL}). Line tension is related to the local curvature (r_{local}) of *tplc*. Fig. 8 illustrates the relationship between average base radius (r_{base}) of a liquid stain (sessile drop) and local curvatures at the corrugated *tplc*.

When radii of curvature (r) or curvature ($1/r$) are concave (r_{int}) or bended towards the center of the stain they are considered positive and when curvature is convex (r_{ext}) they are considered negative [4]. At inflection points along *tplc*, the local radius of curvature $r_{infl} = \infty$. It is expected that $\tau_{SL}/\sigma_{SL} \approx 10^{-11}/10^{-2}$ [(J/m)/(J/m^2)] = 1 nm [27]. However, line tensions up to 10^{-5} J/m have been reported [9] corresponding to liquid collars in mm range. A measurable influence on *tplc* is in the nanometer range, while for larger contact angles interfacial tension is dominating. Line tension is defined as an extra contribution to equilibrium Young equation in terms of radii of curvature [10,27,28] as:

$$\tau_{SL} r_{base} + \tau_{SL}\langle r_{local}\rangle = \gamma_{LV}\left(cos\Theta^{Y}_{SL} - cos\Theta^{\tau}_{SL}\right) \tag{59a}$$

or in terms of curvature as:

$$\frac{\tau_{SL}}{r_{base}} + \left\langle \frac{d\tau}{dr_{base}} \right\rangle = \gamma_{LV}\left(cos\Theta^{Y}_{SL} - cos\Theta^{\tau}_{SL}\right) \tag{59b}$$

where $<>$ equals average values and $\cos\Theta^{\tau}_{SL}$ represents the contact angle in presence of line tension. The second left hand term in eq. (59b) characterizes the influence of local radii (r_{local}) at *tplc*. For sufficiently large droplets it can be neglected [27,28]. Radial extensions of 1 nm magnitude cannot be detected by optical means. Scanning force microscopy (SFM, tapping mode) has, however provided experimental means to detect sessile drop contact angles and *tpcl* curvature on nanometer scale [28]. As shown in Table 5, line tensions are in the range $10^{-11} < \tau_{SL}/N < 10^{-10}$. Line tensions determined from contact angle measurements (Eq.(59a) with $<r_{local}>$ neglected) agreed closely to those determined from interfacial potential measurements using scanning force microscopy (SFM). Moreover, interfacial potentials provided information on excess molecular (van der Waals, charge) interactions close to *tpcl*.

Both positive and negative τ_{SL} agree with the qualitatively different *tpcl* interaction. The contact angle approach is based on large scale tension with constant interface energies. Only as a first-order perturbation *tpcl* is included in Eq. (59a) with the basic assumption that *tpcl* region is more or less one-dimensional. The line tension is derived from its effective influence on the macroscopic parameters; the contact angle and *tpcl* curvature. In contrast the interface potential approach is based on detailed structure of *tpcl* region [28]. Direct information about *tpcl* interaction is derived, which is reported as its force contribution.

According to de Gennes [13] the line tension should instead be expressed as:

$$\frac{\tau_{SL}}{r_{base}} = \gamma_L\left(\Theta^{\tau}_{SL} - \Theta^{Y}_{SL}\right) \tag{60}$$

where Θ^{Y}_{SL} = equilibrium Young and Θ^{τ}_{SL} = strained contact angles. The $\tau_{SL}/(r_{base}\gamma_{LV})$ratio should be of the order 10^{-4} for $r_{base} \approx 1$ μm and the molecular distance 0.1 nm $< \tau_{SL}/\gamma_{LV} <$ 1 nm. As discussed, such dimensions are nowadays experimentally accessible. The line tension is, however obscured by a much more dominant fringe elasticity of *tpcl*. Large line tension values were considered as experimental artefacts due to experimental shortcomings. Consi-dering viscous dissipation of liquids, some average distance between adjacent surface sites, $\lambda \propto 1/\sqrt{N^s/A}$ we may define a rigidity constant [13] as:

$$K_{\tau} = \frac{\pi\gamma_L}{ln\left(\lambda/r_{base}\right)} \tag{61}$$

The maximum energy (work) consumed in viscous dissipation of *tplc* can be characterized [13] as:

$$W^{\tau}_{SL} = \frac{\gamma_{LV}}{N^s_{\lambda}}\left(cos\Theta^{Y}_{SL} - cos\Theta^{A}_{SL}\right) \tag{62}$$

where Θ^{A}_{SL}represents advancing contact angle and equilibrium contact angle has been assumed to be $\Theta^{Y}_{SL} = \pi/2$ (in radians). The following conclusions may be drawn: 1) The amplitude of hysteresis is proportional to number of surface sites and 2) The amplitude varies as the square of maximum pinning force which depends on the site wettability, size, and shape.

4.4. Hydrodynamic (HD) model – Complete wetting

Hydrodynamic theory is based on the time dependent balance between viscous drag dissipation within liquid drops resisting movement and on an out-of-balance capillary force (time dependent surface pressure, Eq.(38)) supporting spreading. The viscous spreading of liquids on smooth and completely wetted surfaces (Θ^{t}_{SL}) was generalized by Hoffman [29], Voinov [30] and Tanner [31]. Based on experimental observations they concluded that:

$$\Theta^{t}_{SL} = f_{HVT}(Ca) = f_{HVT}\left(\frac{\eta_L v_L}{\gamma_{LV}}\right) = f_{HVT}\left(\frac{v_L}{v_{hd}}\right) \tag{63}$$

The model assumes that sessile drops maintain their spherical Laplacian shape and that liquid transport velocity can be normalized by the capillary number (Eq.(58)). The rate (velocity) of spreading is thus normalized by the ratio of liquid viscosity and its surface tension. Complete wetting on ideally smooth surfaces can be related to advancing and receding wetting based on *Ca* as:

- For advancing liquids, $Ca^A \geq 0$ a microscopic precursor vapor film is formed ($\Theta^{t}_{SL} = \Theta^{A}_{SL} \rightarrow \Theta^{t+\Delta t}_{S(V)L}$), where Δt represents relaxation time.
- For receding liquids, $Ca^R \leq 0$ a microscopic surface liquid film is formed ($\Theta^{t}_{S(F)L} = \Theta^{R}_{S(F)L} \rightarrow \Theta^{t+\Delta t}_{S(V)L}$), where Δt represents relaxation time.

Table 5
Line tensions (τ_{SL}/N) determined from contact angle measurements (Eq.(59a), $<r_{local}>$ neglected) and by SFM interfacial potential method of probe liquids on hydrophilic (h-phil) silicon wafers [28]. A part of silicon wafers was patterned by hydrophobic (h-phob) perfluorinated alkylsilane.

	Hexaethylene	glycol	Water	$CaCl_2$	electrolyte	
Method	h-phil SiO_2	h-phob SiO_2	h-phil SiO_2	h-phil SiO_2	h-phob SiO_2	Mica
Θ_{SL}	$-1.0{\cdot}10^{-10}$	$-3.0{\cdot}10^{-10}$	$+0.8{\cdot}10^{-10}$	$+1.0{\cdot}10^{-10}$		
SFM	$-1.0{\cdot}10^{-10}$	$-2.0{\cdot}10^{-10}$	$+0.7{\cdot}10^{-10}$	$+1.0{\cdot}10^{-10}$	$+2.0{\cdot}10^{-10}$	$+0.3{\cdot}10^{-10}$

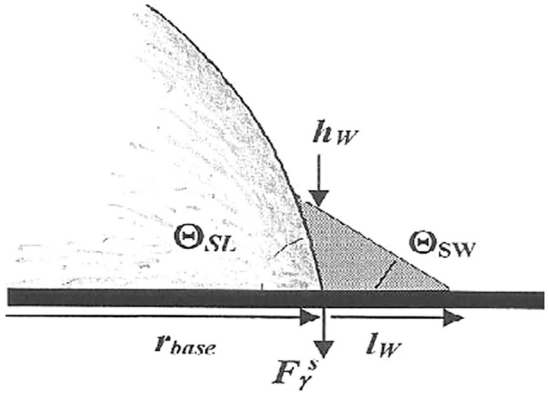

Fig. 9. Close to the three-phase contact-line (*tpcl*) of a sessile drop, the curvature is deformed due to hydrodynamic formation of a liquid wedge. Ahead of the wedge an (adsorbed) molecular vapor film may develop [1,11]. A movement of *tpcl* is resisted by the surface friction force, F_γ^s.

Kept at constant vapor pressure for a prolonged time (sufficient Δt), both advancing and receding contact angle merge as limiting $\Theta^0_{S(X)L}$ ($X = V,F$). Molecular behavior (vapor wedge formation) becomes important when contact angle diminishes. For small Capillary numbers ($Ca < 0.2$), the following relationships applies [11,29–31]:

$$\Theta^t_{SL} = 4.54\ Ca^{0.353} \approx 4.54\ Ca^{1/3} \quad \Rightarrow \quad \left(\Theta^t_{SL}\right)^3 \propto Ca \tag{64}$$

Note that contact angles are expressed in radians. The correlation holds for simple liquids with $35^o < \Theta^t_{SL} = \Theta^A_{SL} < 135^o$. By converting to radial rate of spreading of a liquid on a solid in air Eq. (63) gives:

$$\left(\Theta^t_{SL}\right)^3 \propto Ca \quad \Rightarrow \quad \Theta^t_{SL} \propto \left[\frac{\eta_L}{\gamma_{LV}}\left(\frac{dr_{base}}{dt}\right)\right]^{1/3} \tag{65}$$

4.5. Hydrodynamic model – Partial wetting

The equilibrium profile of a sessile drop resting on an ideally smooth solid substrate is illustrated in Fig. 9.

Note that movement of *tpcl* is resisted by the surface friction force, F_γ^s:

$$F_\gamma^s = -\gamma_{LV} sin\Theta_{SL} \tag{66}$$

The liquid close to the *tpcl* can thus microscopically be divided into two distinct regions: The bulk liquid and the thin vapor wedge. For small Θ_{SW} the work of spreading can be expressed as $S_{SL} \approx -\gamma_{LW}\Theta^2_{SW}/2$ and then eq. (35) can be modified (Fig. 4) to give liquid wedge (*W*) of non-volatile liquid drops as:

$$h_w \approx \sqrt{\left(\frac{H_{SL}}{6\,\pi\gamma_{LV}}\right)\left(\frac{\gamma_{LV}}{2S_{SL}}\right)} = \sqrt{\frac{H_{SL}}{12\,\pi S_{SL}}} \tag{67}$$

where *H* represents Hamaker constant [2,3]. Eq. (67) applies when non-retarded van der Waals interaction forces dominate over capillary interaction.

In absence of contact angle hysteresis and other effects found at small contact angles and small wetting rates (the influence of wedge neglected), eq. (64) can be expanded to apply for partially wetting ($\Theta^o_{SL} > 0$) systems [11,29–31] as:

$$\left(\Theta^t_{SL}\right)^3 = \left(\Theta^o_{SL}\right)^3 + f_{HVT}\,Ca \tag{68a}$$

where contact angles remain undefined. An example of such dependence is illustrated in Fig. 10.

As shown, a low and a high wetting rate section separated by a slip-stick range can be distinguished. The low-rate section extrapolates to a static contact angle $\Theta^o_{SL} = 28^o$, which agrees reasonably well with the experimentally determined non-corrected equilibrium contact angle value $\Theta_{SL}{}^* = 33^o$ (see Table 1). It has been found that small drops spread at a slightly higher rate than large drops. A no-slip condition is applied to the solid-liquid boundary. A slipping of the liquid at the interface is assumed which removes the discontinuity in viscous stress. In vapor, for contact angle less than ($3\pi/4 = 135^o$) Cox and Voinov derived the following equation [31,32]:

$$\left(\Theta^t_{SL}\right)^3 \approx \left(\Theta^0_{SL}\right)^3 \pm 9\ Caln\left(\frac{r_{base}}{l_W}\right) \tag{68b}$$

where base radius, $r_{base} < L_{cap}$ and characteristic wedge length, l_W = slip length of precursor meniscus. The size ratio is one expression for $\sqrt{Bo}$ (Eq.(57b)). Contact angles must be expressed in radians. The positive

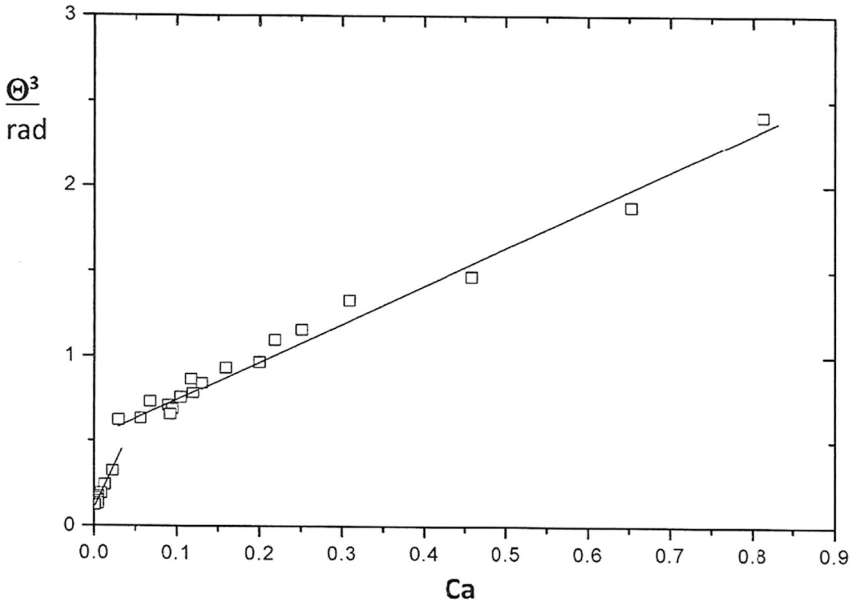

Fig. 10. The cube of contact angle (in radians) for ethylene glycol on OS1 paper (Table 1) plotted against capillary number (normalized wetting rate). The constant slope (s_Θ) and intercept (i_Θ) for the low spreading rate region were $f_{\Theta,1} = 9.1576$ and $i_{\Theta,1} = 0.121$ (28,3°) and the high spreading rate region $f_{\Theta,2} = 2.217$ and $i_{\Theta,2} = 0.539$ (46.6°), respectively [17].

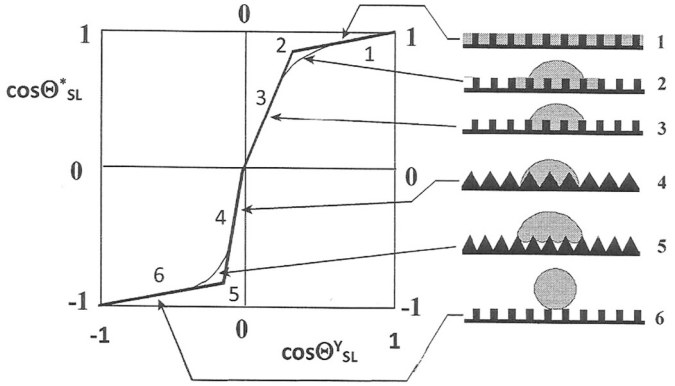

Fig. 11. Relationship between apparent contact angle ($\cos\Theta_{SL}$*) and ideal (Young) contact angle ($\cos\Theta_{SL}^{Y}$) can be schematically divided into four basic ranges (1, 3, 4 and 6) and two transition zones (2 and 5). The influence of the surface structure on wetting is illustrated for each range [11].

sign refers to advancing and negative sign to the receding liquid movement. The hydrodynamic (*HD*) model corresponds to a rate dependent buildup of a fractal object, which is characterized by the ratio of a macroscopic and a nanoscopic characteristic length (perimeter) [11].

Assuming that the limiting time-independent contact angle (Θ_{SL}^{0}) remains constant, eq. (67b) shows that time dependence of contact angle (Θ_{SL}^{t}) on surface chemistry and liquid viscosity corrected spreading velocity (*Ca*) is interpreted as changes in ratio of characteristic macroscopic (millimetric bulk) and microscopic (nanometric wedge) length expressed as:

$$ln\left(\frac{r_{base}}{l_W}\right) = \frac{1}{9}\left(\frac{d\left(\Theta_{SL}^{t}\right)^3}{dCa}\right) \tag{68c}$$

The slip length (l_W) can be obtained from a plot of $(\Theta_{SL}^{t})^3$ against capillary number (velocity). Then $(\Theta_{SL}^{0})^3$ is obtained as the intercept at zero velocity. It is expected that this model applies at least for $Ca \langle 2$. At high wetting rates, hydrodynamics becomes the dominant force, and the geometry of the system will influence the dynamic contact angle. Dynamic drop spreading at $Ca \langle\langle 1$ is free from this obstacle. Although the fit of the hydrodynamic model has been found to be good it may produce unphysical data and must be treated with caution [18,32].

Hayes and Ralston [18] found for the polyethylene terephthalate (PET)–water system an agreement within a few degrees between the contact angle extrapolated to $Ca = 0$ and the equilibrium contact angle determined separately. The agreement pre-assumes that wetting rate was sufficiently small ($v_L < 0.2$ cm/s). They concluded that advancing contact angles should be used since receding contact angles are governed by a different relaxation mechanism. The uncertainty increases with *Ca* due to an extended extrapolation distance.

When apparent Θ_{SL}*data are available Wenzel r_W-ratio can be used to calculate the contact angles corresponding to smooth Young surfaces (Θ_{SL}^{Y}) [11] as:

$$cos\Theta_{SL}^{*} = r_W\, cos\Theta_{SL}^{Y} \quad \Leftrightarrow \quad r_W = \frac{cos\Theta_{SL}^{*}}{cos\Theta_{SL}^{Y}} = \left(\frac{L}{l}\right)^{d_f-2} \tag{69}$$

The Wenzel roughness has been found to be poorly related to the root mean square (rms, S_q) deviations from the mean elevation. Although neglected in most instances, even molecular scale roughness may contribute to the wetting behavior. The range of self-similarity for which fractal dimension characterization applies is determined by the largest (L) and smallest (l) lengths of projected objects and may be related to Wenzel roughness factor r_W in eq. (69) [11]. Since $d_f^{1D} = 1$, $d_f^{2D} = 2$ and $d_f^{3D} = 3$, the range of limiting step lengths for surfaces is obviously $2 < d_f < 3$. Generally, solid structure relates to surface roughness, porosity, and homogeneity (crystal facelets). For the sake of clarity, the focus in Fig. 11 is placed on squared-to-sawtooth profiles. Depending on interaction between probe liquid and solid structure we may distinguish between four basic wetting behaviors [11]:

- The complete wetting (imbition) range (1), where the liquid fully wets the grooves of the rough surface.
- The partial wetting (Wenzel) range (3), where the liquid wets only the asperities under the drop.
- The partial rejection (nanobubble formation) range (4), where the liquid begins to be rejected from the grooves.
- The full rejection (Lotus) range (6), where the liquid wets only the top of the asperities
- and two transition zones (2) and (5).

The Wenzel model (Eq.(68)) applies only to range 3 type of wetting behavior. Two limiting cases can be distinguished considering polar liquids (water) [11]:

1. For hydrophilic solids the wetting and imbition ranges are characterized by ($\Theta_{SL} < 90^{o}$), while $\Theta_{SL}^{*} < \Theta_{SL}$ since $r > 1$
2. For hydrophobic solids the repulsion and Lotus ranges are characterized by ($\Theta_{SL} > 90^{o}$), while $\Theta_{SL}^{*} > \Theta_{SL}$ since $r > 1$

Contact angles and surface energy components of a few selected model papers were deter-mined according to van Oss-Chadhury-Good procedure [6–8] and listed in Tables 6 and 7.

Small equilibrium contact angles give an indication of stronger adsorbate – site interaction (adhesion, wedge formation) than mutual interaction between molecules in liquids (cohesion). This can lead to a slow spreading kinetics. It has been shown that it is easier to spread water on low-energy surfaces than on high-energy solids [16]. In the first case water is finally broken in liquid parts with large contact angle. A slip-stick disturbance may occur already at very small wetting rates ($v_L < 1$ mm/s) which is escalated when time-dependent contact angle

Table 6
Apparent contact angles (Θ_{SL}*) determined for ethylene glycol sessile drops on rough paper surfaces and corresponding limiting equilibrium contact angles ($\Theta_{SL}^{0} = \Theta_{SL}^{Y}$) from eq. (69) at $Ca = 0$ [19,20]. The drop size was 1.0 μl for off-set samples OS1-OS4 and 0.5 μl for ink-jet samples IJ5-IJ8 (Table 1). Surface energy components of papers (mJ/m^2) calculated by vOCG-method [6–8].

Paper	S_q nm	r_W	Θ_{SL} deg	Θ_{SL}^{Y} deg	Θ_{SL}^{low} deg	Θ_{SL}^{high} deg	σ_{SV} mN/m	σ_{SV}^{LW} mN/m	σ_{SV}^{AB} mN/m	σ_{SV}^{A} mN/m	σ_{SV}^{B} mN/m	σ^{B}/σ^{A}
EG							*48.0*	*29.0*	*19.0*	*1.92*	*47.0*	*24.5*
OS1	116	1.43	33	54	28.3	46.6	33.3	30.5	2.78	0.09	21.3	237
OS2	47.3	1.20	32	45	27.4	46.3	36.6	33.7	2.93	0.07	31.5	450
OS3	60.3	1.07			52.2	57.3	37.4	34.6	2.78	0.40	4.80	12.0
OS4	26.4	1.02			42	50	41.3	36.8	4.47	0.35	14.1	40.3
IJ5	51.0		45		45		37.9	37.0	0.90	0.00	30.6	–
IJ6	17.8		62		61		48.0	37.5	10.5	0.80	34.0	42.5
IJ7	4.80		53		52		20.6	18.0	2.60	4.60	0.40	0.09
IJ8	2.06		19		19		42.6	34.3	8.40	3.10	5.70	1.84

Table 7
Apparent contact angles (Θ_{SL}*) determined for water sessile drops on rough paper surfaces and corresponding limiting equilibrium contact angles ($\Theta^0_{SL} = \Theta^Y_{SL}$) from eq. (69) at $Ca = 0$ [19,20]. The drop size was 1.0 μl for off-set samples OS1-OS4 and 0.5 μl for ink-jet samples IJ5-IJ8 (Table 1). Surface energy components of papers (mJ/m^2) calculated by vOCG-method [6–8].

	S_q	r_W	Θ_{SL}	Θ^Y_{SL}	Θ^{low}_{SL}	Θ^{high}_{SL}	σ_{SV}	σ^{LW}_{SV}	σ^{AB}_{SV}	σ^{A}_{SV}	σ^{B}_{SV}	σ^B/σ^A
Paper	nm		deg	deg	deg	deg	mN/m	mN/m	mN/m	mN/m	mN/m	
W							*72.8*	*21.8*	*51.0*	*25.5*	*25.5*	*1.00*
OS1	116	1.43			55.1	66.1	33.3	30.5	2.78	0.09	21.3	237
OS2	47.3	1.20			47.2	52.8	36.6	33.7	2.93	0.07	31.5	450
OS3	60.3	1.07			82.5	94.6	37.4	34.6	2.78	0.40	4.80	12.0
OS4	26.4	1.02			71.8	87.5	41.3	36.8	4.47	0.35	14.1	40.3
IJ5	51.0		62		63		37.9	37.0	0.90	0.00	30.6	–
IJ6	17.8		65		65		48.0	37.5	10.5	0.80	34.0	42.5
IJ7	4.80		105		105		20.6	18.0	2.60	4.60	0.40	0.09
IJ8	2.06		70		72		42.6	34.3	8.40	3.10	5.70	1.84

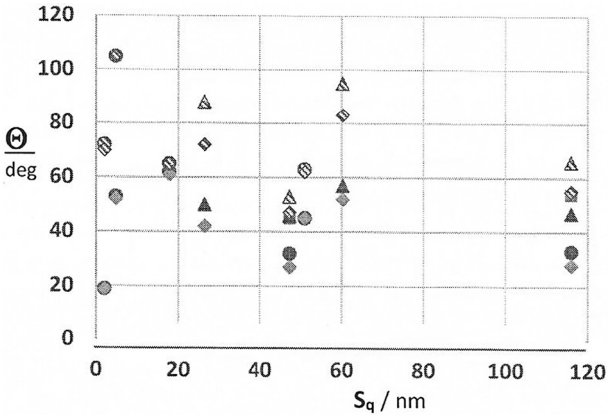

Fig. 12. Apparent (Θ*, circles), equilibrium (Θ^Y, squares), extrapolated short-t (Θ^{low}, diamonds) and long-t (Θ^{high}, triangles) contact angles of ethylene glycol on papers OS1-OS4, IJ5-IJ8 as a function of rms roughness *Sq* (Table 5). The corresponding patterned symbols refer to sessile drops of water (Tables 6 and 7).

grows. Three important observations can be made from Tables 6 and 7:

1) As expected, contact angles extracted from the low-$Ca(v_{tpcl})$ range agree with apparent equilibrium contact angle determined separately for the same substrate.
2) Despite limited number of determinations, a closer examination reveals that the limiting contact angles extracted from the high-Ca (v_{tpcl}) range agree with the Young contact angles corrected with Wenzel's r_W-values (Eq.(46)) listed in Table 1.
3) The transition from low to high-$Ca(v_{tpcl})$ range (break point in Fig. 9) identifies an unstable (chaotic) slip-stick range.

The most basic information on surface chemistry is provided by contact angles. In Fig. 12 contact angles listed in Tables 6 and 7 are plotted as a function of rms roughness S_q.

There seems to be a complex dependence of contact angles on S_q. In Fig. 13 contact angles listed in Tables 6 and 7 are plotted as a function of total and base component of surface energy of off-set papers OS1-OS4 and ink-jet papers IJ5-IJ8.

When contact angles are plotted as a function base component of surface energy (Tables 6 and 7) the complex dependence on (total) surface energy becomes quite systematic. An increased base component result in reduced contact angle for most model papers.

4.6. Summary

Classical work of spreading may be expressed for bare (vapor free), for vapor covered and thin film coated solids.

Vapor in excess of saturation form thin α-films in equilibrium with thick β-films. Between these extremes van der Waals loop characterizes transient metastable states and a unstable range where spinodal decomposition of films result in separation of sessile drops.

The interaction within thin films is expressed as Derjaguin's disjoining pressure which can be divided into linear contributions of solvent structure, of van der Waals and electrostatic interactions, of capillary suction and of gravity. The dependence of disjoining pressure on film thickness provides a mean to establish the film stability.

Work of spreading is defined both as the difference between work of adhesion and work of liquid cohesion, as well as integral linear sum of disjoining pressures. Focusing on vertical solid-film interactions, work

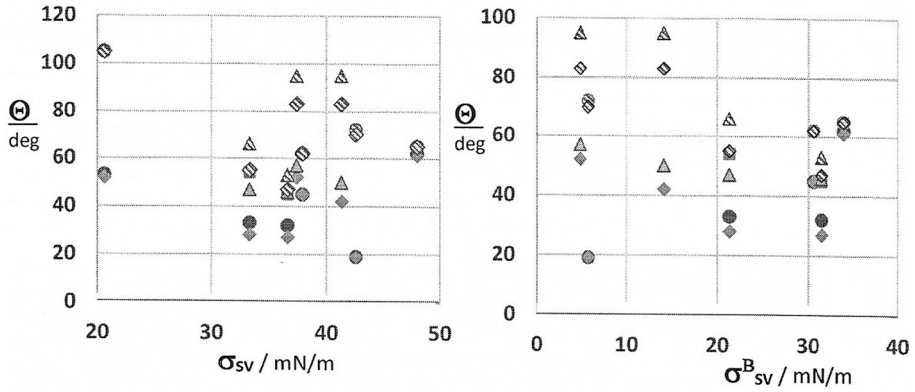

Fig. 13. Apparent (Θ*, circles), equilibrium (Θ^Y, squares), extrapolated short-t (Θ^{low}, diamonds) and long-t (Θ^{high}, triangles) contact angles of ethylene glycol on papers OS1-OS4, IJ5-IJ8 as a function of surface energy (left diagram) and base component (right diagram) (Table 1). The corresponding patterned symbols refer to sessile drops of water.

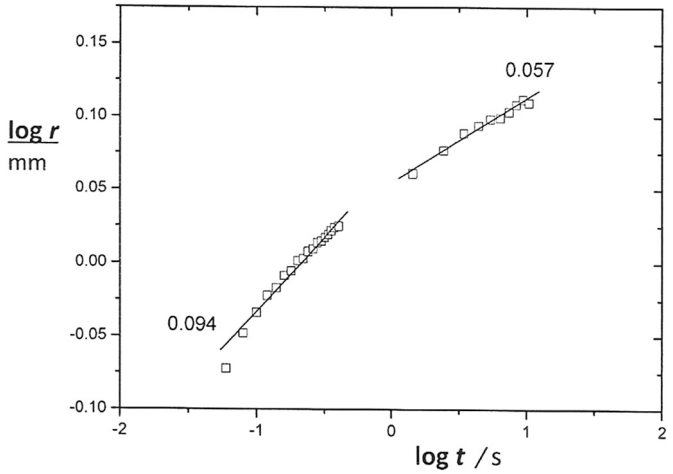

Fig. 14. Logaritmic relationship between drop base radius, r^t_{base} of ethylene glycol on paper OS1 (Table 1) and time. The slopes are $s_r = 0.094$ (1/10) and $s_r = 0.057$ (1/17), respectively [17].

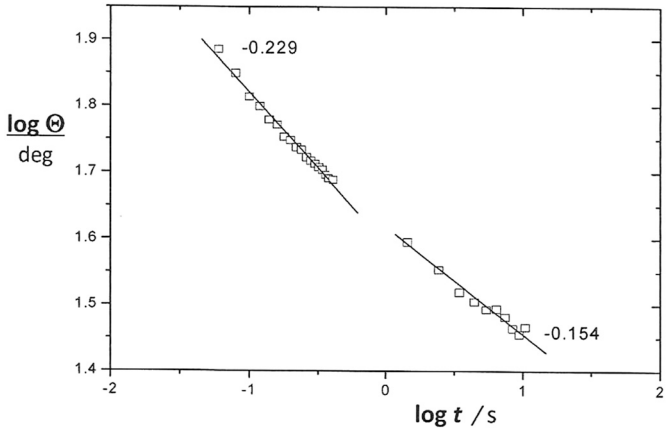

Fig. 15. Logaritmic relationship between the contact angle, Θ^t_{SL} of ethylene glycol on paper OS1 (Table 1) and time. The slopes are $s_{\Theta,1} = -0.229$ (−3/13) and $s_{\Theta,2} = -0.154$ (−3/19), respectively [17].

of adhesion is represented by integral sum of disjoining pressures. The models for geometric averaging and linear combination of dispersive ($D = LW$), polar ($P = AB$), acid (A) and base (B) contributions to all system components become partly contradictory.

Line tension represent thin film movement over heterogeneous solid surfaces. Three-phase contact-line rigidity and fringe elasticity may, however obscure line tension.

Hydrodynamic (*HD*) model was designed to characterize mobility of sessile drops (partial wetting) and liquid films (complete or forced wetting). It is based on relationships between cube of contact angles expressed in radians and Ca. Their derivative is interpreted as ratios of characteristic macroscopic (capillary length) and micro/nanoscopic (wedge) lengths.

Experimentally, two steady-state ranges are identified. The limiting contact angle extrapolated from low-*Ca* range corresponds to apparent contact angle, while the limiting contact angle extrapolated from large-*Ca* range corresponds to equilibrium (Young) contact angle. Wenzel has derived the relationship between these contact angles.

The linear steady-state *Ca*-ranges is intersected by a break range (point) characterizing unstable slip-stick transformation. Corrections for surface roughness (and other surface structure features) should be made before data fits to theoretical models. Wenzel's correction applies only within a restricted contact angle interval.

Contact angles of ethylene glycol and water on model papers were found to depend in a complex way on degree of rms roughness (S_q) and on total surface energy (σ_{SV}). A more organized dependency is found on basic component of surface energy (σ^B_{SV}).

5. Evaluation of MK- and HD models

Molecular-Kinetic (*MK*) model is based on volatile vapor behavior near *tpcl* while hydro-dynamic (*HD*) model is based on viscous liquid behavior. It seems therefore necessary to evaluate their prediction of *tpcl* dependence on surface structure and chemistry using first-hand experimental data.

5.1. Time dependence of base radius and contact angle

Based on eq. (65), de Ruijter et al. [33,34] derived characteristic base radius – time and contact angle – time proportionalities relating to both hydrodynamic (*HD*) and molecular-kinetic (*MK*) behavior. For vanishing contact angles, it was shown for hydrodynamic behavior within long time range that:

$$r^{HD}_{base} \propto t^{1/10} \quad \Leftrightarrow \quad \Theta^{HD}_{SL} \propto t^{-3/10} \tag{70}$$

Logarithmic $\log r^{HD}_{base} - \log t$ and $\log \Theta^{HD}_{SL} - \log t$plots are expected to give a good fit for viscous liquids (ethylene glycol and glycerol) and nearly complete wetting. In Fig. 14 the initial slope $s_r = d \log r/d \log t$ does, indeed agree with the expected exponential (1/10) dependence, which supports the hydrodynamic mechanism. At extended time the exponent decreases to $s_r = 0.057$ (1/17).

Apparent equilibrium contact angles extrapolated from short- t range to zero-t have been found to agree with separately determined equilibrium contact angles which are uncorrected for surface roughness. Contact angles extrapolated from the long- t regime to zero-t corres-pond to a flow over the surface (contact angles) smoothened with Wenzel (Eq. (69)) r_W-values. Overall, $\log r^{HD}_{base} - \log t$ and $\log \Theta^{HD}_{SL} - \log t$plots have been found to apply close to equilibrium or at very long times. The slope

Table 8
Characteristic two-step $s_\Theta = d\log\Theta_{SL}/d\log t$ and $s_r = d\log r_{base}/d\log t$ slopes of 1.0 μl ethylene glycol (columns 5–8) and of 0.5 μl water (columns 9–10) on papers OS1-OS4, IJ5-IJ8 (Table 1). The slope $s_r^2 = d\log r^2_{base}/d\log t$ (last right column 11) [19,20].

	S_q	S_{dr}	r_W	s^{ini}_Θ	s^{ini}_r	s^{fin}_Θ	s^{fin}_r	s_Θ	s_r	s_r^2
Paper	nm	%		m/s	m/s	m/s	m/s	m/s	m/s	m^2/s
HD				*−0.30*	*0.10*	*−0.30*	*0.10*	*−0,30*	*0.10*	*0.20*
MK				*−0.43*	*0.14*	*−0.43*	*0.14*	*−0.43*	*0.14*	*0.29*
OS1	116	43.3	1.43	−0.22	0.096	−0.15	0.055	−0.102	0.063	
OS2	47.3	19.6	1.20	−0.22	0.096	−0.15	0.055	−0.124	0.064	
OS3	60.3	6.70	1.07	−0.068	0.038	−0.042	0.016	−0.052	0.039	
OS4	26.4	2.40	1.02	−0.117	0.054	−0.071	0.026	−0.077	0.049	
IJ5	51.0			−0.369	0.210	−0.038	0.010	−0.078	0.041	0.30
IJ6	17.8					−0.014	0.005	−0.074	0.006	0.23
IJ7	4.8					−0.139	0.059	−0.010	0.011	0.05
IJ8	2.1			−0.695	0.214	−0.101	0.026	−0.017	0.004	0.22

range found for a selection of model papers presented in Table 8 cover the exponent predicted by both models.

Considering molecular kinetic processes in vicinity of the advancing three-phase contact-line (*tpcl*) de Ruiter et.al found the following proportionalities [33,34]:

$$r_{base}^{MK} \propto t^{1/7} \quad \Leftrightarrow \quad \Theta_{SL}^{MK} \propto t^{-3/7} \tag{71}$$

The dissipation is due to friction at *tpcl*. The molecular-kinetic model has been found to be appropriate for partial wetting ($\Theta_{SL}^{t} > 0$) but to be unsuited for describing the final stages of complete wetting near equilibrium. Fig. 15 presents $\log\Theta_{SL}^{HD}$ – log *t*plots for model paper off-set paper OS1.

The initial slope $s_\Theta = d \log \Theta / d \log t$ agrees roughly with the exponent expected for a molecular-kinetic process, but the exponent found at extended time is much smaller. The average slopes found experimentally for the initial (short-*t*) range of all model papers presented in Table 8 correspond to the predicted exponents. A combined model considering both viscous flow in the bulk sessile drop and frictional processes in vicinity of *tpcl* reproduces successfully both scaling laws in appropriate time (wetting rate) ranges. The droplet spreading was found to depend on physicochemical interactions between model solids and probe liquids. The crossover between time (wetting rate) regimes depends on the sessile drop volume, the hydrodynamic velocity (γ_{LV}/η_L) and the contact angle [35]. Obviously, logarithmic plots of base radius–time (Fig. 14) and contact angle–time (Fig. 15) are expected to provide exponents which are characteristic for each time regime.

Wetting has been found to depend on both surface chemistry and surface structure. The roughness of solid surfaces can conveniently be determined by atomic force microscopy (AFM). The most common parameters use for surface roughness characterization are peak-to-valley rms (S_q/nm) roughness and per cent increase of surface area due to roughness (S_{dr}/%). S_{dr} is related to the commonly used Wenzel r_W-factor (Eq.(69)) [36] by:

$$r_W = 1 + \frac{S_{dr}}{100} \tag{72}$$

The experimentally determined S_q, S_{dr}, Wenzel r_W, $s_\Theta = d \log \Theta_{SL}/d \log t$and $s_r = d \log r_{base}/d \log t$slopes are listed in Table 8.

Apel-Paz and Marmur [37] investigated liquid spreading on smooth and rough solid surfaces. He derived an expression for dependence of wetted rough surface area on time. Expressed as logarithmic squared base radius and logarithmic time the relationship becomes:

$$logr_{base}^2 = logk_M + \left(s_r^2\right) logt \quad \Leftrightarrow \quad \frac{dlogr_{base}^2}{dlogt} = \left(s_r^2\right) \tag{73}$$

These slopes for ethylene glycol on IJ5-IJ8 papers are listed in last column of Table 8. The slopes ($0.20 < (s_r^2) < 0.26$) agree with one-dimensional wetting for smooth papers. The slopes for linear logarithmic dependence of base radius on logarithmic time becomes ($0.10 < s_r < 0.13$) which is in the range of expected slope for hydrodynamic ($s_r^{HD} = 0.10$) and molecular kinetic ($s_r^{HD} = 0.14$) liquid flow. The IJ7 paper is, however, quite exceptional. A view on the information embedded in this relationship is provided by the traditional Washburn – d'Arcy equation (discussed later) for liquid flow expressed as:

$$logr_{base}^2 = log\left(\frac{k_V D_V^s \Delta P}{\eta_L}\right) + logt \quad \Leftrightarrow \quad \frac{dlogr_{base}^2}{dlogt} = k_V\left(\frac{D_V \Delta P}{\eta_L}\right) \tag{74}$$

where ΔP = local Laplace pressure, D_V^s=permeability for surface liquid flow and $k_V = 1/4$ for expansion of liquid cakes. Alternatively, the expansion of sessile drops may be considered to depend on surface diffusion expressed by Einstein eq. (33) as:

$$logR_{base}^2 = logk_D D_c^s + logt \quad \Leftrightarrow \quad \frac{dlogr_{base}^2}{dlogt} = 1 \tag{75}$$

where D_c^s=coefficient for surface diffusion (Eq.(33)): $k_D^{1D} = 2$ for one-dimensional, $k_D^{2D} = 4$ for two-dimensional (surface) and $k_D^{3D} = 6$ for three-dimensional (bulk) diffusion. Since the experimentally determined slopes deviate from unity other factors than those considered in Washburn – d'Arcy (Darcy) and Einstein relationships, such as surface structure play a significant role.

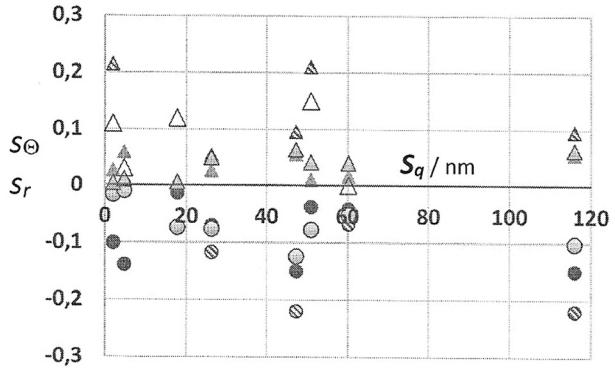

Fig. 16. Dependence of initial (s_Θ^{ini}, patterned circles) and final (s_Θ^{fin}, filled circles) and of initial (s_r^{ini}, patterned triangles) and final (s_r^{fin}, filled triangles) slopes of ethylene glycol on S_q/nm. Dependence of (s_Θ, shaded circles) and (s_r, shaded triangles) slopes of water on S_q/nm. Dependence of (s_r^2 (open triangles) slopes of water on S_q/nm.

Dependencies of base radius on time and contact angle on time on solids for which surface energy components have been determined provide an opportunity to evaluate the influence of surface roughness and surface chemistry. The dependencies of contact angle (s_Θ) and base radius (s_r) slopes (listed in Table 8) on S_q/nm peak-to-peak rms roughness are presented in Fig. 16.

Despite of considerable spread, each set of slopes seem to be dependent on S_q. The best correlations of slopes was found for total and basic surface energies of solid surfaces presented in Fig. 17.

Despite considerable scatter, Fig. 17 suggests that both s_Θ and s_r slopes do correlate with σ_{SL}/(mN/m, left diagram) and with σ_{SL}^B/(mN/m, right diagram). The dependence of s_Θ and s_r slopes on surface energies are reversed. As judged by the much more systematic spread of experimental points it seems that the dominant contribution is provided by basicity of surface sites.

Garnier and coworkers investigated the wetting of hydrophobized paper with water and found time dependent spreading [38,39]. The Bond (Eötvö's) numbers used varied between $1.3{*}10^{-3} < Bo < 2.2{*}10^{-3}$ confirming a negligible effect of gravity on Laplacian sessile droplet. The pseudo-equilibrium contact angle was in the range $70^o < \Theta_{SL} < 120^o$ and the difference between the advancing and receding liquid front of the order $56^o < \Delta\Theta_{S(X)L} < 81^o$. ($X = V$, vapor or $X = F$, thin film). Plotted for capillary numbers in the range $10^{-2} < Ca < 10^{-4}$ the slopes of $\log\Theta_{SL}^t$ versus log *t* plots were of the order of −0.103 for the smoothest and −0.055 for the roughest substrates. This is significantly lower than the slopes predicted by either the hydrodynamic ($s_\Theta^{HD} = -0.30$) or molecular kinetic ($s_\Theta^{MK} = -0.43$) power laws. Garnier suggested that capillary diffusion, surface roughness or chemical heterogeneity may retard wetting by partially pinning the moving *tpcl* as discussed for line tension [38,39]. The average peak-to-valley rms-roughness varied between $5.6 < S_q/\mu m < 6.9$ and the surface asperity were typically higher than 0.16 μm. This roughness was considered sufficient to induce slip-stick disturbance, which reduces wetting rate significantly. This was also supported by the inverse relationship found between wetting rate and roughness for the same surface (hydrophobic paper) chemistry. It was also concluded that the hydrophobic nature could induce cavitation of nanobubbles under the water droplets at the rough surface. Garnier observed, however that surface chemistry had only a negligible effect on the scaling exponents and suggested a structure factor (k_G) correction to the scaling law [39]. The following slopes to hydrodynamic (*HD*) and molecular kinetic (*MK*) exponents were proposed:

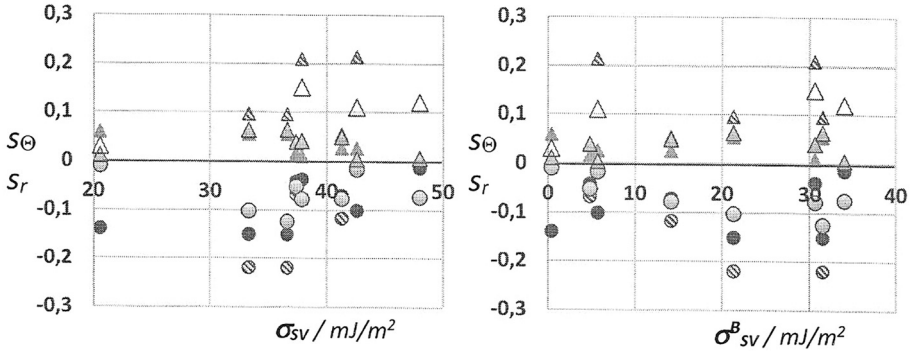

Fig. 17. Dependence of initial (s_Θ^{ini}, patterned circles) and final (s_Θ^{fin}, filled circles) and initial (s_r^{ini}, patterned triangles) and final (s_r^{fin}, filled triangles) slopes of ethylene glycol on σ_{SL}/(mN/m) (left diagram) and on σ^B_{SL}/(mN/m) (right diagram). Dependence of s_Θ (shaded circles) and s_r (shaded triangles) slopes of water on σ_{SL}/(mN/m) (left diagram) and on σ^B_{SL}/(mN/m) (right diagram). Dependence of s_r^2 (open triangles) slopes of water on σ_{SL}/(mN/m) (left diagram) and on σ^B_{SL}/(mN/m) (right diagram).

Table 9
Characteristic correction factors to the molecular kinetic and hydrodynamic models of 1.0 μl ethylene glycol on papers OS1-OS4 and of 0.5 μl ethylene glycol on papers IJ5-IJ8 [19,20] (Table 1). Initial values in left four columns and final values in right four columns. Slopes from Table 8.

Paper	k_Θ^{MK}	k_Θ^{HD}	k_r^{MK}	k_r^{HD}	k_Θ^{MK}	k_Θ^{HD}	k_r^{MK}	k_r^{HD}
OS1	0.201	0.080	0.049	0.004	0.279	0.150	0.088	0.045
OS2	0.201	0.080	0.049	0.004	0.279	0.150	0.088	0.045
OS3	0.361	0.232	0.105	0.062	0.387	0.258	0.127	0.084
OS4	0.312	0.183	0.089	0.046	0.358	0.229	0.117	0.074
IJ5	0.060	−0.069	−0.067	−0.110	0.391	0.262	0.113	0.090
IJ6					0.415	0.286	0.138	0.095
IJ7					0.290	0.161	0.084	0.041
IJ8	−0.265	−0.395	−0.071	−0.114	0.328	0.199	0.117	0.074

$$\Theta_{SL} \propto t^{k_G^{HD}-3/10} \tag{76a}$$

$$\Theta_{SL} \propto t^{k_G^{MK}-3/7} \tag{76b}$$

For water on hydrophobized paper Garnier [38,39] reported a correction constant $0.197 \langle k_G^{HD} \langle 0.245$ for the hydrodynamic model and $0.326 \langle k_G^{MK} \langle 0.374$ for the molecular-kinetic model. In a recent investigation on poly(3-hexylthiophene) semiconductor ink (0.5 wt% P3HT in o-dichlorobenzene) on top-coated paper Peltonen et al. [40] found that the slope of $\log r_{base}^t$ – $\log t$ plots varied from 0.10 on smooth Mica over 0.06 on Kaolin compacts to 0.04 on polycarbonate compacts. The slopes result in $0.04 \langle k_P^{MK} \langle 0.08$ for the molecular-kinetic model and $0.00 \langle k_P^{HD} \langle 0.04$ for the hydrodynamic model. The reduced wetting rate was attributed to surface roughness and porosity, retarding wetting by partially pinning the mowing *tpcl* as found for line tension. Partial pinning was assumed to induce non-equilibrium stick and jump movements typical for the kinetic molecular process. Surface asperities exceeding 0.16 μm were considered sufficient to slow down the wetting rate significantly. Assuming that the Garnier model is applicable both to the drop base radii and contact angles we can establish the following dependencies for the investigated paper samples [11,17,19,20]:

$$\begin{aligned} \Theta_{SL}^t \propto t^{k_\Theta^{MK}-3/7} &\Leftrightarrow \quad s_\Theta^{MK} = k_\Theta^{MK} - 3/7 \;\Leftrightarrow\; k_\Theta^{MK} = s_\Theta^{MK} + 3/7 \\ \Theta_{SL}^t \propto t^{k_\Theta^{HD}-3/10} &\Leftrightarrow \quad s_\Theta^{HD} = k_\Theta^{HD} - 3/10 \;\Leftrightarrow\; k_\Theta^{HD} = s_\Theta^{HD} + 3/10 \end{aligned} \tag{77a}$$

$$\begin{aligned} r_{base}^t \propto t^{1/7-k_r^{MK}} &\Leftrightarrow \quad s_r^{MK} 1/7 - k_r^{MK} \;\Leftrightarrow\; k_r^{MK} = 1/7 - s_r^{MK} \\ r_{base}^t \propto t^{1/10-k_r^{HD}} &\Leftrightarrow \quad s_r^{HD} = 1/10 - k_r^{HD} \;\Leftrightarrow\; k_r^{HD} = 1/10 - s_r^{HD} \end{aligned} \tag{77b}$$

With reference to slopes listed in Table 8 the average correction factors for the investigated ethylene glycol and water on off-set papers OS1-OS4 and ink-jet papers IJ5-IJ8 [19,20] are collected in Tables 9 and 10.

The smaller correction factors are, the closer is the fit to predicted molecular kinetic or hydrodynamic behavior. Relationships to surface structure and surface chemistry should, however only be evaluated after correction of contact angles for surface roughness (Eq.(69)). As shown

Table 10
Characteristic correction factors to the molecular kinetic and hydrodynamic models of 1 μl water on papers OS1-OS4 and 0.5 μl water on papers IJ5-IJ8 [19,20]. Slopes from Table 8.

Paper	k_Θ^{MK}	k_Θ^{HD}	k_r^{MK}	k_r^{HD}
OS1	0.327	0.198	0.080	0.037
OS2	0.305	0.176	0.079	0.036
OS3	0.377	0.248	0.104	0.061
OS4	0.352	0.223	0.094	0.051
IJ5	0.351	0.222	0.102	0.059
IJ6	0.355	0.226	0.137	0.094
IJ7	0.419	0.290	0.132	0.089
IJ8	0.412	0.283	0.139	0.096

the corresponding correction factors are relatively independent on the nature of the substrate paper and on the properties of ethylene glycol. Correction factors representing molecular kinetic (*MK*) model are slightly larger than those of hydrodynamic (*HD*) model. Moreover, the correction factors representing $s_\Theta$slopes (Table 8) are systematically larger than those for s_r slopes. The correction factors for contact angles of water derived from Garnier's data fall within the ranges for both the molecular-kinetic and hydrodynamic models listed in Table 10.

Unfortunately, the large slopes of water were too uncertain to allow a systematic analysis of the correction factors. This is unfortunate, since it would have been interesting to investigate the relationship between the apparent equilibrium contact angles extrapolated from short-*t* dependencies on the one hand and the Wenzel corrected equilibrium contact angles extrapolated from long-*t* dependencies on the other hand. It seems that the slip-stick process causes sufficient instability to provide non-representative slopes and correction factors extrapolated from long-*t* range. This is probably due to the relatively low maximum rate observed for spontaneous sessile drop spreading.

Two constant wetting ranges were also observed or water spreading on ideal PET surfaces with a rms roughness of $S_q = 20$ nm [18], which is in the same range as for investigated paper samples (Table 8). The observed contact angles were, however not corrected for the surface roughness and thence the limiting contact angle from the low v_{tpcl}-range

Table 11
Basic molecular properties of water (W), methanol (MeOH), ethanol (EtOH), 1-butanol (BuOH), 1-octanol (OcOH), formamide (FoAm), ethylene glycol (EG'l) and glycol (glycerine, G'ol). Molar mass (M_L/(g/mol), density (ρ_L/(kg/m^3), dynamic viscosity (η_L/(mPas), Hamaker constant (H_{LL}/(zJ), zJ = 10^{-21} J) and surface tension (γ_{LV}/(mN/m). Additionally, London (Lifshitz)-van der Waals (*LW*), acid-base (*AB*, polar, *H*-bond), acid (*A*) and base (*B*) surface tension components are listed [1–3,8,22,41]. * = estimated value.

Liquid	M_L	ρ_L	η_L	H_{LL}	γ_{LV}	γ_{LV}^{LW}	γ_{LV}^{AB}	γ_{LV}^{A}	γ_{LV}^{B}
	g/mol	kg/m^3	mPas	zJ	mN/m	mN/m	mN/m	mN/m	mN/m
H_2O	18.015	998	0.997	37.3	72.8	21.8	51.0	25.5	25.5
C_1OH	32.04	791	0.564	35.0	22.2	18.2	4.3	0.06	77.0
C_2OH	46.07	789	1.13	42.4	22.1	18.8	2.6	0.02	68.0
1-C_4OH	74.12	810	2.75	49.6	25.0				
1-C_8OH	130.2	827	7.61	56.5*	27.2				
$HCONH_2$	45.04	1113	2.88	60.9	58.2	39.0	19.0	2.28	39.6
$H_4C_2(OH)_2$	62.07	1109	19.67	79.4	48.2	29.0	19.0	1.92	47.0
$H_5C_3(OH)_3$	92.09	1263	731.8	67.1	65.2	34.0	30.0	3.92	57.4

was compared to the uncorrected apparent contact angle Θ_{SL}*. The PET surface also contained low density random blemishes (< 10 mm^2) [18]. These chemical heterogeneities may also have contributed to the observed dynamic wetting behavior. The corresponding ranges found for ink-jet ink radius on various substrates derived from Peltonen's data [40] are also within the range found for the model papers.

5.2. Summary

It is shown that proper experimental conditions (given by L_{cap}, *Bo* and r_W-corrected Θ_{SL}*) are required for a full understanding of the limits of claims made. Moreover, only sufficiently large sets of results enable a full characterization of the systems and the development of predictive models.

Based on cube of contact angle dependence on *Ca*, characteristic dependencies of both base radius and contact angles on time were established, which correspond to both molecular-kinetic (*MK*) and hydrodynamic (*HD*) wetting.

Wetting of model papers and PET surfaces by ethylene glycol or water and wetting of mica sheets and kaolin compacts by ink-jet inks showed, however that the suggested exponents require system dependent correction factors which may be related to influence of surface roughness and/or surface chemistry.

The s_Θ and s_r slopes depend on rms roughness (S_q) and on surface energy (σ_{SV}). The dependence of slopes is considerably improved when plotted against base component of surface energy (σ_{SV}^B, Eq.(16b)). This shows that the influence of both surface structure and surface chemistry on wetting are important.

The $d \log A_S/d \log t$ or $d \log r_{base}^2/d \log t$ slopes should, according to Washburn–d'Arcy and Einstein diffusion models be unity. Since experimental results do not conform to this expectations, surface permeability (related to surface roughness) and surface diffusion cannot alone explain the observed dynamic surface wetting.

6. Forced one-dimensional complete wetting

Contrary to spontaneous two-dimensional wetting of sessile drops, most investigations of solid-liquid wetting mechanisms are executed using forced one-dimensional wetting. Then, different dimensionless force ratios are available to evaluate whether selected experimental conditions prevail. Dimensionless Reynolds number is a measure of relative importance of liquid momentum force as compared to viscous shear force:

$$Re = \frac{\rho_L l v_L}{\eta_L} \tag{78a}$$

Its value depends on the design (dimensions) of the system and is mostly used to establish whether liquid flow is laminar, but not turbulent. Dimensionless Weber number expresses the ratio of liquid drag force to its cohesion force:

$$We = \frac{\rho_L v_L^2 l}{\gamma_{LV}} \tag{78b}$$

Again, its actual value is dependent on the design (dimensions) of the system. For sessile drops characteristic lengths are sessile drop base radius (r_{base}), wedge length (l_W) and for capillary wetting capillary length (L_{cap}). The total wetted area is characterized by ($R_{base} = r_{base} + l_W$) which can be related to Weber and Bond numbers. Generally, the contribution from inertia (large drops) is small when $We < 1.6 \cdot 10^{-5}$ and the contribution from gravity (drop flattening) is small when $Bo < 0.5$.

The most common experimental procedure is dipping of thin (Wilhelmy) plates into probe liquids, but recently other solid substrate shapes (thin fibers) are used. The substrate profile influences the macroscopic contact angle ($\Theta_{S(X)L}^t = \Theta_M^t$), but it is assumed not to change the microscopic contact angle of liquid wedge (Θ_m^0). We shall evaluate some results from such studies. To evaluate the results some basic properties of several probe liquids are listed in Table 11. In particular, the influence of surface chemistry is characterized by listing known molecular surface tension contributions [2,3].

Additional derived properties of probe liquids listed in Table 11 are

Table 12
Molecular volume (v_L), molecular diameter (d_L), molecular spacing (hydrocarbons, l_{LL}^D and semi-polar liquids, l_{LL}^{LW}), hydrodynamic velocity ($v_L = \gamma_{LV}/\eta_L$), capillary length (L_{cap}, Eq.(57a)) and characteristic length (l_{cap}) [2,3,22,41]. * = estimated value.

Liquid	Abrev'n	v_L	d_L	l_{LL}^D	l_{LL}^{LW}	γ_{LV}/η_L	L_{cap}	l_{cap}
		nm^3	nm	nm	nm	m/s	mm	nm
H_2O	W	0.030	0.385	0.15	0.40	73.2	2.73	16.8
C_1OH	MeOH	0.068	0.505	0.16	0.43	39.4	1.69	10.4
C_2OH	EtOH	0.097	0.570	0.17	0.46	19.6	1.69	10.4
1-C_4OH	BuOH	0.152	0.662	0.18*	0.47*	9.09	1.77	10.9
1-C_8OH	OcOH	0.262	0.793	0.18*	0.48*	3.57	1.83	11.3
$HCONH_2$	FoAm	0.067	0.504	0.14	0.39	20.2	2.31	14.2
$H_4C_2(OH)_2$	EG'l	0.093	0.562	0.09	0.51	2.45	2.11	12.9
$H_5C_3(OH)_3$	G'ol	0.121	0.614	0.16	0.43	0.089	2.29	14.1

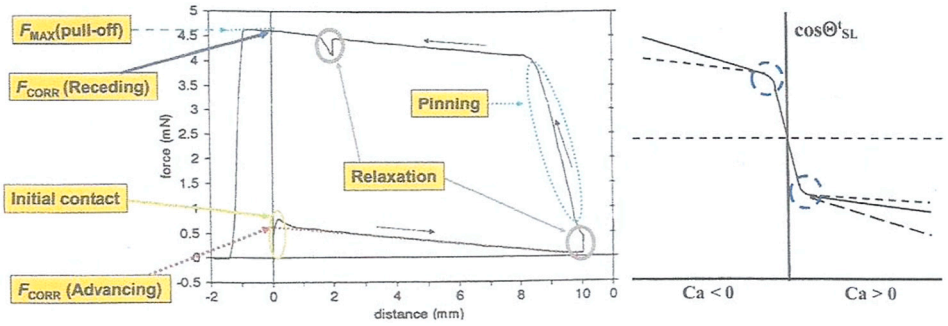

Fig. 18. Left diagram: Force – distance plot for dipping of solid substrate (fiber, plate) into probe liquid (advancing contact) and subsequent withdrawal of the substate (receding contact). Note meniscus relaxation profiles at temporary standstill ($Ca = 0$). Right diagram: Schematic dynamic contact angle – normalized (Ca) rate dependence expressed as advancing ($Ca > 0$) and receding ($Ca < 0$) branches from equilibrium ($Ca = 0$) point: Full drawn lines = experimental, dotted lines = model (Eq.(80)) and dashed line = symmetric ($Ca > 0$). Unstable slip-stick region indicated by broken circle.

given in Table 12: Molar volume $v_L = M_L/(\rho_L N_A)$, molecular diameter $d_L = 2\sqrt[3]{3v_L/4\pi}$, molecular spacing (hydrocarbons) $l^D_{LL} = \sqrt{H^D_{LL}/24\pi\gamma^D_{LV}}$, molecular spacing (semi-polar) $l^{LW}_{LL} = \sqrt{1.2H^D_{LL}/4\pi\gamma^{LW}_{LV}}$ and characteristic length $\ln l_{cap} = \ln L_{cap} - 12$.

Calculated molecular distances in liquid hydrocarbons (l^D_{LL}) are derived by equating work of cohesion (Eq.(10a)) with Hamaker attraction energy between two liquid blocks (H_{LL}) [2,3]. Allowing for graininess at small separations of semi-polar liquids the equilibrium distance (l^{LW}_{LL}) becomes slightly larger. If unknown, a cut-off value of 0.165 nm is frequently used [23]. They equal or are slightly smaller than molecular equilibrium distances between liquids and solids. As shown, the intermolecular distances are nearly equal to the diameter of spherical liquid molecules. A reference characteristic microscopic length l_S may be calculated using the suggested physically acceptable $\ln(L_M/l_S) = 12$ and $L_M = L_{cap}$. However, the obtained l_{cap} is about a decade larger than corresponding molecular dimension (d_L) and equilibrium molecular distances (l_{LL}).

In sessile drop spreading of molten alkyl ketene dimer wax at 65 °C (ρ_L = 860 kg/m^3, η_L = 2.36 mPas, γ_{LV} = 28.8 mN/m) it was found [38,39] that: $6.2{*}10^{-6} < Ca < 1.2{*}10^{-4}$, $2.8{*}10^{-10} < We < 1.0{*}10^{-7}$, $Bo = 8.31{*}10^{-4}$. Since $We << Ca$, Bo inertial forces was neglected. Since $Bo << 1$ the influence of gravity on sessile drop shape was neglected.

6.1. Improved molecular kinetic (MK) models

As discussed, the Molecular-Kinetic (*MK*) model excludes viscous dissipation but is expected to account for surface characteristics (roughness, chemistry). Energy dissipation occurs only at the moving *tpcl* caused by molecular adsorption (advancing, *A*) and desorption (receding, *R*) process. The forward movement is driven by a mean capillary energy (Eq.(38)) defined [41,42] as:

$$\frac{W^s_{cap}}{2N^s_\lambda} = \lambda^2\gamma_{LV}\left(cos\Theta^0_{S(X)L} - cos\Theta^t_{S(X)L}\right) = \frac{\pi^t_{S(X)}}{2N^s_\lambda} \tag{79}$$

where lower index $X = V$ for advancing (wetting) and $X = F$ for receding (dewetting) proess. Introducing eq. (38) into eq. (37) we recover the *MK* model for advancing vapor transport at *tpcl* [16,21,22,41,42] as:

$$cos\Theta^A_{S(V)L} = cos\Theta^0_m - \frac{2N^s_\lambda kT}{\gamma_{LV}} arcsinh\left(\frac{v_{tpcl}}{2\kappa^0_{tpcl}\lambda^{MK}}\right) \tag{80}$$

where κ and λ = fitting parameters. Typically, the average distance of molecular displace-ments is $\lambda \approx$ 1nm and the adsorption/ desorption rates are $\kappa \approx 10^6$s. The positive sign represents advancing and negative sign receding process. Fig. 18 illustrates the time-dependent contact angle as a function of capillary number (Ca).

The experimental conditions were chosen as: $Ca < 5.5{\cdot}10^{-3}$ and $Bo < 2.2{\cdot}10^{-2}$ [41]. Kept at sufficient vapor pressure for a prolonged time (Δt large, constant Ca) both advancing and receding contact angle are expected to merge.

An improved *MK* model was designed to accommodate the unstable slip-stick transition *Ca*-range (dotted circles in Fig. 18) into the overall steady-state *MK* model. The quasi-equilibrium (steady-state) rate constant κ^0_{tpcl}, which was previously related to the activation energy (Eq. (43)) was specified [41] as:

$$\kappa^0_{tpcl} = \frac{kT}{h}e^{-\left\{\left[\left(E^\#/N^s_\lambda\right) - \left(\pi^t_{S(X)}/2N^s_\lambda\right)\right]/kT\right\}} = \frac{kT}{h}e^{-\left\{\left[e^\# - \left(W^s_{cap}\lambda^2/2\right)\right]/kT\right\}} \tag{81}$$

The activation energy (Joule) may be expressed as the sum of a surface and a viscous component [41] as:

$$e^\# = \frac{E^\#}{N^s_\lambda} = kTln\left(\frac{\kappa^0_{tpcl}h}{kT}\right) = e^s + e^\eta = kTln\left(\frac{kT}{\eta_L v_L}\right) + kTln\left(\frac{\eta_L v_L}{h}\right) \tag{82}$$

where v_L = molecular volume of simple liquids. We may now relate rate constant $\kappa^0_{tpcl}$to the surface components κ^s_{tpcl} [16] as:

$$\kappa^0_{tpcl} = \frac{kT}{h}e^{-(E^\#/kT)} = \kappa^s_B\kappa^\eta_B = \left(\frac{\eta_L v_L}{h}\right)\left(\frac{kT}{\eta_L v_L}\right) \tag{83}$$

Blake assumed that λ at *tpcl* and in bulk liquid are the same and replaced κ^0_{tpcl} in eq. (80) by κ^s_B [16] to give:

Table 13
Molecular diameter (d_L/nm), apparent (Θ^*_m) or limiting advancing (Θ^o_m) contact angles, molecular displacement frequency (κ) and corresponding surface site distances (λ). For water, formamide, ethylene glycol and glycerol (glycerin) fits are made to advancing liquid front (Eq.(80)). For alcohols, lower index B represents Blake's model (λ^A_B and κ^A_B, Eq.(84)) [22,41].

Liquid	Θ^*_m	κ^A	λ^A	d_L	Θ^0_m	κ^A	λ^A	κ^{sA}_B	λ^A_B
	deg	s^{-1}	nm	nm	deg	s^{-1}	nm	s^{-1}	nm
H_2O	54.1	$1.19{*}10^4$	1.0	0.385					
C_1OH				0.50	66.2	$1.9{*}10^3$	4.8	$1.1{*}10^5$	4.8
C_2OH				0.57	66.1	$9.9{*}10^1$	5.9	$1.6{*}10^4$	5.9
C_4OH				0.66	63.6	$3.8{*}10^2$	4.4	$2.4{*}10^5$	4.4
C_8OH				0.79	69.2	$1.0{*}10^2$	4.2	$3.0{*}10^5$	4.2
$HCONH_2$	30.5	$5.53{*}10^4$	1.1	0.50					
$H_4C_2(OH)_2$	33.5	$1.97{*}10^3$	1.5	0.56					
$H_5C_3(OH)_3$	46.0	$3.13{*}10^3$	0.9	0.61					

Table 14
Limiting, static advancing, static receding, and effective contact angles (deg) for alcohols on AF 1600 coated silica fibers. Contact angle hysteresis (deg) and Gibbs energy of hysteresis (J/mol) [41].

Alcohol	Θ^0 deg	Θ^A deg	Θ^R deg	Θ^{eff} deg	$\Delta\Theta$ deg	$F\gamma^A$ mN/m	$F\gamma^R$ mN/m	$\Delta_{hys}G^0_m$ J/mol
C_1OH	66.2	68.9	66.0	67.4	2.9	−20.7	−20.3	52.1
C_2OH	66.1	62.8	59.7	61.3	3.1	−19.7	−19.1	73.6
$1{\cdot}C_4OH$	63.6	68.3	63.8	66.1	4.5	−23.2	−22.4	86.5
$1{\cdot}C_8OH$	69.2	74.4	67.1	70.8	7.3	−26.2	−25.1	110

$$cos\Theta^A_{S(V)L} = cos\Theta^0_m \mp \frac{2N^s_\lambda kT}{\gamma_{LV}} arcsinh\left(\frac{\eta_L \nu_L \upsilon_{tpcl}}{2\kappa^s_B \lambda^A_B h}\right) \quad (84)$$

A quasi-static meniscus profile is postulated which neglects viscous bending of the liquid interface. The symmetry of $Ca^A > 0$ and $Ca^R <$ 0serves as qualitative check for these *MK* models. Fits of *MK* models to experimental results are presented in Table 13.

It is found that rate constants are many orders of magnitude smaller than the average molecular displacement rate (10^6 s^{-1}), rate constant for free diffusion (10^9 s^{-1}) and rate constant for viscous flow of simple liquids (10^{11} s^{-1}) [22,41]. Two-dimensional molecular surface displacement occurs at a slower rate than the bulk process. For water on silica surface for water ($\lambda = 1$ nm) $\kappa^{3D} = 4.6{\cdot}10^9$ s^{-1}, while for free water ($\lambda = 1$ nm) $\kappa^{2D} = 2.4{\cdot}10^9$ s^{-1} and for localized water ($\lambda = 0.3$ nm) $\kappa^{2D} = 4.4{\cdot}10^9$ s^{-1} [12]. As illustrated in Fig. 18 the symmetric slopes of $\cos\Theta^t$ – *Ca* predicted by eq. (80) are nearly realized by some, but not by all liquids. To account for the asymmetry Blake exchanged κ^0 for κ^s ($=\eta_L\nu_L/h$) into the arcsinh expression (84). However, as shown in Table 13 the extracted site distances exceed, especially for alcohols molecular dimensions (molecule diameters, d_L) by nearly one order of magnitude. The rate constant for alcohols, which are corrected for viscous dissipation at *tpcl* agree with uncorrected values for other liquids but are two orders of magnitude smaller than the expected range (10^6 s^{-1}). The choice of limiting contact angles have been found to have a decisive impact on the results. Therefore, the effective contact angle obtained from the average advancing and receding contact angles (Eq.(85)) was suggested to be used instead [41]:

$$cos\Theta^{eff}_m = \frac{cos\Theta^A_{max} + cos\Theta^R_{min}}{2} \quad (85)$$

Static advancing (wetting) and receding (dewetting) contact angles were determined 1 min after stopping the dipping or withdrawal of glass fibers into alcohol. The static hysteresis ($\Delta\Theta_{SL} = \Theta^A_{SL} - \Theta^R_{SL}$) that characterizes chemical heterogeneity of the solid surface was found to be small. The effective contact angle (Θ^{eff}_m) is determined from average (extrapolated) maximum advancing and minimum receding static contact angles. This approach differs from the use of dynamic contact angles recorded at small velocities or extrapolated to zero velocity. Then, the advancing contact angle is more appropriate because receding angle could be affected by liquid sorption. Contact angles for silica – alcohol contacts are listed in Table 14.

Extrand derived a thermodynamic model for Gibbs molar energy of hysteresis on smooth and relatively homogeneous surfaces [43] as:

$$\Delta_{hys}G^\theta_m = -RTln\left(\frac{sin\Theta^R_m}{sin\Theta^A_m}\right) = -RTln\left(\frac{F^R_\gamma}{F^A_\gamma}\right) \quad (86)$$

It corresponds to the ratio of surface friction forces (Eq.(66)) at receding and advancing *tpcl*. The molar Gibbs energies (J/mol) are listed in Table 14. Extrand found that hysteriesis is primarily induced by the chemical nature of the system and the resulting intermolecular physicochemical (van der Waals, Lewis's acid-base) interactions involved. This seems like an overstatement in view of the dramatic dependence of solid surface structure (roughness) on wetting behavior (Fig. 18) which, however was not corrected for. Moreover, time-dependent effects such as adsorption-desorption, diffusion and insufficient mobility at the molecular level may contribute to hysteresis. Unfortunately, the surface chemical nature of alcohols is relatively similar (Table 10) which restrict their use alone in rigorous evaluations of equations.

Since rate constants represent transport of matter, we may define a first-order kinetic equilibrium constant and molar pseudo-equilibrium molar Gibbs´ energy as:

$$\Delta_{kin}G^\theta_m = -RTlnK_{kin} = -RTln\left(\frac{\kappa^A_{tpcl}}{\kappa^R_{tpcl}}\right) \quad (87)$$

Unfortunately, no separate rate constants for advancing (wetting) and receding (dewetting) processes are experimentally available.

6.2. Improved hydrodynamic (HD) models

Cox and Voinov redefined Eq. (68b) [22,31,32,41] as:

$$\left(\Theta^t_{S(X)L}\right)^3 \approx \left(\Theta^t_M\right)^3 = \left(\Theta^0_m\right)^3 \pm 9\ Caln\left(\frac{L_M}{l_S}\right) \quad (88)$$

where M = macroscopic and m = microscopic (or molecular) characteristic lengths. Contact angles must be expressed in radians. The plus sign ($Ca^A > 0$) represents advancing and minus sign ($Ca^R < 0$) receding liquid. The macroscopic length L_M represents the dimension of liquid flow (outer region) and relates to Θ^t_M. The slip length (l_S) represents the corresponding size of liquid wedge (inner region) and relates to microscopic contact angle (Θ^0_m). As mentioned *HD* model corresponds to a wetting rate dependent buildup of a fractal object (Eq.(69)) [10]. A typical forced wetting experiment is illustrated in Fig. 19.

In order to ensure proper experimental conditions (negligible influence of gravity and viscosity) the dimensionless Bond (*Bo*, Eq.(57b)), capillary number (*Ca*, Eq.(58)) and Reynolds (*Re*, Eq.(78)) numbers should be acceptable. Cosinus contact angle is related to force exerted by liquid on solid (F_{SL}), to buoyancy force (F_{bu}) and to length of substrate perimeter (solid-liquid contact length, L_{SL}) as, $\cos\Theta^t_{SL} = = (F^t_{SL} - F_{bu})/$

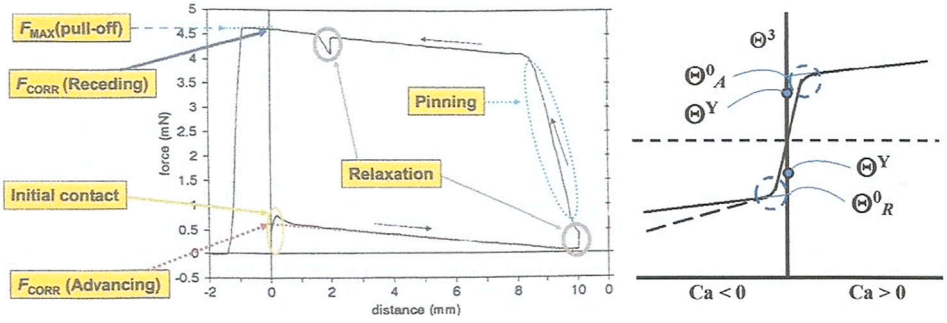

Fig. 19. Schematic illustration of a forced wetting where the solid substrate (fiber, rod, Wilhelmy plate) is dipped into a probe solution to a distance 10 mm at variable wetting rate expressed as capillary numbers. The advancing and receding branches are identified with arrows. Note *tpcl* pinning when movement is reversed and relaxation when movement is arrested. The right-side diagram illustrates the dependence of third-order contact angle on wetting (*Ca*) rate. Extrapolated and equilibrium (Young) advancing and receding contact angles are indicated. Dashed line illustrate typical deviation of model fit to experimental data (full drawn line). Unstable slip-stick region indicated by broken circle.

Table 15
Microscopic (l_S. slip) lengths of advancing and receding liquids extracted from hydro-dynamic (*MD*) model fits and macroscopic (L_M) calculated with eq. (89). Voinov (k_V, Eq.(90)), Zhou-Sheng (k_Z, Eq.(91)) and Blake (k_B, λ_B, Eq.(94) constants extracted from model fits [41].

	L_M^A	l_S^A	L_M^R	l_S^R	k_V^A	k_V^R	k_Z^A	k_Z^R	k_B^A	k_B^R	λ_B^A	λ_B^R
Liquid	mm	m	mm	m							nm	nm
C_1OH	0.24	2.3×10^{-20}	0.26	5.3×10^{-21}						1.94		1.3
C_2OH	0.26	8.6×10^{-16}	0.25	2.1×10^{-17}					0.18	1.49	0.044	2.8
$1\text{-}C_4OH$	0.27	5.8×10^{-11}	0.27	2.6×10^{-12}	2.7^1	6.0^2	2.0^{-1}	4.9	0.23	0.49	0.37	1.7
$1\text{-}C_8OH$	0.26	1.3×10^{-9}	0.26	2.3×10^{-12}	1.2	4.9^3	1.5^{-2}	6.7^1	0.67	0.28	22	0.38

$L_{SL\gamma LV}$. Note the introduced assignments:

- The advancing liquid front at $Ca^A \geq 0$ results in a microscopic precursor (monomolecular) vapor (*V*) film formation $\Theta_{SL}^t = \Theta_{SL}^A \rightarrow \Theta_{S(V)L}^{t+\Delta t}$, where Δt represents relaxation time.
- The receding liquid front at $Ca^R \leq 0$ results in a microscopic surface multimolecular film (*F*) formation $\Theta_{S(F)L}^t = \Theta_{S(F)L}^R \rightarrow \Theta_{S(V)L}^{t+\Delta t}$, where Δt represents relaxation time.

Sufficient time (Δt) must obviously be allowed before measurements are made. The limiting contact angle extrapolated from low-*Ca* range corresponds to apparent contact angle ($\lim\Theta_{SL}^t \rightarrow \Theta_M{}^*$) which is uncorrected for surface roughness. For advancing liquids $\Theta_{SL}^t \rightarrow \Theta_{S(V)L}^A$ and for receding liquids $\Theta_{SL}^t \rightarrow \Theta_{S(F)L}^R$. The microscopic Θ_m^0 relates to the slope of meniscus at interface (inner region). Eq. (88) applies for sessile drops when macroscopic hydrodynamic length is, $L_M \approx L_{cap}$ and when microscopic wedge length, l_S = slip or l_C = cutoff length is close to d_L (Table 12). The latter represent the few vapor layers on solid surface for which no-slip boundary of classical hydrodynamics does not hold. For wetting ($Ca^A > 0$) and dewetting ($Ca^R < 0$) branches, L_M (mm) and l_S (nm) should be, respectively, of reasonably size. Moreover, $\ln(L_M/l_S)$ and $d(\Theta_{SL}^t)^3/dCa$ should remain nearly the same and symmetric ($Ca^A \leftrightarrow Ca^R$), which can be used as check for internal consistency. Considering L_M as the maximum possible dimension of the system (maximum drop size, half-width of slots or capillary radius) the maximum slip length may be derived [41] as:

$$l_S^{\max} = L_M^{\max} e^{-1/9\left(d\left(\Theta_M^t\right)^3/dCa\right)} \tag{89}$$

A reference characteristic microscopic length (l_S) is calculated using the suggested physically acceptable $L_M/l_S = 12$ and $L_M = L_{cap}$. As shown in Table 12 the obtained l_{cap} is, however nearly a decade larger than corresponding molecular dimension (d_L) or equilibrium molecular distances (l_{LL}). The quasi-static form of meniscus implies an equivalence of different definitions of Θ_M^t in *HD* models. Linear and symmetric $\Theta_M^3 - Ca$ plots are expected if Θ_m^0 remain constant. As illustrated in Fig. 17 deviations and non-symmetry are found at small *Ca* (low rates, slip-stick range), which result in the extremely unrealistic small l_S^A and l_S^R values recorded in Table 15.

Voinov modified the characteristic macroscopic length for small drops, narrow slots, and thin capillaries (geometries of the system) for which gravity is negligible. He found that one could account for the geometry of systems by normalizing L_M by a numerical constant k_V. Cox-Voinov eq. (88) becomes [44]:

$$\left(\Theta_V^t\right)^3 = \left(\Theta_m^0\right)^3 \pm 9\ Caln\left(\frac{L_M/k_V}{l_S}\right) = \left(\Theta_m^0\right)^3 \pm 9\,Caln\left(\frac{L_V}{l_S}\right) \tag{90}$$

where $L_V = L_M/k_V$. As indicated, $(\Theta_V^t)^3$ is determined by the slope at the solid wall of the quasi-static part of moving meniscus, $(\Theta_m^0)^3$.Therefore eq. (88) seems unable to provide proper fits to data. The Voinov model (Eq.(90)) predicts independent k_V ($\ln k_V$) values for different liquids, which should remain the same for wetting (advancing) and dewetting (receding) branches. However, using the physically relevant $\ln(L_M/l_S) = 12$ ($L_M/l_S = 1.63{\cdot}10^5$) it is found that k_V varies for different alcohols (Table 15) and for $Ca^A > 0$and $Ca^R < 0$ branches [41].

Zhou and Sheng identified specific friction generated by the pinning of the moving *tpcl* on surface sites. A master curve for different slip models were obtained when l_S were normalized by a constant k_Z specific to their model [45,46] as:

$$\left(\Theta_Z^t\right)^3 = \left(\Theta_m^0\right)^3 \pm 9\ Caln\left(\frac{L_M}{l_S/k_Z}\right) = \left(\Theta_m^0\right)^3 \pm 9\,Caln\left(\frac{L_M}{l_Z}\right) \tag{91}$$

where $l_Z = l_S/k_Z$. According to Zhou-Sheng model $(\Theta_Z^t)^3 - Ca$ should be asymmetric if k_Z has different signs and/or values for wetting and dewetting. Physically relevant $\ln(L_M/l_S) = 12$ values used with Zhou and Sheng model (Eq.(91)) resulted in k_Z which varied both for different alcohols (Table 15) and for $Ca^A > 0$and $Ca^R < 0$ branches. By unifying Voinov and Zhou-Sheng approaches we find [41] that:

$$\left(\Theta_{VZ}^t\right)^3 = \left(\Theta_m^0\right)^3 \pm 9\ Caln\left(\frac{L_M/k_V}{l_S/k_Z}\right) = \left(\Theta_m^0\right)^3 \pm 9\,Caln\left(\frac{L_V}{l_Z}\right) \tag{92}$$

Eq. (92) predicts symmetric advancing and receding branches if k_V and k_Z, respecttively are independent on the direction of *tpcl* motion. For small drops L_M may be substituted by their maximum size; for small sessile drops by their height ($k_V = 2.7$, $\ln k_V = 1.0$), for narrow slots by the half-width of the slot ($k_V = 4.5$, $\ln k_V = 1.5$) and for thin capillaries by their radii ($k_V = 6.1$, $\ln k_V = 1.8$) [41]. The k_V values for silica fibers presented in Table 15 are except for k_V^{HD} of butanol and octanol outside this range. Moreover, only exceptionally l_S^A, l_S^R,λ_B^A and λ_B^R are of (molecular d_L) nanometer dimensions. Therefore, Voinov and Zhou-Sheng models were considered insufficient. Immersing a glass tube in silicon oil at constant tilt angle (complete wetting) resulted in constant *Ca*-values in the range $2.8{\cdot}10^{-4} < Ca < 8.3{\cdot}10^{-2}$ [47]. A straight line was obtained when $\Theta_{SL}^3$was plotted against *Ca*, which passed through origo ($\Theta_{SL}^3 = 0$, $Ca = 0$). The slope, $\ln(L_V/l_S) = 13.66$ is larger as compared to reference $\ln(L_M/l_S)$ =12 but closer to $\ln(L_{cap}/d_L)$ values shown in Table 15. The slip length calculated using eq. (90), $k_V = 1.0$ and L_{cap} (Table 15) gives $l_S = 1.7$ nm. Choosing maximum recommended $L_V = 6.05$ decreases $l_S = 0.28$ nm [41]. Both values are physically reasonable which shows that *HD* model for complete wetting are in quantitative agreement with experimental results.

The presented theories assume that microscopic $\Theta_m^0 \approx \Theta_{S(X)L}^Y$ and predicts that they remain constant during wetting ($Ca^A > 0$) and dewetting ($Ca^A < 0$). This assumption does in most cases do not apply as illustrated in Fig. 17, since it disregards *tpcl* relaxation. It implies that an additional frictional force influences *tpcl* movement. Instead of using commonly used *tpcl* surface friction force (F_γ^s/(mN/m) Eq.(66), Blake summarized published observations as a complex relationship [16,41,45–48]:

$$F_B^{HD} \approx k_B^{HD} Ca^n \quad \Leftrightarrow \quad cos\Theta_m^t = cos\Theta_B^0 \mp k_B^{HD} Ca^n \tag{93}$$

where minus represents wetting and plus represents dewetting. Using recommended limiting maximum $Ca = 5.5{\cdot}10^{-3}$ the friction force without unit becomes for advancing front: 0.087 (EtOH), 0.074 (BuOH) and 0.104 (OcOH) and for receding front: 0.389 (MeOH), 0.299 (EtOH), 0.193 (BuOH) and 0.129 (OcOH) [41]. Replacing $\cos\Theta_m^0$ in eq. (88) by eq. (93) we obtain for the advancing and receding dynamic contact angles (note signs) [41]:

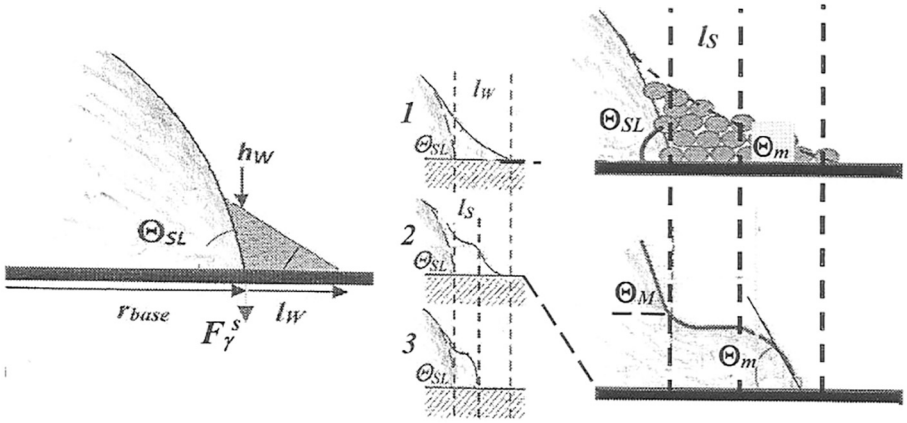

Fig. 20. Three alternative liquid profile close to three-phase contact-line (*tpcl*) of a liquid front: *1*. Near equilibrium (very low transport rates) a vapor wedge extends *tplc* close to solid-liquid contact point by l_W. *2*. Increasing transport rate the liquid-vapor curvature is deformed due to hydrodynamic drag and increased interaction. *3*. At high rates the wedge disappears, and liquid flow occurs through a window defined by the thick film height, h_F (disussed later).

$$\left(\Theta_B^0\right)_A^3 = \left[arccos\left(cos\Theta_m^0 - k_B^{HD}Ca^n\right)\right]^3 \Rightarrow \left(\Theta_{VZ}^t\right)^3 = \left(\Theta_B^0\right)_A^3 + 9\,Caln\left(\frac{L_V}{l_Z}\right) \tag{94a}$$

$$\left(\Theta_B^0\right)_R^3 = \left[arccos\left(cos\Theta_m^0 + k_B^{HD}Ca^n\right)\right]^3 \Rightarrow \left(\Theta_{VZ}^t\right)_R^3 = \left(\Theta_B^0\right)_R^3 - 9\,Caln\left(\frac{L_V}{l_Z}\right) \tag{94b}$$

Zhou and Sheng ascribed the contact angle friction to its pinning at solid surface sites and defined the friction constant [45,46] as:

$$k_B^{HD} = 1.3k_f\sqrt{\frac{\pi^3\gamma_{LV}\rho_{LV}\lambda_B^{HD}}{\eta_L^2}} \tag{95}$$

where the distance between sites, $\lambda_B^{HD} = l_j/k_f(l_j =$ molecular jump lengths normalized by dimensionless constant, $0 < k_f < 1$. Results from fits are listed in Table 15. Although the distances between sites $\lambda_B^{HD}$are of reasonable magnitude, the physical meaning of eqs. (94a) and (94b) remain unclear since k_B and exponent n remain unspecified.

6.3. Combined molecular-hydrodynamic (MH) models

Although both improved Hydrodynamic (*HD*) and Molecular Kinetic (*MK*) models were to some extent satisfactory, their shortcoming in reproducing physically relevant data is a disappointment. Comparison of extracted data show that the spread is very large, $10^{-5} < l_S/\text{nm} < 10^4$, $10^{-5} < \kappa^o/\text{s}^{-1} < 10^{10}$ and $0.1 < \lambda/\text{nm} < 10$, which deviates from physically relevant values. One key problem was non-constant limiting microscopic contact angle caused by the slip-stick region. In addition to the viscous drag within bulk liquids there is a non-viscous resistance extending a part into the wedge. This raises a conflict between no-slip condition within sessile drop and unbound viscous stresses upon liquid movement. In order to enforce fits also over the unstable slip-stick *Ca*-range the wedge was divided into three mutually interacting zones:

- A quasi-static (outer) zone represented by bulk liquid (capillary length L_{cap} or r_{base}). The process is dominated by flow resistance caused by bulk viscosity dissipation. The geometry of the system affects the liquid interface profile.
- A transition (intermediate) zone is introduced to remove viscous stress singularity arising from the no slip boundary condition. Viscous and capillary forces determine the hydrodynamics and shape of the liquid-vapor (*LV*) interface. The liquid is allowed to slip (l_S) over several sites within this zone which corresponds to the first layers adjacent to solid surface.
- A molecular (inner) wedge zone, where solid-liquid (*SL*, adhesion), liquid-liquid (*LL*, cohesion) physicochemical interaction and disjoining forces are dominating. The molecular oscillations at surface sites (potential wells) at *tplc* is characterized by κ-frequency. The geometry of the system is assumed not to affect the liquid shape profile. Conventional hydrodynamics encounters difficulties in this zone so that the wedge is usually excluded from bulk liquid considerations.

The three-zone model is illustrated in Fig. 20.

The combined Molecular-Hydrodynamic (*MH*) model is expected to provide characterization of the slip-stick range between linear low- and high-*Ca* ranges identified previously. It is assumed that the microscopic equilibrium contact angles have a strong dependence on contact line velocity. By replacing Θ_m^0 in *HD*-model defined in eq. (88) with an arccos function of *MK*-model, we find [49] that:

$$\left(\Theta_m^{0,MH}\right)_A^3 = arccos\left[cos\Theta_m^0 - \left(\frac{2N_\lambda^s kT}{\gamma_{LV}}\right)arcsinh\left(\frac{v_{tpcl}}{2\kappa_{tpcl}^0\lambda^{MH}}\right)\right]^3 \tag{96a}$$

The advancing dynamic *tpcl* movement may now be expressed [49] as:

$$\left(\Theta_M^A\right)^3 = \left(\Theta_m^{0,MH}\right)_A^3 + 9\;\; Caln\left(\frac{L_M}{l_S}\right) \tag{96b}$$

where κ, λ and l_S are fitting parameters. For receding liquids the sign in eqs. (96a) and (96b) should be reversed. This *MH*-model considers nonhydrodynamic friction at *tpcl* and viscous friction in transition (intermediate) zone. Blake replaced κ_{tpcl}^0 by κ_{tpcl}^s(Eq.(83)). The resulting frictional force may be expressed [16] as:

$$F_B^{MH} = 2N_\lambda^s kTarcsinh\left(\frac{\eta_L v_L v_{tpcl}}{2\kappa_B^s\lambda_B^{MH}h}\right) \tag{97}$$

Applying this procedure on *MH* model (Eq.(96a)) for advancing wetting process we find that:

$$\left(\Theta_m^{0,MH}\right)_A^3 = arccos\left[cos\Theta_m^0 - \left(\frac{2N_\lambda^s kT}{\gamma_{LV}}\right)arcsinh\left(\frac{\eta_L v_L v_{tpcl}}{2\kappa_B^s\lambda_B^{MH}h}\right)\right]^3 \tag{98a}$$

The corrected advancing dynamic *tpcl* movement may now be expressed (Eq.(98a)) [41] as:

$$\left(\Theta_B^A\right)^3 = \left(\Theta_m^{0,MH}\right)_A^3 + 9\;\; Caln\left(\frac{L_V}{l_S}\right) \tag{98b}$$

Note that Voinov length (L_V) has been used in data fitting. For real surfaces the extrapolated contact angle Θ_m^0 should be replaced by the

Table 16
Liquid molecule diameters (d_L), apparent contact angles (Θ_m*), distances between surface sites (λ) and rate constant (κ^0) derived from a fit of Molecular-Hydrodynamic model (Eqs.(96a),(96b)) to entire Ca^A-region (left three columns) and to low-*Ca* range of advancing (*A*) and receding (*R*) branches (middle three columns). Last κ_B^{MH} column represents rate constant fit of modified Molecular-Hydrodynamic model (Eqs.(98a),(98b)). Molecular diameter (d_L) and capillary length (L_{cap}) used to calculate l_S are inserted for comparison [22,41].

	Θ_m*	λ^{MH}	κ^{MH}	d_L	Θ_m^0	λ^{MH}	κ^{MH}	l_S	L_{cap}	κ_B^{MH}
Liquid	deg	nm	s^{-1}	nm	deg	nm	s^{-1}	m	mm	s^{-1}
H_2O	54.1	1.0	$1.18*10^4$	0.385					2.73	
C_1OH				0.505	66.2	5.4	$6.1\cdot10^2$	$1.7*10^{-12}$	1.69	$3.5*10^4$
C_2OH				0.570	60.0	6.4	$2.9\cdot10^1$	$1.4*10^{-13}$	1.69	$4.8*10^3$
$1\text{-}C_4OH$				0.662	63.5	6.2	2.5	$3.3*10^{-10}$	1.77	$1.6*10^3$
$1\text{-}C_8OH$				0.793	68.0	6.2	$1.7\cdot10^{-1}$	$1.9*10^{-11}$	1.83	$5.0*10^2$
$HCONH_2$	30.5	1.1	$5.57*10^4$	0.504					2.31	
$H_4C_2(OH)_2$	33.5	1.4	$2.18*10^3$	0.562					2.11	
$H_5C_3(OH)_3$	46.0	0.8	$5.30*10^3$	0.614					2.29	

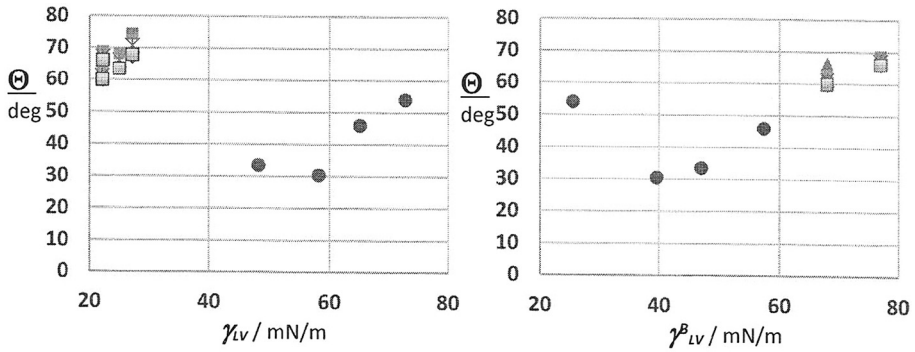

Fig. 21. Apparent (Θ^*_{SL}, spheres) and limiting advancing (Θ^A_{SL}, triangles) *MK* contact angles. Advancing (Θ^A_{SL}, squares), receding (Θ^R_{SL}, diamonds) and effective (Θ^{eff}_{SL}, asterisks) *MK* contact angles. Advancing (Θ^A_{SL}, shaded squares) *MH* contact angles. Dependence on surface tension (left diagram) and on base component of surface tension (right diagram).

apparent contact angle Θ_m* or corrected to equilibrium (Young, Θ^Y_m, Eq. (69)) or effective (Θ^{eff}_m, Eq.(85)) because *MK* theory requires a unique static value. Results for fits of *MH* models to experimental data is presented in Table 16.

Comparing results from Tables 3 and 4 with those in Tables 13 and 16 it is found that no actual improvement is achieved as compared to previous *MK* and *HD* models. The rate constants (κ) and site-distances (λ) are nearly equal and within expected ranges. Since symmetric *MH* model fits data over all advancing and receding v_{tpcl} or *Ca* values it implies that inflection point represents the transition from *tpcl* to bulk viscous friction. In general, it is expected that the extracted data would be representative. The distance between sites are significantly larger than molecular (d_L) order $0.5 < \lambda/\text{nm} < 1.0$. Overall, extracted κ-values are many orders of magnitude smaller than the average molecular displacement rate ($10^6\ s^{-1}$), rate constant for free diffusion ($10^9\ s^{-1}$) and rates for viscous flow of simple liquids ($10^{11}\ s^{-1}$) [22,41]. The L_V/l_S ratio is too high. Assuming $l_S = 1.0$ nm gives $k_V = 1.48\cdot10^3$ which is two order of magnitude larger than $2.7 < k_V < 6.1$ predicted for small drops, slots, and capillaries [41]. Since l_S extracted from eq. (96) were either not constant or too large as compared to molecular dimensions they were omitted as not physically meaningful [22]. The λ and κ values indicate, however that adsorption (wetting, *A*) and desorption (dewetting, *R*) at *tpcl* is the dominating *MH* mechanism at low velocities and bulk viscous dissipation becomes more important at high velocities. As sown, however the asymmetry of these effects for the wetting and dewetting modes is nontrivial. The three zone *MH* model seems to provide a better fit to experimental data, but the extracted λ and κ values remain almost identical to those extracted from the two-zone *MK* model.

The dependence of contact angles, site distances and logarithmic rate constants on surface chemistry of probe liquids can be evaluated. Fig. 21 illustrates the dependence of contact angles of all *HD*, *MK,* and *MH* models on surface tensions.

As shown, only when fitted as a function of the base component of probe liquid surface tension all contact angles arrange themselves on a

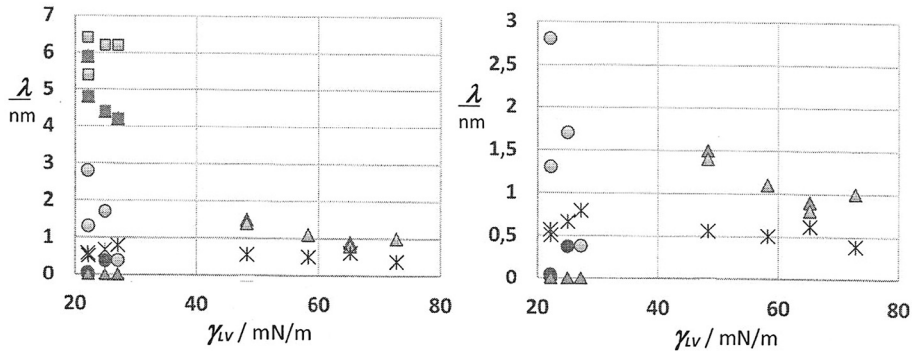

Fig. 22. Site distances (λ/nm) extracted from *HD* model fits to advancing (filled circles) and receding (shaded circles) liquid front, from *MK* model fits to advancing (filled and patterned triangles) and from Blake corrected *MK* model fits (filled squares) to liquid front, and from *MH* model fits to advancing (shaded triangles) and receding (shaded squares) liquid front. Molecule diameter (d_L/nm) of probe liquids (asterisks) are added for comparison. Plots are made as a function of liquid surface tensions. Expanded site distance length scale (right diagram).

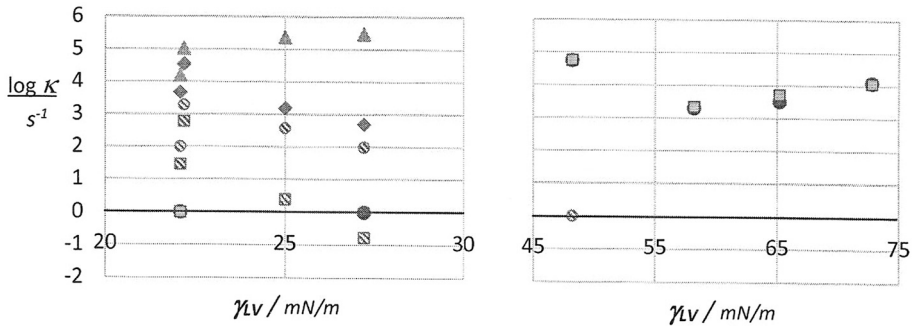

Fig. 23. Logarithmic dependence of rate constants on small surface tension of probe liquids (left diagram) and on large surface tensions (right diagram). Spheres ($\log\kappa^A$) and triangle ($\log\kappa_B^s$) from Table 14. Squares ($\log\kappa^A$) and diamonds ($\log\kappa_B^s$) from Table 15.

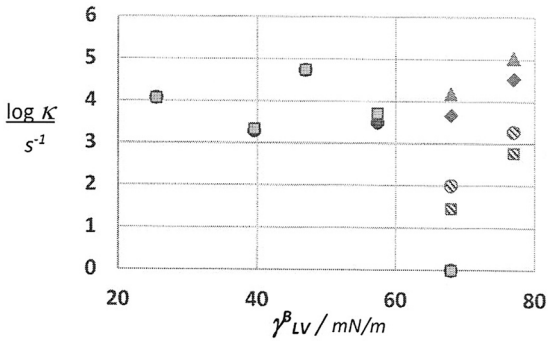

Fig. 24. Logarithmic dependence of rate constants on base component of probe liquid surface tensions. Spheres ($\log\kappa^A$) and triangle ($\log\kappa_B^s$) from Table 14. Squares ($\log\kappa^A$) and diamonds ($\log\kappa_B^s$) from Table 15.

master curve. There is a substantial dependence of basic model parameters (contact angles) on probe liquid chemistry (surface tensions). Unfortunately, only limiting microscopic contact angles were available for water, formamide, ethylene glycol and glycerol (glycerine). Except for separately determined apparent contact angles, all contact angles extracted as a part of model fits remain nearly indistinguishable. Extracted distances between surface sites are plotted together with molecule diameter of liquid molecules in Fig. 22.

As shown, the Blake modification of *MK* and *MH* models (squares) result in a decade too large site distances. Site distances extracted from *HD* model (circles) are extremely dependent on probe liquids and resulted in unphysical l_S values. Site distances extracted from *MK* and *MH* model fits (triangles) are reasonably close to molecular dimensions (d_L, asterisks) and equally dependent on surface tension. Since κ-values were one or more order of magnitude to small as compared to reference value ($\kappa = 10^6\ s^{-1}$) they are plotted on logarithmic scale in Fig. 23 as a function of total probe liquid surface tensions.

All surface tensions of alcohols are very low as compared to other liquids listed in Table 11. Therefore, the surface tension is expanded in left diagram. Most $\log\kappa^A$ are descending with increasing surface tension, but Blake's $\log\kappa_B^s$ is ascending. The rate constants extracted from *MK* and *MH* models are nearly the same, except for alcohols. As shown in Tables 3 and 4*MK* fits to ethylene glycol and water on model papers produce $\log\kappa$ values which are close to reference $\log\kappa^A = 6$. In Fig. 24 logarithmic rate constants are plotted as a function of base component of probe liquid surface tensions.

The $\log\kappa$ dependencies on base component of surface tension is almost reversed as compared to (total) surface tension. The $\log\kappa$ of water, formamide, ethylene glycol and glycerol (glycerine) remain almost constant, while $\log\kappa$ for alcohols (only MeOH and EtOH available) increases with their base component of surface tension. The average difference from reference $\log\kappa = 6$ is two orders of magnitude.

6.4. Summary

Two-dimensional spontaneous wetting is replaced by one-dimensional forced complete wetting to enhance wetting rate (enlarge *Ca*-range) and to enable successive advancing and receding wetting cycles.

The expected symmetric advancing and receding cycles and constant limiting microscopic contact angles (Θ_m^0) were not obtained. The N_λ^s, λ, κ_{tpcl}^0 parameters extracted from linear molecular-dynamic (*MK*) model were not in the expected range.

MK- model was modified by reducing equilibrium quasi-equilibrium rate constant (κ_{tpcl}^0) by a surface component (κ_B^s). This procedure did, however not improve results.

Since slip-stick instability resulted in variable limiting contact angles extracted from advancing and receding branches, an arithmetically averaged effective contact angle was suggested. Gibbs' hysteresis energy was determined from advancing and receding contact angles.

The dependence of cube of contact angle on *Ca* in hydrodynamic (*HD*) model is interpreted as logarithmic ratio of characteristic macroscopic and microscopic lengths. This corresponds to wetting rate dependent buildup of fractal objects. To improve fitting, both characteristic macroscopic and microscopic lengths were normalized (divided) by reference constants. The lengths extracted from this model were however unphysical. Independent linear fits of equations to $Ca^A > 0$and $Ca^R < 0$ branches did not provide improved n, k_f, k_V, k_Z values. No improvement of *HD* model were thus able to explain the observed non-symmetric $\Theta_M^3 - Ca$ (slip-stick) dependence at low Ca. The *HD* model was altogether rejected due to exceedingly poor fits.

A complex exponential friction contribution was used to modify time-dependence of contact angles. In this way more reasonable characteristic lengths were found, but the mechanism became unclear.

Since the slip-stick behavior caused problems for both *MK* and *HD* models, the two (bulk–wedge) phase equilibrium was exchanged for a three (bulk–(slip-stick)–wedge) equilibrium. The expansion was realized by introducing *MK* model as microscopic contact angle of *HD* model.

The molecular-hydrodynamic (*MH*) model produced improved fits, but the extracted N_λ^s, λ, κ_{tpcl}^0, κ_B^s and characteristic lengths remained unacceptable.

Overall, an increased number of adjustable parameters introduced to *HD*, *MK* and *MH* models resulted in improved fitting to experimental data, but makes it simultaneously increasingly difficult to interpret the scattered extracted parameters in terms of primary basic physicochemical properties.

When evaluating influence of physicochemical interactions between probe liquids and solid surface sites, a more advanced characterization of liquids and solids is needed. It was shown that van der Waals (dispersive, Lifshitz-van der Waals), polar (Lewis acid-base) and Brϕnsted hydrogen bonding are useful in data fitting.

When evaluating the success of improved *MK*, *HD*, and *MH* models, one gets the impression of a purely mathematical exercise in curve

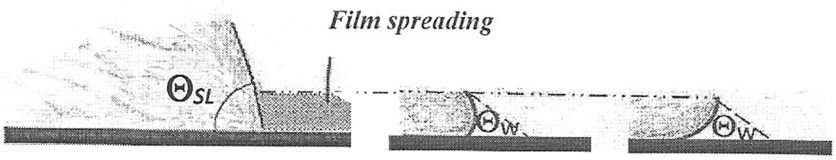

Fig. 25. When the liquid film spreading rate increases (from left-to-right) the wedge (left) bends forming a vertical window (middle) and finally a half-parabola (right).

fitting. Little attention is given to the interconnection between solid surface structure since no data is corrected for roughness before attempting to evaluate wetting processes. Even nano-scale surface roughness may influence wetting properties. It has been shown that only when corrected for surface structure, wetting can be related to physicochemical interaction between solid surface sites and surface tension components of probe liquids. Although the unstable slip-stick *Ca*-region is clearly detected, the steady-state *HD*, *MK* and *MH* models are forced to cover extended *Ca*-values to non-recommended ranges. No wonder that extracted key parameters become of reduced physical relevance.

7. Viscous flow of thick films on surfaces

Two-dimensional spreading (wetting) was considered as volumetric, thin film flow. Thin films were allowed to grow if sufficient vapor is available. Fig. 25 shows that the shape of reasonably thick liquid wedges are dependent on spreading velocity.

The liquid flow is represented by volumetric liquid flow normalized by a circular window of height h as:

$$\frac{(dV/dt)}{A_\phi} = \frac{\pi R_{base}\, h(dR)/dt}{2\pi R_{base}\, h} = \frac{dR_{base}}{2\,dt} \tag{99}$$

where R_{base} is the sum of sessile drop base radius (r_{base}) and wedge radius (r_{wed}), $R_{base} = r_{base} + r_{wed}$. Combined with d'Arcy equation for linear volumetric flow we find [10] that:

$$\frac{dR_{base}}{2\,dt} = \frac{D_V^s}{\eta_L}\left(\frac{\Delta P}{R_{base}}\right) \tag{100}$$

where the linear pressure gradient is negative for decreasing pressure and positive for increasing pressure. D_V^s is the surface permeability for liquid flow. Integration of eq. (100) yields:

$$\int R_{base} dR = \frac{2D_V^s \Delta P}{\eta_L}\int t \quad \Leftrightarrow \quad R_{bse}^2 = \frac{4D_V^s \Delta P}{\eta_L}\, t \quad \Leftrightarrow \quad \frac{dR_{base}^2}{dt} = \frac{4D_V^s}{\eta_L}\Delta P \tag{101}$$

Introducing Hagen-Poiseuille surface permeability ($D_V^s = 2\pi R_{base} h/8$) we find two limiting cases: (1) The influence of interfacial chemistry may be evaluated by interpreting ΔP in terms of Laplace pressure. Focusing on two-dimensional forces and a vertical (no radius of curvature) liquid wedge of constant height (h_W) the wetting rate is given by:

$$\frac{dR_{base}^2}{dt} = \pi h_W\left(\frac{\gamma_{LV}}{\eta_L}\right) = \pi h_W v_{hd} \tag{102a}$$

where (γ_{LV}/η_L) is a characteristic hydrodynamic velocity (v_{hd}). (2) If the spreading wedge has a curved meniscus (r_{men}) determined by its contact with the solid, this must be accounted for when defining local Laplace pressure in terms of curvatures as:

$$\frac{dR_{base}^2}{dt} = \pi R_{base}\, h_W\left(\frac{\gamma_{LV}}{\eta_L}\right)\left(\frac{1}{R_{base}} + \frac{cos\Theta_{SL}}{r_{men}}\right) \tag{102b}$$

Alternatively, the hydrodynamic properties of a forced steady-state one-dimensional laminar flow of liquids between two ideal plates at a distance 2 h is evaluated. Neglecting gravity, we find for a half-parabola liquid transport:

$$\frac{dP}{dl} \approx \frac{\Delta P}{l} = \eta_L\left(\frac{d^2 v}{dh^2}\right) \tag{103}$$

Integration with respect to h and inserting boundary conditions (no slip at solid-liquid interface) gives the parabolic velocity [4,11]:

$$v_{para} = \frac{h(v)^2 - h(0)^2}{2\eta_L}\left(\frac{F_v}{l}\right) \tag{104}$$

where ΔP has been exchanged for the force F_v per unit area used to maintain steady-state flow. Two limiting cases may be identified [4,11]. (1) The liquid velocity is maximum at the top of half-parabola (in the center between the plates):

$$v_{\max} = \frac{h^2}{2\eta_L}\left(\frac{F_v}{l}\right) \tag{105}$$

The average velocity is given [4,11] by:

$$v_{ave} = \frac{2}{3}v_{\max} = \frac{h^2}{3\eta_L}\left(\frac{F_v}{l}\right) \tag{106}$$

Eq. (106) can also be expressed as radial spreading. Since the wedge flow is dominated by hydrodynamics only the curvature of circular flow needs to be accounted for when assigning the local Laplace pressure [4,11] as:

$$v_{ave} = \frac{h^2}{3R^2}\left(\frac{\gamma_{LV}}{\eta_L}\right) = \frac{h^2 v_{hd}}{3R^2} \tag{107}$$

where γ_{LV}/η_L is the characteristic hydrodynamic rate. Considering an irregular media between the plates, the average velocity must be multiplied with porosity to obtain the velocity by which liquid exits the plates. Then, the Hagen-Poiseuille permeability has to be exchanged for more representative relationships [4,11].

7.1. Summary

For macroscopic thick films the volumetric flow is normalized by the window through which flow occurs. D'Arcy equation provides a relationship for viscous flow and Hagen-Poiseuille an approximation for permeability. Depending on the meniscus shape two Laplace pressure alternatives may be identified.

Forced steady-state wetting may be modeled by laminar flow behavior between two parallel plates from which maximum and average flow rates may be derived. For irregular (porous) media the average velocity must be multiplied by porosity to obtain exit flow. Then, the Hagen-Poiseuille permeability must be exchanged for more realistic models.

8. Transport phenomena

Improved *HD* and *MK* and *MH* models were designed based on data accumulated from forced wetting (advanced liquid front) and forced dewetting (receding liquid front) at nearly ideal solid surfaces. Since the results were disappointing, established phenomenological relations known from irreversible thermodynamics are offered to improve existing models. Forced wetting may be expressed as generalized fluxes,

Table 17
Processes expressed in terms of conjugate extensive (X) and intensive (Y) state functions. The unit of $X{\cdot}Y$ should be Joule [1].

Process	Extensive (X)	Intensive (Y)
Heat	Heat, q_T	Temperature, T
Mechanical	Volume, V	Pressure, P
Chemical	Amount, n	Chem.potential, μ
Electric	Charge, q_E	Electric potential, ψ

which can be made dependent on several coupled conjugate generalized forces. With these forces particular physicochemical properties influencing forced wetting can be identified.

8.1. Thermodynamic considerations

The systems have hitherto been considered mechanical where the internal energy is at minimum and the sum of forces acting on the system is zero. In such systems temperature is not involved and entropic contributions do not play any roles.

Changes of internal energy of homogeneous bulk phases are expressed as a sum of conjugate state functions [4,5] as:

$$dU = TdS - PdV + \Sigma_i \tilde{\mu}_i dn_i = TdS - PdV + \Sigma_j \mu_j dn_j + \Sigma_k \psi_k dq_k \quad (108)$$

where electrochemical potential is $\tilde{\mu}_i = \mu_j + z_k F \psi_k$ (J/mol), n_j represents amount of neutral molecules and n_k (mol) amount of ionic species. The charge of each ionic species is $q_k = z_k F n_k$(C). Gibbs-Duhem rule states [4,5] that:

$$SdT - VdP + \Sigma_j n_j d\mu_j + \Sigma_k q_k d\psi_k \equiv 0 \quad (109)$$

As shown in Table 17 internal energy is defined in terms of conjugate extensive (X) and intensive (Y) state functions.

In reversible equilibrium systems heat change was replaced by entropy. In irreversible systems heat is considered an entropy production (dS/dt) which, especially for isothermal processes equals entropy dissipation (rate at which work is exchanged to heat). Entropy change is subdivided into an external contribution d_eS (interaction with surrounding) and an internal contribution d_iS (internally produced entropy). For reversible processes $d_eS = dq_T/T$ and $d_iS = 0$ [4].

Thermodynamics of irreversible processes is introduced since classical thermodynamics does not apply to non-equilibrium situations. For irreversible processes $d_iS > 0$. The rate of entropy production is coupled to conjugate fluxes and forces since they determine the rate at which a disrupted system returns to equilibrium [13]. When internal and/or external forces are applied on the system, it results in time-dependent processes. Such forces may be *directional forces* which, over a sufficiently long time operate in more or less same direction. Alterna-tively, *stochastic forces* may be considered which change from moment to moment in a random way [4]. Two system dependent time scales, (sufficiently) long and (momentary) short must therefore be considered.

The driving force for transport processes have a mechanical or electrical origin but may also have a thermodynamic origin. We shall therefore employ a generalized $F_Y = \text{grad}Y$ (grad$Y$ = linear work or potential energy gradient) notion of force. Transport can be treated on a macroscopic (phenomenological) or on a molecular (nanoscopic) level. Any molecular transport model must always be compatible with macroscopic behavior.

Transport models are related to characteristic macroscopic and molecular (nanoscopic) length scales which differ within the system. The length scales of these non-uniformities are macroscopic but may be much smaller than the size of the system. On the other hand, they must remain large compared to molecular distances. Hence, we are dealing with intermediate length scales. Transport occurs in and out of volume elements which are of intermediate size. They are small enough to allow only small gradients across them, but large enough to consider them macroscopic [4,50].

Table 18
Established relationships (laws) between flux (J_X), phenomenological coefficient (L_{XY} = inverse resistance), force and transport process [4,50]. The unit of $X{\cdot}F_Y$ should be Newton.

Law	$J_X = (dX/dt)/A_\phi$	$L_{XY} = J_X/F_Y$	$F_Y = \Delta Y/l$	Transport
Fourier's	$X = q_T$ [J/m^{2}s]	λ_T [J/Kms]	$\Delta T/l$ [K/m]	Heat
Fick's	$X = n$ [mol/m^{2}s]	D_c [m^2/s]	$\Delta c/l$ [mol/m^4]	Amount
Fick's	$X = n$ [mol/m^{2}s]	$D_c c/RT$ [mol^2/Jms]	$\Delta\mu/l$ [J/molm]	Amount
Ohm's	$X = q_E$ [C/m^{2}s]	κ_E [S/m]	$\Delta\psi/l$ [V/m]	Charge
d'Arcy's	$X = V$ [m/s]	D_V/η [m^4/Ns]	$\Delta P/l$ [N/m^3]	Volume
Newton's	$X = l$ [1/ms]	$1/\eta$ [m^4/Ns]	τ/l [N/m^3]	Momentum
Newton's	$X = \rho\, l$ [kg/m^{4}s]	$1/\mu$ [s/m^2]	τ/l [N/m^3]	Momentum

where λ, κ = conductivity, D_c = diffusivity and D_V = permeability. A_ϕ denotes cross-sectional area of window to volume element. Phenomenological linear laws like those in Table 18 do not generally comply with the unit of product of flux and force. They have been formulated to account for familiar physical properties without having an interpretation in terms of irreversible thermodynamics and do not all adhere to Eq. (109) [4]. As indicated, $dS_i > 0$ for irreversible processes for which entropy production equals the product of conjugate fluxes and forces:

$$\frac{1}{V}\left(\frac{dS_i}{dt}\right) = \Sigma_j J_j F_j = \Sigma_j \left(\frac{dX_j/dt}{A}\right)\left(\frac{dY_j}{dl}\right) \quad (112)$$

All transport phenomena have in common that they involve one or more flows (fluxes) induced by one or more applied force(s). A basic element in the mathematical description is conservation of mass (amount) and conservation of momentum (equation of motion). Generally, the conservation of a given extensive property X can be represented as related rate of changes in and out of a reference unit volume reduced by rate of production which equals rate of accumulation. The considered process determines the relative importance of alternative extensive properties (X). Experience has shown that for several transport phenomena, the flux is proportional to the driving force divided by resistance. The nature of resistance depends on the process under consideration, and its dimensions are determined by the dimension of force. For a unidirectional single component flow, the generalized relationship between conjugated flux (J_X) and force (F_Y) is:

$$J_X = \frac{(dX/dt)}{A_\phi} = L_{XY} F_Y = L_{XY}\, grad Y \approx L_{XY}\left(\frac{\Delta Y}{l}\right) \quad (110)$$

where L_{XY} = phenomenological constant (inverse resistance) and l is a characteristic length. As shown by Table 17 flux equals the rate of extensive variable X per unit entrance cross-sectional area (A_ϕ) to unit volume. Force is expressed as linear length gradient of intensive (work, W) variable Y. To preserve units:

$$L_{XY} = \frac{J_X}{grad\, Y} = \frac{(dX/dt)/A_\phi}{\Delta Y/l} \quad (111)$$

Table 18 collects some relationships between flux (J_X), phenomenological constant (L_{XY} = 1/resistance) and force (F_Y). They are formulated to account for familiar physical properties without having an interpretation in terms of proper irreversible thermodynamics.

Entropy change is expressed per volume, the unit is (J/Km^{3}s). If the driving force for heat is chosen as $gradT^{-1}$ instead of $gradT$ in Table 18 its product with flux has the right dimension, but then the phenomenological coefficient must be multiplied by T^2. Newton's momentum transport is usually expressed in terms of stress tensors (τ_{vis}) [50] as

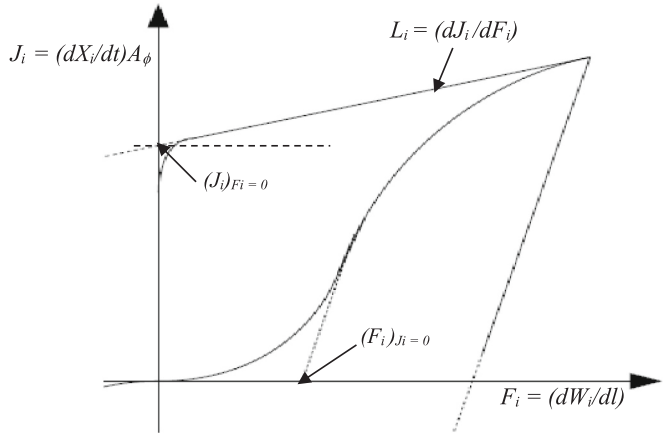

Fig. 26. Dependence of generalized Flux *Ji* on generalized force *Fi* resulting in a hysteresis loop. Intensive variable *Y* is expressed as generalized work *W*.

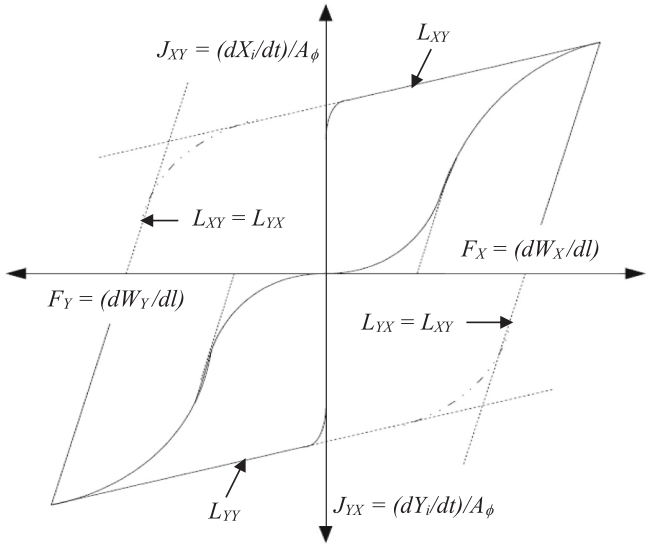

Fig. 27. Generalized force F_X induces a flux J_X which is counteracted by a force F_Y and a flux J_Y coupled by hysteresis loop. Limiting Ostwald's phenomenological constants L_{XX}, L_{YY}, $L_{YX} = L_{XY}$. Intensive variable *Y* is expressed as generalized work (*W*).

$$\tau_{vis} = \frac{F_{vis}}{A_\phi} = \eta_L\left(\frac{\Delta v_L}{l}\right) \tag{113}$$

$$\tau_{vis} = \frac{F_{vis}}{A_\phi} = \frac{\eta_L}{\rho_L}\left[\frac{\Delta(\rho_L v_L)}{l}\right] = \mu_L\left[\frac{\Delta(\rho_L v_L)}{l}\right] \tag{114}$$

where η = dynamic and $\mu = \eta/\rho$ = kinematic viscosity. In order to express stress tensor as N, Newton's law should be converted to d'Arcy's law. Acceleration (inertial) force and gravitation (vertical) force are excluded from the discussion. The ratio between inertial and viscous forces was expressed by dimensionless Reynolds number (Eq.(78)). Fig. 26 illustrates a typical reversible transport process.

Typically flux increases successively when force is applied, from which a characteristic limiting value at $(F_i)_{Ji=0}$ can be extracted. When force is released, it is common that the system maintains a memory at $(J_i)_{Fi=0}$ before thermal agitation brings the system back to equilibrium. The memory is characterized by phenomenological coefficient $L_i = dJ_i/dF_i$ (Eq. (111)).

8.2. Coupled transport

Coupled transport of matter is a result of co- and counteracting fluxes. Expressed as generalized linear transports, coupled fluxes can be expressed as:

$$J_X = \Sigma_Y L_{XY} F_Y \tag{115}$$

This gives an opportunity to control the flux by external forces influencing one of the fluxes more than the other. The near-irreversible balance is illustrated in Fig. 27.

The advantages provided when volume and charge transport (Table 18) are coupled is presented as an example. This corresponds to enforced electrolyte transport at a solid (hollow cylinder, capillary) surface. The simultaneous transport of liquid and charge (ion) flows involves d'Arcy's and Ohm's eqs. D'Arcy's equation represent hydraulic liquid transport. Ohm's equation relates electrolytic current to the electric potential gradient in a resist material. The coupled transport can be expressed in terms of coupled forces [4,24] as:

$$J_V = L_{AA}\,grad P + L_{AB}\,grad\psi = L_{AA}\left(\frac{dP}{dL}\right) + L_{AB}\left(\frac{d\psi}{dl}\right) \tag{116a}$$

$$J_q = L_{BB} grad\psi + L_{BA} grad P = L_{BB}\left(\frac{d\psi}{dl}\right) + L_{BA}\left(\frac{dP}{dl}\right) \tag{116b}$$

where the phenomenological (Ostwald's) constants for single fluxes are defined as $L_{AA}(D_V/\eta_=$ permeability/viscosity) and as $L_{BB}(\kappa_E =$ electrical conductivity). The sign determines the direction of action. Introducing the single terms of single linear fluxes we obtain:

$$J_V = \frac{(dV/dt)}{A_\phi} \approx \frac{D_V}{\eta}\left(\frac{\Delta P}{l}\right) + L_{AB}\left(\frac{\Delta\psi}{l}\right) \tag{117a}$$

$$J_q = \frac{(dq/dt)}{A_\phi} = \frac{I}{A_\phi} \approx \kappa_E\left(\frac{\Delta\psi}{l}\right) + L_{BA}\left(\frac{\Delta P}{l}\right) \tag{117b}$$

The surface potential gradient can be exchanged for an external potential gradient. The advantage with these expressions is that they may be used to determine how rational experiments should be executed to obtain relevant data. We choose a hollow cylinder filled with electrolyte and electrodes mounted at both ends as model system [4,24,50].

The potential difference, which arises due to an external pressure is denoted *streaming potential* (*SP*)

$$SP = \left(\frac{grad\psi}{grad P}\right)_{J_q=0} = \left(\frac{d\psi/dl}{dP/dl}\right)_{J_q=0} = -\frac{L_{BA}}{L_{BB}} = -\frac{L_{BA}}{\kappa_E} \tag{118}$$

It is measured with disconnected current flow and without a shortcut between electrodes.

The counterpart to streaming potential is denoted *electro-osmosis* (*EO*) or electro-osmotic volume flow

$$EO = \left(\frac{J_V}{J_q}\right)_{gradP=0} = \frac{L_{AB}}{L_{BB}} = \frac{L_{AB}}{\kappa_E} \text{ or } \left(\frac{J_V}{grad\psi}\right)_{gradP=0} = L_{AB} \tag{119}$$

It is measured in the absence of an external pressure gradient.

Onsagers's reciprocity principle states that the phenomenological constants must be equal ($L_{AB} = L_{BA}$) which means that:

$$\left(\frac{grad\psi}{grad P}\right)_{J_q=0} = \left(\frac{d\psi/dl}{dP/dl}\right)_{J_q=0} = -\left(\frac{J_V}{J_q}\right)_{gradP} = -\left(\frac{dV/dt}{dq/dt}\right)_{gradP} \tag{120}$$

The liquid volume displaced per unit time is expressed as a product of migration rate and cross-sectional area of the hollow cylinder:

$$\left(\frac{dV}{dt}\right) = vA_\phi = \frac{\varepsilon_o\varepsilon_r\varsigma A_\phi}{\eta}\left(\frac{d\psi}{dl}\right) \tag{121}$$

where ζ is the induced zeta (effective surface) potential. Introducing Ohm's law $(d\psi/dl) = I/A_\phi\kappa_E$ we find the phenomenological constants to

streaming potential and electro-osmosis as:

$$\left(\frac{dV}{dt}\right) = \upsilon A_\phi = \frac{\varepsilon_o \varepsilon_r \varsigma I}{\eta \kappa_E} = \frac{\varepsilon_o \varepsilon_r \varsigma}{\eta \kappa_E}\left(\frac{dq}{dt}\right) \Leftrightarrow \left(\frac{dV/dt}{dq/dt}\right) = \frac{\varepsilon_o \varepsilon_r \varsigma}{\eta \kappa_E} = \frac{L_{BA}}{\kappa_E} \quad (122)$$

Streaming current (*SC*) which is defined as

$$SC = \left(\frac{J_q}{J_V}\right)_{grad\psi=0} = \frac{L_{BA}}{D_V/\eta} = \frac{\varepsilon_o \varepsilon_r \varsigma}{D_V} \text{ or as } \left(\frac{J_q}{gradP}\right)_{grad\psi=0} = L_{BA} = \frac{\varepsilon_o \varepsilon_r \varsigma}{\eta} \quad (123)$$

It is created by an external pressure and is measured with a shortcut between electrodes.

Electro-osmotic counter pressure (*EOP*) is the counterpart to *SC* and caused by an electrical field in the absence of liquid flow is defined as

$$EOP = \left(\frac{gradP}{grad\psi}\right)_{J_V=0} = \left(\frac{dP/dl}{d\psi/dl}\right)_{J_V=0} = -\frac{L_{AB}}{D_V/\eta} = -\frac{\varepsilon_o \varepsilon_r \varsigma}{D_V} \quad (124)$$

It is measured without shortcut between electrodes. One may relate *SC* and *EOP* to Ohm's law by introducing the current associated with volume flow as:

$$dI = \frac{dq}{dt} = \rho_\pm \left(\frac{dV}{dt}\right) \quad (125)$$

where the hydrodynamic liquid flow (dV/dt) is obtained from the integral rate of volume elements. Introduction of volumetric charge density $\rho_\pm = -\varepsilon_o \varepsilon_r (d^2\psi/dl^2)$ and integrating in parts over the horizontal cylinder (limiting conditions were $(\psi)_{l=0} = \zeta$ and $(\psi)_{l=r} = 0$) yields the *streaming current* as:

$$I = A_\phi \frac{\varepsilon_o \varepsilon_r \varsigma}{\eta}\left(\frac{dP}{dl}\right) \quad (126)$$

Introducing Ohm's law $I = A_\phi \kappa_E (d\psi/dl)$ we recover Ostwald's phenomenological constant as:

$$A_\phi \kappa_E \left(\frac{d\psi}{dl}\right) = A_\phi \frac{\varepsilon_o \varepsilon_r \varsigma}{\eta}\left(\frac{dP}{dl}\right) \Leftrightarrow \left(\frac{d\psi/dl}{dP/dl}\right) = \frac{\varepsilon_o \varepsilon_r \varsigma}{\eta \kappa_E} = \frac{L_{BA}}{\kappa_E} \quad (127)$$

Comparison of eqs. (122) and (126) show for the limit of large cylinder radii that the expectations of eq. (121) is fulfilled:

$$\left(\frac{dV/dt}{dq/dt}\right) = \frac{\varepsilon_o \varepsilon_r \varsigma}{\eta \kappa_E} = \left(\frac{d\psi/dl}{dP/dl}\right) \quad (128)$$

This equality is frequently quoted in textbooks of surface and colloid chemistry [4,24]. Ideal steady-state conditions and large pore radii (r_p) has been assumed. The radius of cylinders (r_c) of known length (l) may be obtained from eqs. (116a) and (117a) when the potential difference is adjusted to zero by an external potential as:

$$\left(\frac{J_V A_\phi}{grad\, P}\right)_{grad\,\psi=0} = \left(\frac{dV/dt}{dP/dl}\right)_{grad\,\psi=0} = \frac{A_\phi D_V}{\eta} = \frac{\pi r_c^4}{8\eta} \quad (129)$$

where Hagen-Poiseuille expression for permeability $D_V = r^2/8$ has been introduced. When the double layer within pores or capillaries are thin surface conductance may influence measure-ments. This can be corrected for by relating the apparent (measured) zeta-potential (ζ) to the true one as [4,24]:

$$\frac{1}{\varsigma_a} = \frac{1}{\varsigma}\left(1 + \frac{\kappa_E^s}{\kappa_E^b r_c}\right) \quad (130)$$

where κ_E is the electric conductivity at surface (s) and in bulk (b) solution and r_c is the radius of capillary (pore). A plot of $1/\zeta_a$ against $1/r$ should give a straight line if the pore/capillary radius is large as compared to the double layer thickness and conductivities and zeta potentials remain constant. In reality particular details of the porous media influencing transport must be considered [4,10]. Taking membranes as example the pores ($r_p << l_p$) and their heterogeneity is considered in terms of tortuosity and azimuth angle from linear transfer. Poisson-Boltzmann equation provides the volumetric charge distribution and ζ-potential represents the effective potential close to pore walls. From these constraints detailed models for liquid volume (Eqs.(116a), (117a)) and charge flux (Eqs.(116b),(117b)) were derived [51] for electrolyte transport through track-etched microfiltration polymeric membranes. The Ostwald's constant ratio $L_{BA}/L_{BB} = L_{BA}/\kappa_E$ was determined from eq. (127). It was found that: 1) *SP* increases with pore radius since more charges accumulate on pore walls enhancing surface charge density. 2) *SP* increases with electrolyte concentration due to decreasing diffuse layer thickness or Debye length ($1/\kappa_D$). 3) *SP* decreases with increased counter (cat)ion diffusivity ($Li^+ < Na^+ < Mg^{2+} < Ca^{2+} < Cl^-$) as compared to coions [51]. The surface charge density increases independent on pore radius in absolute number with electrolyte concentration. On the other hand, there was no clear dependence of ζ-potential (expressed as$F\zeta/RT$) on electrolyte concentration or pore radius. An opposite dependence as compared to surface charge density is expected.

This rather advanced investigation has been developed further by specifically determining counterion adsorption into Stern layer of porous alumina membranes by (Langmuir and Freundlich) adsorption isotherms. Sorptometry was used to establish pore sizes, porosity and permeability. Based on double layer (capacitor) model surface charge densities and potentials are assigned to surface, Stern surface, and diffuse layer (ζ-potential) [52]. The complex counterparts to eqs. (116a) and (116b) were used to evaluate expressions for Ostwald's phenomenological constant L_{AB}. Adsorption isotherms for LiCl solutions were employed to determine Cl^- concentration dependent surface charge densities. However, these charges seem to be overruled by cation absorption into alumina membranes [52]. In another investigation the same eq. (118) was used to determine streaming potentials, but extended to account for surface conduction (Eq.(129)) [53] as:

$$SP = \left(\frac{\Delta\psi}{\Delta P}\right)_{J_E=0} = \frac{\varepsilon_o \varepsilon_r \zeta}{\eta}\left[\frac{1}{\kappa_E^B + \left(2\kappa_E^s/r_p\right)}\right] \quad (131)$$

Only for surfaces with low surface conductivity the κ_E^sterm can be omitted. A triple layer model was adopted for further analysis. The charge density of polymeric track-etched microfiltration membranes (equal to [51]) was determined as a function of NaCl concentration. To establish relaxation processes within membranes a voltage is applied which initiates a flow injection and pressure increase. When the system reaches a steady-state the flow injection is stopped, and relaxation potential investigated by an exponential time dependence $\phi^t = \phi^0 \exp(-t\omega)$ where mechanical and electrical potential relaxations contribute to ω of this first-order dynamic system [53]. Streaming potentials were determined from electrical potential which showed linear dependency on pore sizes. Applying a numerical method to solve Poisson-Boltzmann equation for cylindrical geometries, the Galvani potential within pores, ζ-potential and surface charge densities could be determined. It was found [53] that: 1) Freudlich isotherms were best suited for large pore sizes at high electrolyte concentrations. 2) Langmuir isotherms were best suited for small pore sizes at low electrolyte concentrations. 3) For some membranes both isotherms were acceptable. 4) The resulting surface charge density dependence on electrolyte concentration was found to be irregular. 5) The dimensionless apparent ζ_a-potential ($\zeta_a = z_+ F\zeta/RT$) increased rapidly at low NaCl concentrations and after a maximum began to degrease gradually. The behavior of surface charge densities and ζ_a-potentials suggests contributions from strong immobilization of solvent near pore surfaces and specific ion effects [54].

8.3. Summary

Although classical thermodynamics does not apply to non-equilibrium processes some classic phenomenological linear laws have been established. Rate of extensive state variables (X) change per entrance window area to reference volumes equals generalized fluxes.

Table 19
Collected rate constants (κ/s^{-1}) and distance between sites (λ/nm) for liquids on solids using molecular kinetic (*MK*) and molecular hydrodynamic (*MH*) models. Site distances (λ/nm) to be compared to molecular diameters (d_L/nm). Properties are listed both for the low ($Ca(v_L) < Ca(v_{ss})$) and high ($Ca(v_L) > Ca(v_{ss})$) wetting rate ranges, where $Ca(v_{ss})$ = slip-stick wetting range.

Table	Liquids	solids	κ (low Ca)	κ (high Ca)	λ (low Ca)	λ (high Ca)	d_L(low Ca)	d_L(high Ca)
Ref. 12	W	SiO_2	$2.4{\cdot}10^{9}$	$4.4{\cdot}10^{9}$	0.30		0.385	
T.3	EG	OS1-OS4	$4.7{\cdot}10^{6}$	$1.6{\cdot}10^{8}$	0.6	1.7	0.56	
T.3	EG	IJ5-IJ8	$2.9{\cdot}10^{2}$	$2.0{\cdot}10^{4}$	1.6	3.5	0.56	
T.4	W	OS1-OS4	$1.5{\cdot}10^{7}$	$2.1{\cdot}10^{8}$	1.0	1.8	0.385	
T.4	W	IJ4-IJ8	$2.3{\cdot}10^{1}$	$2.5{\cdot}10^{6}$	0.4	4.6	0.385	
T.13	C_1OH-C_8OH	h-phob glass	$9.9{\cdot}10^{1}$	$1.9{\cdot}10^{3}$	4.2	5.9	0.50	0.79
B-ext	C_1OH-C_8OH	h-phob glass	$1.6{\cdot}10^{4}$	$3.0{\cdot}10^{5}$	4.2	5.9	0.50	0.79
T.13	W,FoA,EG,G	h-phob glass	$2.0{\cdot}10^{3}$	$5.5{\cdot}10^{4}$	0.9	1.5	0.385	0.61
T.16	C_1OH-C_8OH	h-phob glass	$1.7{\cdot}10^{-1}$	$6.1{\cdot}10^{2}$	5.4	6.4	0.50	0.79
B-ext	C_1OH-C_8OH	h-phob glass	$5.0{\cdot}10^{2}$	$3.5{\cdot}10^{4}$	5.4	6.4	0.50	0.79
T.16	W,FoA,EG,G	h-phob glass	$2.2{\cdot}10^{3}$	$5.6{\cdot}10^{4}$	0.8	1.4	0.385	0.61
Ref. 18	W	PET	$2.0{\cdot}10^{5}$	$1.3{\cdot}10^{6}$	0.99	1.00	0.385	

Gradients of intensive state functions (*Y*) represent conjugate forces.

Phenomenological laws have been formulated based on these premises to account for familiar physical properties. They do as such not represent proper irreversible thermodynamics.

Fluxes depend on experimentally measurable multiple conjugate forces. They provide an opportunity to identify flux and force conditions to observe particular interlinked effects.

Ostwald's phenomenological constants relate these forces to the overall fluxes.

Enforced wetting is a transport process relating to irreversible thermodynamics. Therefore, phenomenological relationships may be used to design future enforced coupled force wetting experiments to produce more realistic molecular and hydrodynamic wetting models.

9. Conclusions

Molecular kinetic (*MK*) models were designed to relate time dependent contact angles to wetting rates. As shown in Table 19, poor agreement was found as compared to molecular relaxation and to surface diffusion rates. Surface site distances are mostly an order of magnitude too large. Most reasonable results were obtained when the unstable (chaotic) slip-stick wetting was excluded from molecular kinetic (*MK*) and molecular hydrodynamic (*MH*) models.

Reference values

- Molecular relaxation [22], $\kappa = 10^{6}\ s^{-1}$
- Viscous dissipation [41], $\kappa = 10^{11}\ s^{-1}$
- Water diffusion [12], $\nu_{transl} = 1.7{\cdot}10^{10}\ s^{-1}$
- Microwave relaxation [10,24], $\nu_{mw} < 3.0{\cdot}10^{11}\ s^{-1}$
- Water diel. Relaxation [10,23,24], $\nu_{diel} = 3.02{\cdot}10^{13}\ s^{-1}$
- C_1-C_{15} diel. Relaxation [10,23,24], $\nu_{IR} = 8.5{\cdot}10^{13}\ s^{-1}$
- C_1-C_{15} diel. Relaxation [10,23,24], $2.94{\cdot}10^{13}\ s^{-1} < \nu_{UV} < 2.03{\cdot}10^{15}\ s^{-1}$

Hydrodynamic (*HD*) models for thin film spreading relates cube of time dependent contact angles with fractal type logarithm of characteristic macroscopic and nanoscopic (molecular) length rates. However, the extracted nanoscopic (wedge) lengths remained unphysical.

The observed drawbacks seem to depend on: 1) Although even nanometric surface structure heterogeneities may influence wetting, no corrections for surface roughness were made before model fits. 2) The well-known contact angle–surface structure relationships identifying different; full (imbition), partial (Wenzel), partial rejection and full rejection (Lotus) wetting mechanisms were ignored. 3) No detailed physicochemical properties (van der Waals, Lewis, Brϕnsted) of probe liquids and model solids were recognized when model fits were evaluated. 4) The aim to enforce experimentally observed unstable (chaotic) slip-stick wetting into steady-state *MK*, *HD* and molecular hydrodynamic (*MH*) models seems unjustified. The poor success is evident from obtained results. 5) The *MK*, *HD* and *MH* models have been developed in isolation, without correlation to corresponding key properties of (diffusion, line tension, thin film spreading) processes. As a result, some modifications have no physicochemical foundation.

Enforced wetting is a transport process relating to irreversible thermodynamics. Several classical phenomenological relationships have been established. They may be used to design future enforced coupled force wetting experiments to produce more realistic molecular and hydrodynamic wetting models.

Declaration of Competing Interest

There are no conflicts of interest with coauthors (I am the sole contributor) or financial counterparts.

Acknowledgements

Academy of Finland financial support to Center of Excellence for Functional Materials (FunMat) at Åbo Akademi University is acknowledged.

References

[1] Rosenholm JB. In: Tadros ThF, editor. Colloid stability. The role of surface forces. Part II. Weinheim, Germany: Wiley-VCH; 2007. p. 1–83.
[2] Rosenholm JB. Adv Colloid Interface Sci 2016;234:89.
[3] Rosenholm JB. Adv Colloid Interface Sci 2017;247:264.
[4] Lyklema J. Fundamentals of interface and colloid science. In: Fundamentals. vol. 1. London, UK: Academic Press; 1991.
[5] Rosenholm JB. Adv Colloid Interface Sci 2021;294:102433.
[6] Van Oss CJ, Chadhury MJ, Good RJ. Adv Colloid Interface Sci 1987;28:35.
[7] Van Oss CJ, Chadhury MJ, Good RJ. Chem Rev 1988;88:927.
[8] Granqvist B, Järn M, Rosenholm JB. Colloids Surfaces A 2007;296:248.
[9] Lyklema J. Fundamentals of interface and colloid science. In: Solid-liquid interfaces. vol.2. London, UK: Academic Press; 1995.
[10] Rosenholm JB. Adv Colloid Interface Sci 2018;253:66.
[11] Rosenholm JB. Adv Colloid Interface Sci 2015;220:8.
[12] Clark JW, Hall PG, Pidduck AJ, Wright CJ. JCS Faraday I 1985;81:2067.
[13] De Gennes P-G, Brochard-Wyart F, Quére D. Capillarity and wetting phenomena. Drops, bubbles, pearls, waves. Berlin, Germany: Springer; 2002.
[14] Blake TD, Haynes JM. J Colloid Interface Sci 1969;30:421.
[15] Glasstone S, Laidler KJ, Eyring HJ. The theory of rate processes. New York, USA: McGraw-Hill; 1941.
[16] Blake TD. In: Berg JG, editor. Wettability. New York, USA: Marcel-Dekker; 1993 [p.251 and p.311].
[17] Tåg C-M, Järn M, Rosenholm JB. J Adhesion Sci Technology 2010;24:539.
[18] Hayes RA, Ralston J. J Colloid Interface Sci 1993;159:429.
[19] Järn M, Tåg C-M, Järnström J, Rosenholm JB. J Adhesion Sci Technology 2010;24:567.
[20] Järnström J, Järn M, Tåg C-M, Rosenholm JB Peltonen J. J Adhesion Sci Technology 2011;25:761.
[21] Schneemilch M, Hayes RA, Petrov JG, Ralston J. Langmuir 1998;14:7074.
[22] Ranabothu SR, Karnezis C, Dai LL. J Colloid Interface Sci 2005;288:213.
[23] Israelachvili J. Intermolecular & surface forces. London, UK: Academic Press; 1992.
[24] Hunter RJ. Foundations of colloid science. 2nd ed. Oxford, UK: Oxford Univ. Press; 2001.

[25] Rosenholm JB. Adv Colloid Interface Sci 2020;276:102047.
[26] Lyklema J. Fundamentals of interface and colloid science. In: Liquid-fluid Interfaces. vol.3. London, UK: Academic Press; 2000.
[27] Starov VM. In: Tadros ThF, editor. Colloid stability. The role of surface forces. Part II. Weinheim: Germany. Wiley-VCH; 2007. p. 85–108.
[28] Pompe T, Fery A, Herminghaus S. In: Mittal KL, editor. Contact angle, wettability, and adhesion. vol. 2. The Netherlands. VSB BV: Zeist; 2002. p. 377–86.
[29] Hoffman RL. J Colloid Interface Sci 1875;50:228.
[30] Tanner LH. J Phys D 1979;12:1473.
[31] Voinov OV. Fluid Dyn 1976;11:714.
[32] Cox RG. J Fluid Mech 1986;168:169.
[33] De Ruijter MJ, De Coninck J, Blake TD, Clark A, Rankin A. Langmuir 1997;13:7293.
[34] De Ruijter MJ, De Coninck J, Oshanin G. Langmuir 1999;15:2209.
[35] Von Bahr M, Tiberg F, Yaminsky V. Colloids Surfaces A 2001;193:85.
[36] Peltonen J, Järn M, Areva S, Lindén M, Rosenholm JB. Langmuir 2004;20:9428.
[37] Apel-Paz M, Marmur A. Colloids Surfaces A 1999;146:273.
[38] Garnier G, Bertin M, Smrchova M. Langmuir 1999;15:7863.
[39] Modaressi H, Garnier G. Langmuir 2002;18:642.
[40] Määttänen A, Ihalainen P, Bollström R, Toivakka M, Peltonen J. Colloids Surfaces A 2010;367:76.
[41] Petrov JG, Ralston J, Schneemilch M, Hayes RA. J Phys Chem B 2003;107:1634.
[42] Petrov JG, Ralston J, Hayes R. Langmuir 1999;15:3365.
[43] Extrand CW. Langmuir 2003;19:646.
[44] Voinov OV. Sov Phys Dokl (Engltransl) 1978;23:891.
[45] Zhou MY, Sheng P. Phys Rev Lett 1990;64:882.
[46] Sheng P, Zhou MY. Phys Rev A 1992;45:5694.
[47] Dussan VEB, Rame E, Garoff S. J Fluid Mech 1991;230:97.
[48] Stokes JP, Higgins MJ, Kushnick AP, Bhattacharya S, Robbins MO. Phys Rev Lett 1990;65:1885.
[49] Petrov PG, Petrov JG. Langmuir 1992;8:1762.
[50] Plawsky J. Transport phenomena fundamentals. 2nd ed. Boca Raton, Florida, USA: CRC Press; 2010.
[51] Diez LM, Villa FM, Gimenez AH, Garcia FT. J Colloid Interface Sci 1989;132:27.
[52] Hernandez A, Martinez F, Martin A, Pradanoz P. J Colloid Interface Sci 1995;173:284.
[53] Molina C, Victoria L, Arenas A, Ibanez J. J Membr Sci 1999;163:239.
[54] Chen L, Bonaccurso E. Adv Colloid Interface Sci 2014;210:2.